The properties of a spectroscopically selected sample of cataclysmic variables

by

Amornrat Aungwerojwit

Thesis

Submitted to the University of Warwick

for the degree of

Doctor of Philosophy

Department of Physics

July 2007

THE UNIVERSITY OF
WARWICK

“Better a single day of life, seeing the reality of arising and passing away than a hundred years of existence, remaining blind to it.”

The Buddha

Contents

List of Tables

List of Figures

Acknowledgments

I would like to thank Dr. Boris Gänsicke for being a superb supervisor in guiding me during my PhD. Without his useful suggestions, constructive comments, kindness, and patience, the work presented in this thesis could not have been satisfactory. I am grateful for his enthusiasm, which has inspired me and has picked me up out of the depths of despair numerous times. I am greatly indebted for his introducing me to the world of research and helping me to be involved in several projects other than my thesis work. I am deeply thankful for his trust in allowing me, a novice, to "play" with various ground-based telescopes for nearly 200 observing nights, which indeed recharged my "battery" from time to time during the four-year period of studying.

I would like to thank all observers listed in Table 2.1 who contributed their big efforts in obtaining the data during the past few years and I do apologise in advance to those that I do not mention here. I thank Dr. Pablo Rodríguez-Gil, Dr. Sofía Araujo-Betancor, and Dr. John Southworth for their work on all spectroscopic data reduction presented in this thesis. Deep thanks goes to Dr. Pablo Rodríguez-Gil who guided me on how to observe with the IAC80 and the OGS telescopes. I thank Ana Guijarro and all supporter astronomers at Calar Alto observatory, the Observatorio del Teide, the Observatorio del Roque de los Muchachos, and Kryoneri observatory, who helped the first night of each observing run pass smoothly. Prof. Tom Marsh is acknowledged for his developing and sharing in reduction and analysis packages.

I am grateful to the Royal Thai Government for a studentship.

I thank Dr. Kannika Tampanishvong who has been my trustworthy friend, sharing my blues and beautiful days. I appreciate her help in scanning any inconsistency in Chapter 1 and Chapter 2. Special thanks go to Dr. John Southworth for his generosity and speedy proof-reading of the entire thesis. I also thank the following friends for their support and making these four years lively: Ratchada Pattaranit, Issavara Sirirungruang, Pattarawit Polpinit, Paradee Tungtang, Wila-sini Wongkaew, Jittiwut Suwatthikul, Kamolchanok Chongsathien, Susana Barros, and Monihar Dillon.

Finally, my deepest gratitude goes to my parents and my sisters for their unconditional love, no matter what I am and what I have chosen in my life.

Declarations

I hereby declare that this thesis has not been submitted in any previous application for a higher degree. This thesis represents my own work except where references to other works are given. In particular, details on observations and data reduction carried out by my collaborators are given in Chapter 2.

The following chapters are based on refereed publications that I submitted during my period of study:

Chapter 4 is based on: A. Aungwerojwit, B. T. Gänsicke, P. Rodríguez-Gil, H.-J. Hagen, E. T. Harlaftis, C. Papadimitriou, H. Lehto, S. Araujo-Betancor, U. Heber, R. E. Fried, D. Engels, and S. Katajainen, "HS 0139+0559, HS 0229+8016, HS 0506+7725, and HS 0642+5049: Four new long-period cataclysmic variables" Astronomy & Astrophysics, 443, 995 (2005).

Chapter 5 is based on: A. Aungwerojwit, B. T. Gänsicke, P. Rodríguez-Gil, H.-J Hagen, S. Araujo-Betancor, O. Baernbantner, D. Engels, R. E. Fried, E. T. Harlaftis, M. Mislis, D. Nogami, P. Schmeer, R. Schwarz, A. Staude, and M.A.P. Torres, "Dwarf novae in the Hamburg Quasar Survey: Rarer than expected" Astronomy & Astrophysics, 455, 659 (2006).

Chapter 6 is based on: A. Aungwerojwit, B. T. Gänsicke, P. Rodríguez-Gil, H.-J. Hagen, O. Giannakis, C. Papadimitriou, C. Allende Prieto, and D. Engels, "HS1857+5144: A hot and young pre-cataclysmic variable", Astronomy & Astrophysics, 469, 297 (2007).

Abstract

Over the past two decades, disrupted magnetic braking has been the standard paradigm of cataclysmic variable (CV) evolution with relatively few modifications. The predictions made by this theory, however, are in strong disagreement with the observations. These discrepancies may, at least in part, be related to observational selection effects. In order to circumvent observational biases, a search for CVs was carried, selecting candidates in a homogenous way using their spectroscopic appearance in the Hamburg Quasar Survey (HQS), resulting in the discovery of 50 new CVs and 3 new cataclysmic progenitors (pre-CVs).

In this thesis, I present follow-up time-resolved spectroscopic and photometric observations of nine new CVs and one new pre-CV from the HQS. Their orbital periods were determined from radial velocity and photometric variability studies. Specifically, four relatively bright CVs, HS 0139+0559, HS 0229+8016, HS 0506+7725, and HS 0642+5049 are found in the narrow 3–4 h orbital period range, i.e. $P_{\rm orb} = 243.69 \pm 0.49$ min, 232.550 ± 0.049 min, 212.7 ± 0.2 min, and 225.90 ± 0.23 min, respectively. Although they have very similar orbital periods, they greatly differ in their observed properties. HS 0506+7725 is classified as a VY Scl star. The other three systems are identified either as UX UMa-type novalike variables or as Z Cam-type dwarf novae.

The orbital periods of five new dwarf novae HS 0417+7445, HS 1016+3412, HS 1340+1524, HS 1857+7127, and HS 2214+2845 cover the range $\sim 1.5 - 5$ h, i.e. $P_{\rm orb} \simeq 105.1$ min or $\simeq 109.9$ min, 114.3 ± 2.7 min, 92.66 ± 0.17 min, 272.317 ± 0.001 min, and 258.02 ± 0.56 min, respectively. These five dwarf novae display a variety of observed properties: HS 0417+7445 is a SU UMa-type dwarf nova, and HS 1016+3412 and HS 1340+1524 have rare outbursts, but their subtype is yet undetermined. The eclipsing HS 1857+7127 may be a Z Cam-type dwarf nova and HS 2214+2845 is a U Gem-type dwarf nova.

Finally, the orbital period of one of the youngest pre-CVs, HS 1857+5144, was determined to be $P_{\rm orb} = 383.5203 \pm 0.0001$ min. The light curves of HS 1857+5144 display large amplitudes of brightness variation resulting from a reflection effect on the heated inner hemisphere of the companion star, suggesting a very high temperature of the white dwarf.

To date, the orbital periods of 44 new HQS CVs/pre-CVs have been measured. It is clear that our survey did not identify the large number of short-period CVs predicted by the population models. The ratio of short-period ($\lesssim 3$ h) to long-period (> 3 h) systems of the new HQS sample is only half that of the previously known CVs. In contrast, the HQS CV survey has been very prolific in identifying bright long-period CVs, with a distinct preference for the 3–4 h period range. Surprisingly, the HQS sample provides a large number of SW Sex stars, which represent 25% of all new CVs above the period gap, and nearly half in the 3–4 h period range.

Chapter 1

Introduction

1.1 Scientific background

1.1.1 Motivation

The majority of stars in the sky are born in binaries, and a substantial fraction of them will interact at some point in their lives (Iben 1991). The interactions between the two stars and mass exchange between them have a significant impact on their evolution. The different combinations of the two stellar components in such binaries result in the most exotic objects in the Galaxy e.g. galactic black-hole candidates, low-mass X-ray binaries, millisecond pulsars, cataclysmic variables (CVs), and double degenerate systems. Among them, CVs are most easily accessible to observations as they are numerous, fairly bright ($12 \lesssim V \lesssim 20$), relatively nearby (a few hundred parsecs away), contain well-understood stellar components, and have short orbital periods in the range from about one hour to a day. Due to their interacting nature, CVs provide excellent cosmic laboratories to study exotic phenomena over all wavelengths, from radio waves to X-rays. This includes the limited knowledge on accretion discs, which are a common phenomenon occurring throughout the Universe, from the formation of solar systems like ours to fuelling the nuclei of active galaxies. In addition, CVs offer the possibility to examine plasma physics in very strong magnetic fields of $\sim 10-200\,\mathrm{MG}$, which cannot be created in any terrestrial laboratory.

From a cosmological point of view, CVs are of extraordinary interest as they are closely related to Type Ia supernovae (SN Ia), which are thought to be the violent explosions of accreting white dwarfs driven over the Chandrasekhar mass limit. Given that the ground-shaking discovery of "dark energy" is based on the interpretation of SN Ia as standard candles, it is of utmost importance that all effort is made to arrive at a complete understanding of SN Ia progenitors.

Despite its enormous importance, our understanding of CV evolution is still rather fragmentary. Although over the past two decades a host of theoretical models have been put forward to explain the evolution of CVs, none of them can successfully match the observed properties of CVs in their entirety. It is likely that part of this discrepancy is caused by observational selection effects, resulting in incomplete and skewed CV samples, which do not reflect the properties of the true galactic CV population. To progress on the observational side, it is therefore clear that a large and unbiased sample of CVs, as well as of their progenitors, or pre-CVs, is necessary to be established.

1.1.2 Thesis objectives

The work in this thesis focuses on spectroscopic and photometric observations to characterise new CVs/pre-CVs that were identified in the Hamburg Quasar Survey (HQS) using the spectroscopic hallmark of CVs: the presence of hydrogen Balmer emission lines in their optical spectra. This selection is thought to provide a large and homogeneous sample of CVs that will serve as an important tool to improve our understanding of the evolution of CVs. Based on the follow-up data analysed here, the orbital periods of these new CVs, the most easily measured parameter that is relevant to the evolution of CVs, will be determined. The characteristics of the

HQS CVs will then be compared to those of CV samples originating from other surveys, as well as to the predictions of the CV evolution theory.

Throughout the rest of this Chapter, I describe the structure and the properties of CVs as well as the current standard scenario of their evolution (Sections 1.2–1.6). In Section 1.7, I spell out the inconsistencies between predictions made by the theory and observational facts, which are the main motivation of this thesis. Finally, I discuss the different methods of finding CVs and why the known CV population is likely to be strongly biased and incomplete. I then specifically describe the search for new CVs/pre-CVs in the HQS (Section 1.8), and show that a spectroscopic selection of CVs should, in principle, provide a homogenous sample of CVs.

1.2 Cataclysmic variables

CVs are semi-detached close binary systems comprising an accreting white dwarf, and a late-type main-sequence donor (see Patterson 1984; Smith & Dhillon 1998). The orbital periods of CVs typically range between ~ 80 min and ~ 10 h, with only a few systems having shorter or longer periods. An entire CV could easily fit inside a star as large as our Sun. The accretion rates encountered in CVs are typically in the range $10^{-11} - 10^{-8}\, M_{\odot}\,\mathrm{yr}^{-1}$ (e.g. Howell et al. 2001). The strength of the magnetic field of the white dwarf plays an important role in governing the accreting matter. If the magnetic field is weak, then mass transfer takes place via an accretion disc, with a luminosity enhancement at the outer edge of the disc, or a "bright spot", where the stream leaving the donor star impacts the disc (Figure 1.2a). In contrast to this, if the magnetic field is strong enough to suppress the formation of the disc, the accretion stream flows along the magnetic field lines from the secondary star to the poles of the white dwarf (Figure 1.2b). For moderate magnetic field strengths, the transferred material may form a partial disc whose inner part is disrupted into accretion columns.

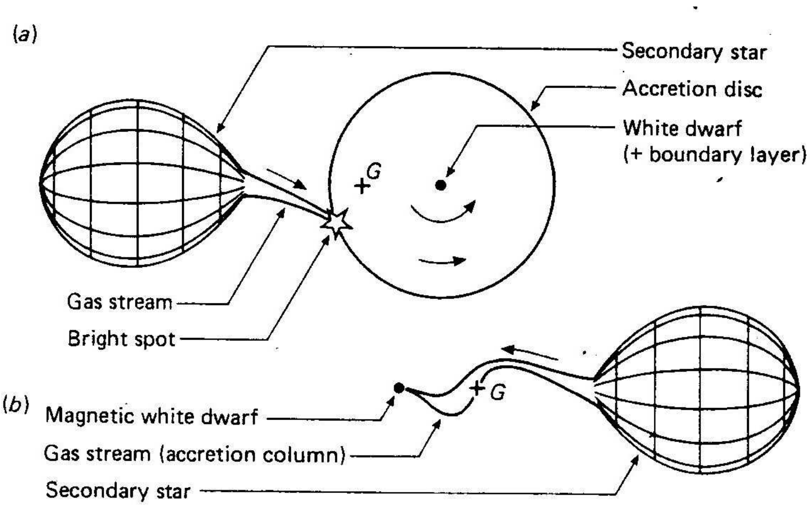

Figure 1.1: Schematic views of the components in (a) a weak or non-magnetic CV and (b) a strong magnetic CV. The stars rotate around the centre of mass of the system (G). In the weak/non-magnetic system, a disc forms around the white dwarf, and the stream of material impacts at the outer edge of the disc, resulting in a "bright spot". In the strong magnetic system, the magnetic field of the white dwarf prevents the formation of a disc and the stream is channelled along the magnetic field lines to the magnetic pole(s) of the the white dwarf. Taken from Pringle & Wade (1985).

As suggested by their name, a wide range of variability may be observed in CVs, ranging from flickering with time scales of minutes to dramatic brightenings such as dwarf nova outbursts or classical nova eruptions (see Section 1.3 for classification scheme). Historically, the morphology of their long-term optical light curves has been the primary information on which CV classification was based. However, from a more modern perspective, this classification scheme should be taken with a grain of salt, and we should start to think of CVs as being divided into different groups because of their physical differences. The three main physical parameters that determine the appearance of a CV are the orbital period (which is a proxy for the geometric extension of the system), the accretion rate, and the magnetic field strength of the white dwarf. Below, I describe the different types of CVs grouped together as a function of their differing physical parameters.

1.3 CV classification

Dividing CVs into different types according to their physical properties such as their orbital periods, mass-transfer rates, and magnetic field strengths of the accreting white dwarfs is likely to create subsamples with different observable properties, such as e.g. different orbital period distributions. Because the orbital period distribution of the observed CVs is a major tool to test the evolution of CVs, observers ultimately need to quantify the different selection effects applying to the different CV subsamples, and a successful binary evolution theory must be able to explain the features found in the observed period distributions of the different subclasses, after correcting for the selection effects.

Figure 1.2 presents the orbital period distribution of different classes of 572 known CVs from Ritter & Kolb (2003, Edition 7.5 of July 2005). The period distribution of the entire set of systems shows three striking features: a dearth of systems in 2–3 h period range (the so-called *period gap*), a sharp cut-off at ~ 80 min, and the decreasing number of systems at long periods. These features will be discussed in more details in Section 1.7. The distributions of the individual subclasses are markedly different, which at the moment is due to a mixture of observational selection effects and the underlying physical properties of the different CV types. The major classes of CVs are outlined below.

1. **Classical novae**

   These are the brightest manifestations of mass transfer onto the white dwarfs in CVs. During classical nova explosions, the brightnesses of the systems increase by 6–19 magnitudes, lasting from weeks to years. These powerful outbursts are caused by a thermonuclear runaway of hydrogen-rich material accumulated on the surface of the white dwarf accreting at a rate lower than $10^{-9}\,M_{\odot}\,\mathrm{yr}^{-1}$ (Cassisi et al. 1998). The accreted layer grows until it gets sufficiently hot and dense to ignite hydrogen burning, which turns into an

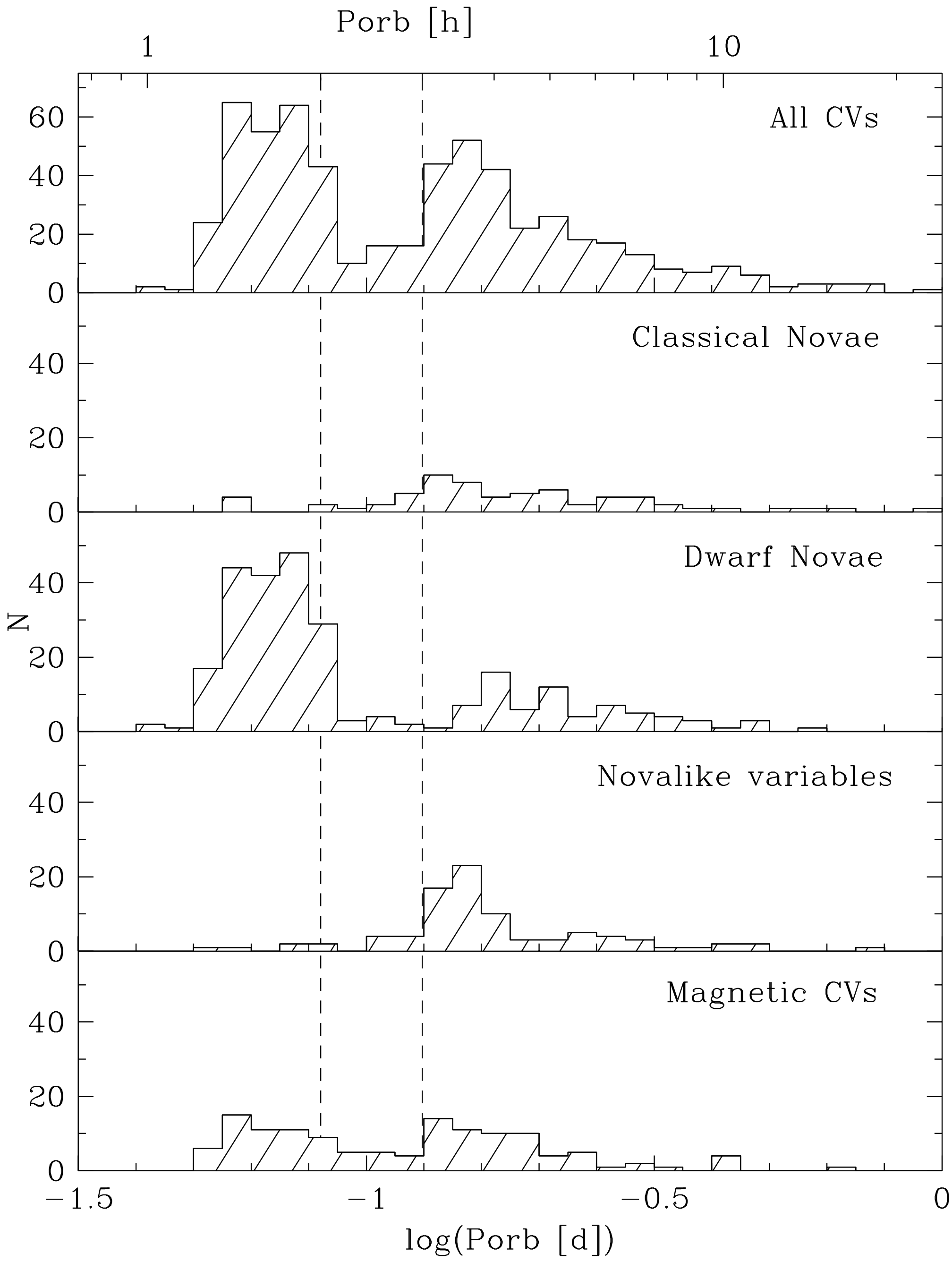

Figure 1.2: *Top panel:* orbital period distribution of 572 known CVs from Ritter & Kolb (2003, Edition 7.5 of July 2005) within the orbital period range ~ 1 h to ~ 1 d, and after removing AM CVn systems, the ultracompact binaries with a helium secondary. The remarkable features in this period distribution are the 2–3 h conventional "period gap" (dashed lines), a sharp cut-off at ~ 80 min, and a dwindling number of the systems at long orbital period. *Bottom four panels:* those are illustrated again according to their classes.

explosive reaction that blows off the layer. An estimate of the recurrence time of a classical novae is in the order of $\sim 10^3 - 10^4$ yr (Patterson 1984; Downes 1986). $\sim 12\%$ of the systems in Ritter & Kolb (2003) are listed as classical novae; their orbital periods span the range 1.4 h to more than 16 h, with most of them found between 3 h and 5 h (e.g. Diaz & Bruch 1997; Warner 2002).

2. **Dwarf novae**

   Dwarf novae represent the largest CV subclass ($\sim 46\%$ of all known CVs). They are the dominant type of systems among CVs with non- (or weak) magnetic white dwarfs. Dwarf novae are observed undergoing regular outbursts, during which they brighten by 2–5 magnitudes, lasting from days to weeks. The recurrence times of the outbursts range from weeks to years. The cause of the outbursts is a thermal instability in the accretion disc, which occurs around the ionisation temperature of hydrogen and implies that there exists a mass-transfer rate above which accretion discs will be stable and show no outbursts. Dwarf novae are subdivided into three distinct subclasses based on their observed outburst properties: U Gem, Z Cam, and SU UMa types.

   - The U Gem-type dwarf novae show regular outbursts which do not have characteristics of Z Cam and SU UMa stars. They are found above the period gap.
   - The Z Cam-type dwarf novae are characterised by rapid outbursts interspersed with more or less constant brightness at an intermediate level between outburst maxima and minima, the so-called standstills. The standstills are ~ 0.7 mag fainter than the maximum brightness, and they last from ten days to years. It has been suggested that Z Cam stars are on the borderline between novalike variables and dwarf novae (Smak 1983) with a mass-transfer rate fluctuating about the critical value that switches them from one behaviour to the other (e.g. Schreiber et al.

2002). All Z Cam stars lie above the period gap.

- The SU UMa-type dwarf novae undergo occasional superoutbursts in addition to normal outbursts. Superoutbursts occur less frequently than normal outbursts, but they are brighter (~ 0.7 mag) and last longer (~ 5 times). During a superoutburst, a modulation of the light curve appears near superoutburst maximum, called a superhump, which is caused by the deformation of the disc by tides from the donor star (Whitehurst 1988; Hirose & Osaki 1990; Lubow 1991). In general, the superhump period is a few percent longer than the orbital period. Most of the recurrence times of superoutbursts are around a few hundred days. Some systems such as ER UMa and WZ Sge stars, however, have extremely short or long recurrence times. ER UMa stars undergo superoutbursts every 20–50 days, interleaved by a rapid succession of normal outbursts occuring every few days. WZ Sge stars are characterised by infrequent superoutbursts of every few years to decades, and usually do not undergo normal outbursts. Practically, all SU UMa stars have orbital periods below 2 h.

The orbital period distribution of all known dwarf novae is discussed in more details in Section 5.8.1.

3. **Novalike variables**

This group belongs to the non-eruptive CVs and it contains $\sim 15\%$ of the objects listed by Ritter & Kolb (2003)[1]. They are characterised by a roughly steady brightness due to a high rate of mass transfer which exceeds the critical rate for disc instabilities, resulting in the systems being stuck in a "permanent outburst", called a high state. Novalike variables are subdivided into the fol-

[1]Note that, Ritter & Kolb (2003) classify magnetic CVs as novalike variables as well, which follows the historic definition based on their light curve. Here, I treat magnetic CVs as a separated class.

lowing distinct subclasses according to their spectroscopic and photometric properties.

- UX UMa stars have persistent broad Balmer absorption line spectra, typical of optically thick discs seen at relatively low inclination.
- RW Tri stars display pure emission line spectra (albeit occasionally with sharp absorption cores) and they are thought to have higher inclinations than UX UMa-type systems.
- VY Scl stars spend most of their time in a bright state and abruptly drop by more than one magnitude into faint states, which last from weeks to years. During the low states, they may spectroscopically appear like quiescent dwarf novae but do not show dwarf nova outbursts (see Warner 1995, and references therein). The cause of the faint state is thought to be due to the temporary cessation of mass transfer from the secondary star. Interestingly, VY Scl stars appear almost entirely just above the period gap in the range 3–4 h (see discussion in Section 4.6).
- SW Sex stars were proposed by Thorstensen et al. (1991a) to be a distinct subclass of novalike variables . The SW Sex stars are preferentially found at $3\,\mathrm{h} \lesssim P_{\mathrm{orb}} \lesssim 4\,\mathrm{h}$ and are often, but not always, eclipsing systems (for non-eclipsing systems see e.g. Casares et al. 1996; Dickinson et al. 1997; Martínez-Pais et al. 1999; Taylor et al. 1999; Hoard et al. 2000; Rodríguez-Gil et al. 2007b). These systems share a number of peculiar characteristics which cannot easily be explained by the steady-state optically thick accretion disc model: (a) they have unusual V-shaped eclipse profiles (in case of high inclination systems); (b) their optical spectra are characterised by single-peaked emission lines that display central absorption dips at particular phases; (c) their spectra contain strong He II λ4686 emission lines; (d) their radial velocity curves derived from

their emission lines reveal substantial phase lags relative to their photometric ephemerides. SW Sex stars represent nearly 40% of the total novalike/classical nova population (Rodríguez-Gil et al. 2007b). Specifically, they represent half of the total population of novalike variables in the 3–4 h orbital period range (Rodríguez-Gil et al. 2005a, 2007b; and see also a discussion in Section 4.6).

Unlike dwarf novae which are found mostly below the period gap where low mass-transfer rate are thought to be driven by gravitational radiation, almost all novalike variables are found above the period gap, where magnetic braking can drive much higher mass-transfer rates (see Section 1.6). However, a number of dwarf novae and novalike variables are found in overlapping period ranges, implying that mass-transfer rates can vary significantly between different systems for the same orbital period.

4. **Magnetic CVs**

   The CVs in this class contain magnetic white dwarfs with intermediate to strong magnetic fields, $B \simeq 1 - 200\,\mathrm{MG}$, that affect or control the interaction between the white dwarf and the material accreted from the Roche-lobe-filling companion. They are further divided into two different subclasses according to the strength of the magnetic field of the white dwarf. Ritter & Kolb (2003) list $\sim 22\,\%$ of all known CVs as magnetic systems.

   - Polars, or AM Her stars contain white dwarfs with magnetic field strengths of $10\,\mathrm{MG} \lesssim B \lesssim 200\,\mathrm{MG}$. In these systems, the accreted material cannot form a disc around the white dwarf. Instead, the white dwarf takes control of the flow of gas, forcing it to follow the magnetic-field lines towards one or both poles of the (presumed) dipolar magnetic field. The accretion flow passes through a shock standing above the surface of the white dwarf, turning polars into intense X-ray sources. The strong magnetic fields of the white dwarfs in polars interact with the weaker fields of the secondary star, resulting in a synchronous rotation of the white dwarf spin and the orbital motion of the system, or $P_{\rm spin} = P_{\rm orb}$ (for comprehensive reviews see Cropper 1990; Warner 1995). The orbital periods of the known polars are found in the range between $\sim 80\,$min and a few hours with a preference for systems below the period gap.

- Intermediate polars (IPs), or DQ Her stars, have weaker magnetic fields, $1\,{\rm MG} \lesssim B \lesssim 10\,{\rm MG}$, that generally are not strong enough to entirely suppress the formation of a disc. In this case, a partial disc may form which is truncated in the middle by the magnetic field of the white dwarf. IPs typically have high mass-transfer rates, which produce harder X-ray spectra than generally observed in polars. Because of their weaker fields, the white dwarfs in IPs are not synchronised with the orbit of the system, and in many systems the white dwarf rotates with spin period $P_{\rm spin} \sim 0.1 P_{\rm orb}$ (see Patterson 1994). In practice, the IP nature of a system is confirmed by the detection of coherent variability on the spin period and/or the beat period between the spin and the orbital periods. There are ~ 30 confirmed IPs, and their orbital periods are concentrated above the period gap (Norton et al. 2004; Gänsicke et al. 2005a).

1.4 Roche geometry

In close binary systems, the shapes of stellar components are defined by equipotential surfaces, where the potential is given by the sum of the gravitational potentials of the two stars plus the rotational potential. The shapes of these equipotential surfaces depend only on the mass ratio, q, of the system, and their absolute dimensions depend on the orbital period (or the binary separation, a). Figure 1.3 illustrates the cross section of the equipotential surfaces in the orbital plane of a binary system for $q = M_2/M_1 = 0.2$ where M_1 is mass of the primary star and M_2 is mass of the secondary star. If the stars have relatively small radii, they will have approximately spherical shapes and be well-detached, as shown by the equipotential surfaces close to M_1 and M_2. Stars having larger radii will be more distorted from a spherical shape. The two surfaces touching at L_1, or the inner Lagrangian point, are called Roche lobes (bold contours). The Roche lobe defines the maximum volume of the star that its matter can occupy under its own gravity. If a star is filling its Roche lobe, it will transfer material to its companion through L_1. Systems in which one component fills its Roche lobe are called semi-detached binaries, e.g. CVs. Another Lagrangian point labelled as L_2, or outer Lagrangian point is the easiest gateway through which matter can escape from the gravitational field of the system. This point lies on the equipotential of a contact binary where the two stars fill their Roche lobes, and are surrounded by a common envelope. A higher potential than L_2 is found at L_3, on the opposite side of L_2. The highest potential is located at points L_4 and L_5. The Lagrangian points L_1 to L_5 represent points where all existing forces within the system cancel each other, and potentially matter can be stored.

In CVs, the low-mass secondary star fills its Roche lobe, resulting in mass overflowing into the Roche lobe of the white dwarf via L_1, which is the saddle point of the equipotential surface. One immediate consequence of the Roche-lobe filling is that the donor stars in CVs are tidally locked to the orbital period, i.e. $P_{\rm spin} = P_{\rm orb}$. The radius of the secondary star is defined by the volume radius of the Roche lobe, $R_{\rm L_2}$, according to Eggleton (1983)'s approximation,

$$\frac{R_{\rm L_2}}{a} = \frac{0.49q^{2/3}}{0.6q^{2/3} + \ln(1+q^{1/3})} \tag{1.1}$$

which is accurate to about $\pm 1\%$. The separation, a, between the centres of mass of the binary can be determined from Kepler's third law

$$P_{\rm orb}^2 = \frac{4\pi^2 a^3}{G(M_1+M_2)} \tag{1.2}$$

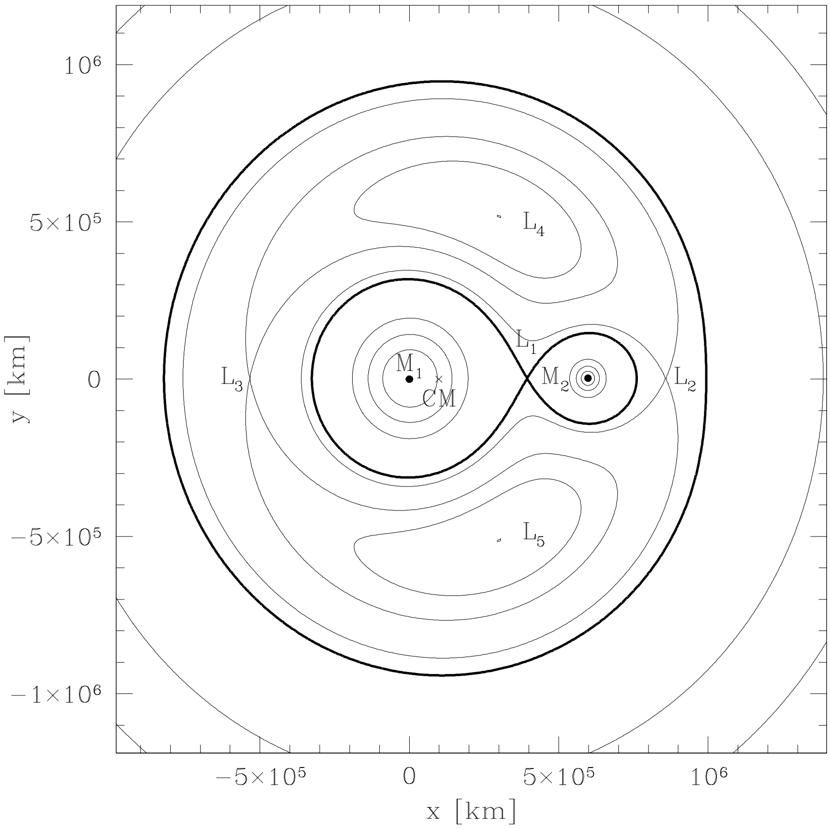

Figure 1.3: A cross section in the orbital plane of a schematic Roche geometry, showing the Lagrangian points L_1 to L_5 for a close binary system of $q = 0.2$. The Roche lobes of the two stars are drawn in bold and represent the equipotential surface which makes contact at the inner Lagrangian point, L_1 (see Section 1.4 for details). Provided by B. Gänsicke.

or

$$a = 3.35 \times 10^{10} \left(\frac{M_1}{M_\odot}\right)^{1/3} (1+q)^{1/3} P_{\rm orb}^{2/3}(\rm h) \qquad \rm cm. \tag{1.3}$$

The mean density of the Roche-lobe-filling secondary then becomes

$$\bar{\rho}_2 = 107 P_{\rm orb}^{-2}(\rm h) \qquad \rm g\,cm^{-3}, \tag{1.4}$$

which implies that CVs with $1\,\rm h \lesssim P_{\rm orb} \lesssim 10\,\rm h$ will contain low-mass main-sequence companions with $\rho \sim 1 - 100\,\rm g\,cm^{-3}$.

1.5 Mass transfer

Mass transfer between two components in close binaries changes the size of the Roche lobes and the orbital period of the system. The reaction of the binary to mass transfer depends on the mass ratio of the donor to the white dwarf. In the context of CVs, mass exchange/loss occurs within two different phases of the evolution, i.e. during the pre-CV phase and the CV phase (see Section 1.6 for their evolution tracks). During the pre-CV phase, the system contains two main-sequence stars. Once the more massive star evolves off the main sequence, it eventually fills its Roche lobe and transfers mass to the less massive component. Since the more massive Roche-lobe-filling star is nearer to the centre of mass of the system, its lost mass is then moved further away from the centre of mass, onto its companion, which results in an increased angular momentum of the transferred material. In order to conserve the angular momentum, the separation decreases, and consequently, the size of the Roche lobe decreases according to Equation 1.1. This configuration is, hence, unstable and results in a brief and violent phase of mass transfer and the creation of a common envelope.

For CVs, mass is transferred from the low-mass main-sequence star to the more massive accretor, or the white dwarf. In this case, the low-mass star is further away from the centre of mass. Transferred material, then, ends up closer to the centre of mass. This causes the transferred material to lose angular momentum, and as a result, the separation increases to conserve the overall angular momentum; the size of the Roche lobe then increases, leading the secondary star to detach from its Roche Lobe, and consequently mass transfer ceases. Mass transfer in CVs can only be sustained either by an expansion of the secondary star due to nuclear evolution, or by shrinking of the Roche lobe as a result of orbital angular momentum loss by means of magnetic braking or gravitational radiation. Nuclear evolution, however, cannot explain most CVs, since they contain secondary stars of less than a solar mass which cannot evolve significantly during the age of the Universe.

1.6 The evolution of CVs

1.6.1 Pre-Cataclysmic variable evolution

CVs are thought to be descended from post common envelope binaries (PCEBs). These systems have originated from wide binaries that lost substantial angular momentum through a common envelope phase (Paczynski 1976; Iben & Livio 1993; Iben & Tutukov 1993). The initial stellar components of these PCEBs consist of an intermediate-mass main-sequence star ($\sim 1-10\,M_{\odot}$), the primary star, and a low-mass companion ($\lesssim 1\,M_{\odot}$), the secondary star, with an orbital period of the order of years. The primary star evolves faster, becoming a giant which expands and fills its Roche lobe. The mass transfer from the more massive star to the lower mass companion is dynamically unstable. As a result of the high mass-transfer rate, which may reach 0.1 $M_{\odot}\,\mathrm{yr}^{-1}$ (Webbink 1979), the secondary star is driven out of its thermal equilibrium and then also fills its Roche lobe. An envelope of gas forms around the two stars, leading the system into the common envelope phase. Friction between the common envelope and the stellar components causes the two components transferring angular momentum to the envelope while they spiral inwards. As a result, the binary separation decreases from $\sim 100\,R_{\odot}$ to $\sim 1\,R_{\odot}$ within 10^{3} yr. If the energy deposited in the envelope exceeds its binding energy, the common envelope will be ejected. The system may appear as a binary central star of a planetary nebula comprising a hot subdwarf/white dwarf and a low-mass main-sequence companion, e.g. MT Ser (Grauer & Bond 1983; Green et al. 1984), UU Sge (Miller et al. 1976; Pollacco & Bell 1993, 1994), Abell 65 (Hilditch et al. 1996), and KV Vel (Hilditch et al. 1996; Wood et al. 1995; Ferguson et al. 1999). When the planetary nebula has been dispersed, the hot primary will gradually cool down and evolve into a white dwarf, allowing the system to be observed as a short-period white dwarf/main-sequence detached binary with an orbital period of a few days. The system will evolve into a CV configuration when angular momentum loss takes place by means of magnetic braking and/or gravitational radiation, which decreases the binary separation enough to bring the secondary star into contact with its Roche lobe. The typical time to evolve into a CV configuration is ~ 2 Gyr (Schreiber & Gänsicke 2003).

1.6.2 Disrupted magnetic braking

Disrupted magnetic braking was proposed as a standard model of CV evolution with the primary aim to explain the lack of systems in the 2–3 h period range, the *period gap* in Figure 1.2 (e.g. Rappaport et al. 1983; Spruit & Ritter 1983; Paczyński & Sienkiewicz 1983; Patterson 1984, and see Howell et al. 2001 for a recent review). The essential idea is that CVs evolve towards shorter periods because of angular momentum loss by magnetic braking (e.g. Verbunt & Zwaan 1981) and gravitational radiation (Kraft et al. 1962) with the nature of the dominant agent depending on the orbital period of the system. Magnetic braking is governed by the stellar wind and the stellar magnetic field of the rapidly rotating secondary star (being tidally synchronised with the orbital motion). The extraction of angular momentum by gravitational radiation becomes significant for short-period systems, and magnetic braking dominates at longer orbital periods ($P_{\rm orb} \gtrsim 3$ h) where the Roche-lobe-filling stars still have a radiative core.

At $P_{\rm orb} \gtrsim 3$ h, the relatively high mass loss rate of $\sim 10^{-9} - 10^{-8}\,M_{\odot}\,{\rm yr}^{-1}$ drives the secondary star out of its thermal equilibrium, resulting in a slight expansion. At $P_{\rm orb} \simeq 3$ h, the secondary star becomes fully convective (at $\sim 0.2-0.3\,M_{\odot}$), causing magnetic braking either to cease totally or to dramatically decrease (Rappaport et al. 1983; Spruit & Ritter 1983; Taam & Spruit 1989). As a consequence, the angular momentum loss rate decreases, and therefore, the mass transfer rate decreases. The lower mass-transfer rate allows the secondary star to shrink towards its main-sequence radius and ultimately to lose contact with its Roche lobe. The mass transfer then completely stops, resulting in the onset of the period gap at $P_{\rm orb} \simeq 3\,$h; the CVs become detached systems that are too inconspicuous to be found. Gravitational radiation causes these systems to continue to evolve towards shorter periods. When the Roche lobe shrinks enough to make again contact with the secondary star at $P_{\rm orb} \simeq 2\,$h, the mass transfer resumes. The mass transfer at $P_{\rm orb} < 2\,$h is driven only by the less efficient mechanism of gravitational radiation, with low mass-transfer rates of $10^{-11} - 10^{-10}\,M_{\odot}\,{\rm yr}^{-1}$. Such low mass-transfer rates drive the evolution of the short period systems on much longer timescale than in the case of magnetic braking. The timescales for angular momentum loss due to magnetic braking, $\tau_{\rm MB}$, and gravitational radiation, $\tau_{\rm GR}$, are given by (Kolb & Stehle 1996)

$$\tau_{\rm MB} = -\left(\frac{J}{\dot{J}}\right)_{\rm MB} = 2.2\times10^{9}\frac{M_1}{(M_1+M_2)^{1/3}}R_2^{-4}P_{\rm orb}^{10/3}({\rm d})\ \ {\rm yr}$$

and

$$\tau_{\rm GR} = -\left(\frac{J}{\dot{J}}\right)_{\rm GR} = 3.8\times10^{11}\frac{(M_1+M_2)^{1/3}}{M_1M_2}P_{\rm orb}^{8/3}({\rm d})\ \ {\rm yr.}$$

Typical evolution timescales for CVs that evolve from $P_{\rm orb} \simeq 10\,$h to $P_{\rm orb} \simeq 3\,$h are $\sim 10^{8}\,$yr, and $\sim 10^{9}\,$yr to evolve through the period gap. Kolb & Stehle (1996) determined the age structure of a model population of Galactic CVs by applying standard models for the formation and the evolution of CVs and found that the systems above the period gap comprise young systems that typically formed less than $1.5\times10^{9}\,$yr ago, whereas the systems below the period gap have a typical age of $3-4\times10^{9}\,$yr.

At $P_{\rm orb} < 2\,$h, the orbital separation and mass of the donor star decrease; the mass loss timescale increases, but the thermal timescale increases much faster. When the mass loss timescale becomes shorter than the thermal timescale, the secondary star will not be able to shrink rapidly enough and it will therefore become oversized for its mass. When the mass of the secondary star becomes so low ($< 0.08\,M_{\odot}$) that hydrogen fusion terminates, the secondary star evolves towards a degenerate state and starts behaving like a white dwarf: its radius increases when

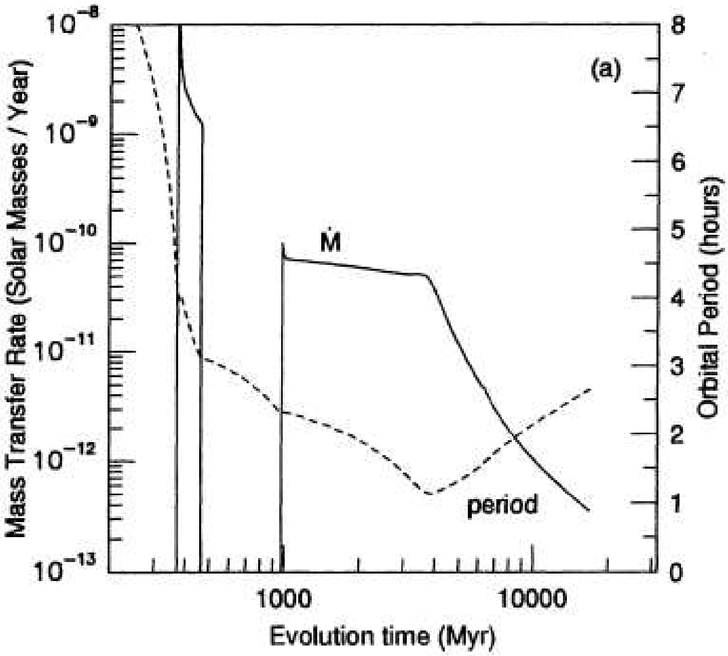

Figure 1.4: The evolution of the mass-transfer rate (solid line) and the orbital period (dashed line) of a CV, according to the disrupted magnetic braking model. At $P_{\rm orb} \gtrsim 3$ h, magnetic braking efficiently drives mass transfer with the rates of $\sim 10^{-9} - 10^{-8} M_{\odot}\,{\rm yr}^{-1}$. At $P_{\rm orb} \lesssim 2$ h, much lower mass-transfer rates of $\sim 10^{-11} - 10^{-10} M_{\odot}\,{\rm yr}^{-1}$ are caused by gravitational radiation. In the 2–3 h period range, mass transfer is completely shut-off. Taken from Howell et al. (1997).

its mass decreases. As a consequence, CVs reach their minimum period where the mass transfer timescale is about equal to the thermal timescale (e.g. Paczyński 1971; King 1988) within $\sim 10^9$ yr and evolve back to longer periods. The position of the minimum period depends on the thermal timescale of the secondary star and the mass transfer timescale, which depends particularly on the angular momentum loss rate. According to the standard scenario where gravitational radiation is the prevailing angular momentum loss mechanism for the short-period systems, the calculated minimum period is placed at ~ 65 min (Kolb & Ritter 1992; Howell et al. 1997; Kolb & Baraffe 1999); see e.g. Figure 1.5, middle panel. The mass transfer drops dramatically from $\sim 10^{-10}\,M_{\odot}\,{\rm yr}^{-1}$ to $\sim 10^{-12}\,M_{\odot}\,{\rm yr}^{-1}$ while CVs evolve back from the minimum period to $P_{\rm orb} \sim 2$ h within an evolution time of $\sim 10^{10}$ yr (e.g. Howell et al. 1997). The binaries then become too faint to be detected. Ultimately, the mass of the secondary star is reduced to that of a Jupiter-like object orbiting a white dwarf. A candidate for the systems that have evolved through the period minimum, or period bouncers, is WZ Sge with an orbital period of 81.6 min and an estimated mass of the donor star of $\sim 0.06\,M_{\odot}$ (Smak 1993; Patterson et al. 2002).

1.7 The contradictions between the standard model and observations

The disrupted magnetic braking model successfully explains the period gap found in the observed CV period distribution (Figure 1.2). A number of other predictions made by this model, however, are in strong disagreement with the observations. These severe contradictions are:

- Population synthesis studies estimate a large space density of galactic CVs in the range $\sim 2 \times 10^{-5} - 2 \times 10^{-4}\,\mathrm{pc}^{-3}$ (Ritter & Burkert 1986; de Kool 1992; Politano 1996). These predictions contrast with the properties of the observed CV population, with an estimated space density of $\sim 6 \times 10^{-6}\,\mathrm{pc}^{-3}$ (Ringwald 1996; Araujo-Betancor et al. 2005b). This indicates that we are missing a large fraction of the predicted CV population.

- The theory predicts a minimum period for hydrogen-rich CVs at $P_{\mathrm{orb}} \simeq 65$ min (e.g. Kolb & Ritter 1992; Howell et al. 1997; Kolb & Baraffe 1999); see Figure 1.5, middle panel, while the observed period distribution shows a sharp cut-off at $\sim 75 - 80$ min (e.g. Ritter & Kolb 2003; Knigge 2006); see e.g. Figure 1.2 and Figure 1.5 top panels.

- The standard model predicts that the evolution of the orbital period should slow down at the shortest periods, leading to a significant accumulation of systems near the minimum period (Figure 1.5, bottom panel), which is not observed (Kolb & Baraffe 1999).

- The population syntheses estimate that $\sim 99\%$ of the entire CV population should have $P_{\rm orb} < 2\,\rm h$, and of these, 70% should have passed the period bounce (e.g. Kolb 1993; Howell et al. 1997). However, the similar number of CVs are observed above and below the period gap (Figure 1.2, top panel).

- There is no observational evidence to support a discontinuous change in spin down rate between late-type field stars that are fully convective and those that have a radiative core (e.g. Sills et al. 2000; Andronov et al. 2003).

- As mass-transfer rates primarily depend on the timescale of angular momentum loss, this should lead to a strong correlation between observed mass-transfer rates and orbital periods. In contrast, the inferred mass-transfer rates show a significant dispersion at any given orbital period varying by about an order of magnitude from $\sim 10^{-10} - 10^{-9}\,M_{\odot}\,\rm yr^{-1}$ in dwarf novae to $\sim 10^{-9} - 10^{-8}\,M_{\odot}\,\rm yr^{-1}$ in novalike variables (Patterson 1984; Warner 1987). In addition, the lack of dwarf novae at the upper edge of the period gap indicates that the mass-transfer rate does not always decrease with the orbital period (Shafter 1992).

- The disrupted magnetic braking model predicts a narrower period gap for low mass-transfer systems than for high mass-transfer systems. In fact, the observed period gap of dwarf novae is twice as wide as that of CVs in general (Figure 1.2, third panel from bottom), as first pointed by Shafter (1992).

Despite having serious discrepancies with the observations, the widely accepted standard scenario of CV evolution has remained significantly unchanged since it was established two decades ago. A number of alternatives/modifications to the standard model have been proposed to explain these contradictions (e.g. Livio

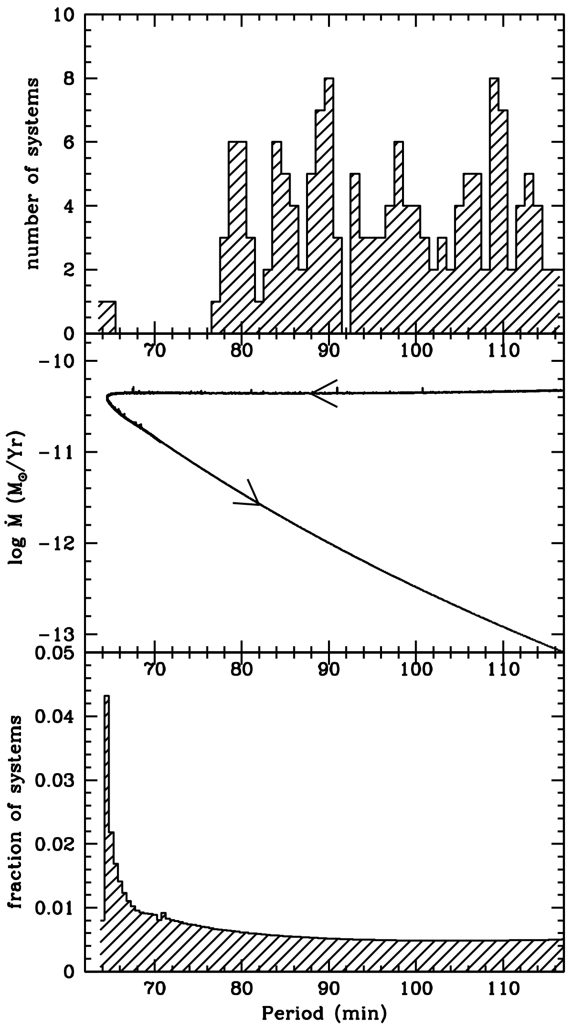

Figure 1.5: *Top panel:* the observed period distribution of known CVs with $P_{\rm orb} < 2$ h from Ritter & Kolb (1998). *Middle panel:* the calculated evolutionary track of CVs that evolve under the influence of angular momentum loss via gravitational radiation. The systems reach a minimum period at ~ 65 min and evolve back towards longer periods. *Bottom panel:* the predicted period distribution of CVs following the evolutionary track in the *middle panel* shows a spike at the minimum period which is absent in the observed distribution. Taken from Barker & Kolb (2003).

& Pringle 1994; King & Kolb 1995; Kolb et al. 1998; Patterson 1998; Clemens et al. 1998; McCormick & Frank 1998; Schenker et al. 1998; Kolb & Baraffe 1999;

Spruit & Taam 2001; Taam & Spruit 2001; Kolb et al. 2001; King et al. 2002; King & Schenker 2002; Schenker & King 2002; Andronov et al. 2003; Barker & Kolb 2003; Taam et al. 2003; Ivanova & Taam 2004; Willems et al. 2005; Matthews et al. 2006). However, none of them has been completely successful in matching all features found in the observed CV period distribution. A large number of these alternatives/modifications reflect the rather unsettled nature of CV evolution. Instead of revising the theoretical framework, the work presented in this thesis is mainly based on observational studies with the aim of establishing a homogeneously selected sample of CVs in order to improve our understanding of their evolution.

1.8 A large scale search for missing CVs and Pre-CVs

The standard model for the population of CVs predicts a vast number of short-period systems, $P_{\rm orb} < 2\,{\rm h}$ (e.g. Kolb 1993; Howell et al. 1997), and a high space density of $\sim 10^{-5} - 10^{-4}\,{\rm pc}^{-3}$ (Ritter & Burkert 1986; de Kool 1992; Politano 1996). Based on the current number, it seems that we know only a relatively small fraction ($\sim 1 - 10\%$) of the predicted population with an apparent lack of short-period systems. Possible reasons for these discrepancies are uncertainties in the theory of CV evolution (e.g. King 1988; Schenker & King 2002; Andronov et al. 2003; Barker & Kolb 2003; Taam et al. 2003), but also observational selection effects in the known CV population (e.g. Downes 1986; Ringwald 1996; Gänsicke 2005). In order to quantitatively test any theory of CV evolution, it is necessary to establish a large and unbiased sample of CVs as well as of their progenitors. I have been involved in a large search for new CVs in the Hamburg Quasar Survey (HQS), which pursues this aim.

1.8.1 The observational selection effects in the known population of CVs

One fascinating feature of CVs is that they are characterised by accretion activity onto a non-magnetic/magnetic white dwarf, which results in a wide range of observed phenomena, depending on the mass transfer rate and the nature of the white dwarf. These in turn provide various means to identify them. The known population of CVs in Figure 1.2 was discovered by one of the following methods:

Variability. One of the main features of CVs is variability. The brightness variations are clearly seen in classical novae and dwarf novae when they undergo outbursts and brighten up by several magnitudes. As a result, more than half of all known CVs have been discovered by variability surveys, either through professional sky patrols, or through the legions of amateur astronomers.

X-ray emission. CVs release a large amount of potential energy over a small volume close to the white dwarf, and therefore they are often X-ray emitters. This is especially true for magnetic CVs which emit most energy in a shock near the magnetic pole caps of the white dwarf. Consequently, many polars and intermediate polars are detected first as X-ray sources and subsequently identified as CVs (e.g. Beuermann et al. 1999; Gänsicke et al. 2005a).

Blue colour. In general, CVs contain a hot component in the form of the accretion disc/column and/or white dwarf. This makes them appearing as blue/ultraviolet excess objects in colour surveys, such as the Palomar-Green survey (Green et al. 1982; Ringwald 1996) or the Edinburgh-Cape Blue Object Survey (Stobie et al. 1997; Chen et al. 2001).

Emission lines. CVs may be discovered by their spectroscopic characteristic, i.e. the presence of relatively strong Balmer and helium emission lines (see Section 1.8.2 for details). So far, this criterion has been used only to a very limited extent; most of the 2-3 dozen spectroscopically selected CVs come from the first and second Byurakan surveys (see e.g. Stepanian et al. 1999).

Gänsicke (2005) divided the known CVs according to methods of their discovery, i.e. variability, X-ray emission, colour, and spectroscopic features, and found that the first three have bias towards different CV types: the variable CVs are dominated by dwarf/classical novae ($\sim 85\%$); more than 50% of the X-ray CVs are magnetic systems; and nearly 50% of the colour-selected CVs are novalike variables. Spectroscopic selection seems to be a viable method of finding CVs in an unbiased way.

1.8.2 Spectral characteristics of CVs

The spectrum of a CV is the superposition of the emission from the white dwarf, the secondary star, and the accretion disc/stream, with the relative strength of these three components varying dramatically between different types of CVs.

The white dwarf spectrum. Most white dwarfs in CVs have temperatures higher than $\sim 12\,000$ K (Sion 1999; Gänsicke 2000). They, therefore, emit the maximum radiation at short wavelengths, particularly in the ultraviolet band. The white dwarf spectra are characterised by a continuum with flux rising steeply in the blue, together with broad hydrogen absorption lines (Figure 1.6). The width of the lines results from pressure broadening due to high gravity in the white dwarf atmosphere.

The secondary star spectrum. As the donor stars in CVs are low-mass main-sequence objects with temperatures of ~ 3000 K, their maximum radiation is mainly emitted at red and infrared wavelengths. At such low temperatures, molecules are formed and therefore the spectrum of the donor star is dominated by broad absorption bands (Figure 1.6), with the most noticeable being titanium oxide (TiO).

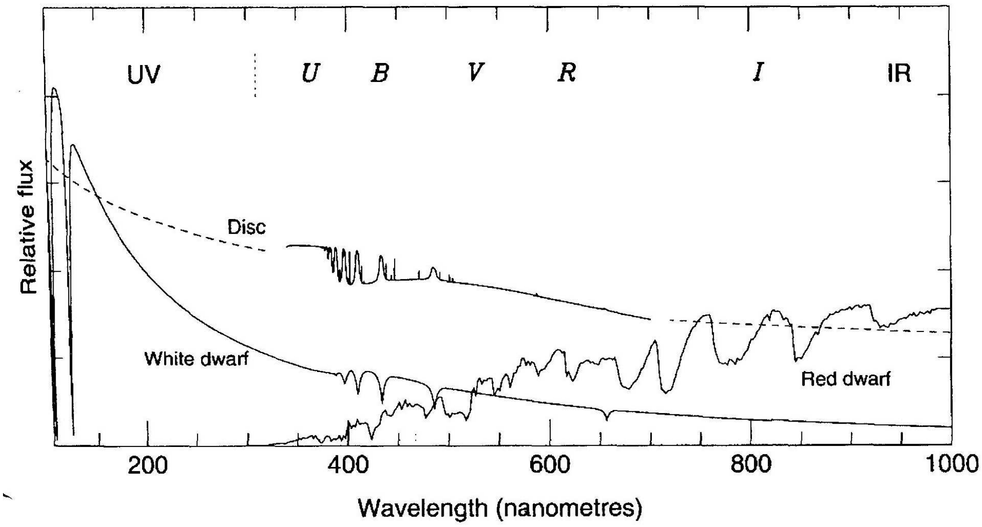

Figure 1.6: Schematic spectra of the components of a CV comprising that of a hot white dwarf, a cooler donor star, and a hot disc. The labels $UBVR$ and I show the regions of the spectrum in the different Johnson broadband filters. The dashed line is an approximation of the disc spectrum which is a sum of the blackbody radiations of different temperatures between outer and inner edges of the disc; the emission lines from a disc model are added up only in the optical region. Taken from Hellier (2001).

The accretion disc spectrum. The main contribution to the luminosity in most CVs is the accretion disc. The temperature of the disc varies in the range $\sim 3000 - 100\,000\,\mathrm{K}$ from outer edge to inner region, heating up by the release of gravitational potential energy. A rough approximation of the disc spectrum can be obtained by a sum of blackbody spectra of the appropriate temperature for each annulus which produces an overall flatter spectrum than that of the white dwarf (see Figure 1.6). Another approximation of the disc spectrum can be obtained, assuming that the disc radiates locally like a star of the same effective temperature and surface gravity, and then the disc spectrum can be synthesised by adding up a series of stellar spectra with the relevant range of parameters. In practice, spectra of most CVs are characterised by disc emission in which the continuum reaches a maximum in the ultraviolet and falls monotonically towards longer wavelengths, with the superimposition of prominent emission/absorption lines from low-ionisation states such as hydrogen (Paschen, Balmer, and Lyman series), helium (He I), calcium (Ca II), iron (Fe II), and oxygen (O I). Higher ionisation lines of He II as well as the Bowen fluorescence feature at 4640 – 4660 Å, caused by ionised carbon (C III) and nitrogen (N III), can be detected in the systems which have high mass-accretion rates such as novalike variables and magnetic CVs.

1.8.3 The selection effects in the HQS sample

About 75% of all known CVs have been discovered either because of their variability or because of their X-ray emission, with a strong dominance of dwarf novae and classical novae in the first group and magnetic CVs in the second group (Gänsicke 2005). It is therefore clear that CVs characterised by infrequent outbursts and/or low-amplitude variability, as well as lacking strong X-ray emission, will be under-represented in the currently known CV population. Hypothetically, such objects could make up for the large number of predicted short-period CVs with low mass-transfer rates. As a result, it is likely that the currently known sample of CVs may not represent the intrinsic population of CVs.

The primary purpose of our project to identify new CVs in the HQS is to establish a large homogeneously selected sample of systems that overcomes previously observational biases and that can subsequently be used to test our understanding of CV evolution. The efficiency of using the HQS to identify new CVs is fully investigated in Gänsicke et al. (2002b). I shall summarise below the main results of this test.

During the period of 1980 to 1997, the HQS, an objective-prism survey, was carried out with the 0.8 m Schmidt telescope at Calar Alto Observatory to search for bright quasars in the northern sky at high galactic latitudes, $\delta > 0^\circ$ and $|b| > 20^\circ$, covering $\approx 13\,600\,\mathrm{deg}^2$, with a dynamic range of $13 \lesssim B \lesssim 18.5$ (Hagen et al. 1995). The photographic plates cover a spectral range of $\sim 3400 - 5400$ Å with a resolution of ~ 45 Å at Hβ.

The HQS CV candidate selection made use of a property that has never been systematically exploited before: the *spectroscopic* hallmark of CVs, i.e. the presence of noticeable emission lines in most CVs. The CV candidate selection was carried out by visually inspecting 48708 HQS prism spectra for the presence of Balmer emission lines. In order to test the efficiency of this method, the authors applied the same procedure to the subset of 84 previously known CVs (Downes et al. 2001, as of July 2001) that are contained in the HQS spectral data base. They positively recovered $\simeq 90\%$ of the known short-period ($P_{\rm orb} \lesssim 3$ h) CVs (Figure 1.7), including prominent dwarf novae such as SW UMa or T Leo (the latter one has a rather long outburst cycle of ~ 420 d), as well as magnetic CVs, such as AN UMa or ST LMi. The fraction of recovered systems drops to $\simeq 55\%$ for long-period systems, with the largest fraction of missed identifications being novalike variables with weak or no Balmer emission lines. In total, 62% of the previously known CVs with an HQS prism spectrum were positively identified by the spectroscopic selection method. The authors concluded from this test that the HQS should be very efficient in finding CVs below the period gap, as long as they have similar spectroscopic properties to the previously known systems, i.e. Balmer emission lines with equivalent widths > 10 Å in Hβ. The decrease in detection efficiency for long-period systems has been compensated to some extent by follow-up programs investigating hot stars in the HQS, delivering a number of new CVs with weak emission lines (Heber et al. 1991).

In total, 53 new CVs and pre-CVs were identified within this project, and 12 CV candidates still await additional spectroscopic confirmation (Figure 1.8). Substantial observational effort was invested in determining the properties of these systems. To date, 44 HQS CVs/pre-CVs have had their orbital period measured, including nine new CVs and a pre-CV presented in this thesis.

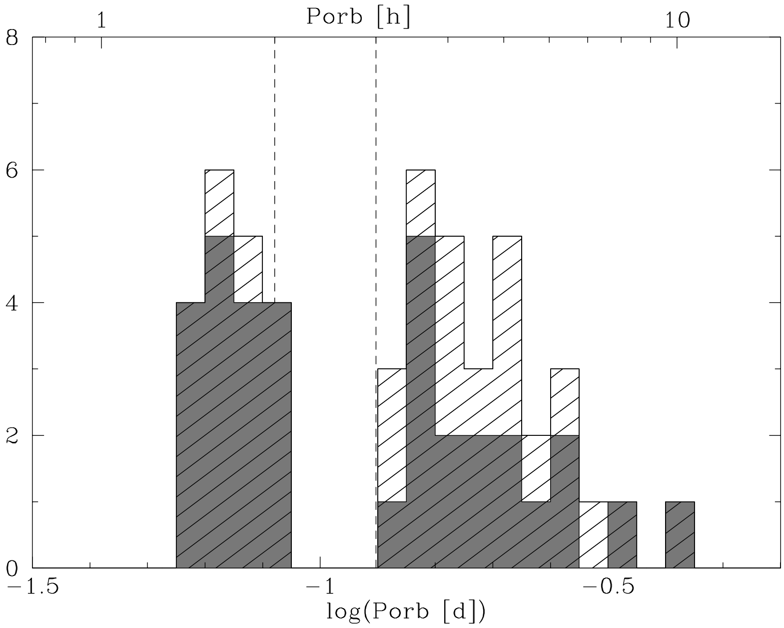

Figure 1.7: Orbital period distribution of the previously known CVs from Downes et al. (2001) contained in the HQS spectral data base (white shade) and those correctly recognised (grey shade) by our spectroscopic selection criterion, i.e. the detection of Balmer emission lines. Data are provided by B. Gänsicke.

1.9 Future chapters

In the next chapter, I provide a description of the observations and the data reduction used throughout this thesis. The technique of time-series analysis for the orbital period measurement is described in Chapter 3. In Chapters 4–6, I present the results of my contribution to the large scale search for new CVs/pre-CVs from the HQS. Specifically, Chapter 4 presents four new long-period CVs, HS 0139+0559, HS 0229+8016, HS 0506+7725, and HS 0642+5049, that all have orbital periods in the range of 3–4 h, but greatly differ in their observed properties. The discovery of five new dwarf novae, HS 0417+7445, HS 1016+3412, HS 1340+1524, HS 1857+7127, HS 2214+2845 with orbital periods spanning from ~ 1.5 h to nearly 5 h are described in Chapter 5. In Chapter 6, the nature of one of the youngest pre-CVs containing a very hot white dwarf, HS 1857+5144, with an orbital period of ~ 6.5 h is investigated. Finally, I discuss the overall status of the survey in Chapter 7

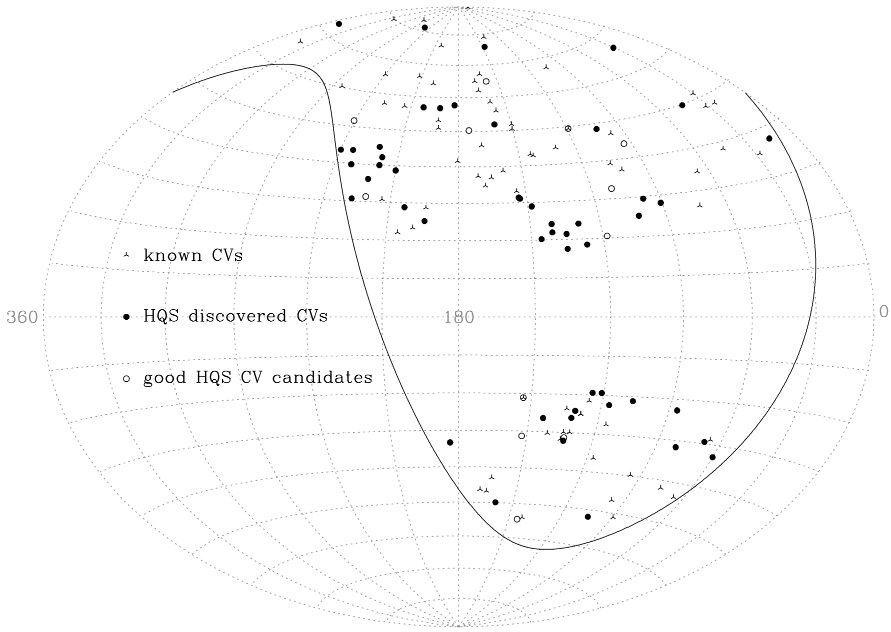

Figure 1.8: Galactic distribution of CVs/pre-CVs from the HQS covering the northern hemisphere ($\delta > 0^\circ$, indicated by the solid line and $|b| > 20^\circ$). The new HQS CVs/pre-CVs are displayed as filled dots. The promising CV candidates are shown in open circles. Flake triangles are previously known CVs from Downes et al. (2001) that are contained in the HQS spectral data base. Provided by B. Gänsicke.

and summarise the thesis in Chapter 8.

Chapter 2

Observations and data reduction

The major goal of our search for new CVs in the HQS is to construct the orbital period distribution of this sample that should overcome the incompleteness of the orbital period distribution of the previously known CV population. In order to achieve this goal, time-series photometric and spectroscopic observations are mandatory. In practice, the orbital periods of CVs can be obtained by measuring the periodicity of variability associated with changing geometry of the system as the binary rotates around its centre of mass or as the white dwarf spins, e.g. photometric variability found in high-inclination systems or spectroscopic variation based on the Doppler shifts found in observed spectral lines.

During the course of this large scale project, time-resolved photometric and spectroscopic observations have been carried out using various ground-based telescopes. The data in this thesis is part of a substantial effort and dedication by the team in Warwick that I have been a member of. Since December 2003, however, all time-resolved spectroscopic and photometric observations obtained at Calar Alto observatory were collected by myself, except one occasion in February 2005 in which spectroscopic observations were carried out in service mode. In addition, I carried out all photometric observations obtained after December 2003 at the Observatorio del Roque de los Muchachos, the Observatorio del Teide, and one observing run in May/June 2006 at Kryoneri Observatory. These photometric data were reduced by myself using Gänsicke et al. (2004a)'s pipeline. Spectroscopic data reduction was performed by P. Rodríguez-Gil, S. Araujo-Betancor, and J. Southworth.

In the following section, I outline the general principle of CCD (charge-coupled device) observations and data reduction, focusing on the techniques applied to the observations presented here. In Section 2.2, I provide the details on the observations and the data reduction for the new HQS CVs/pre-CV presented in this thesis, which are HS 0139+0559, HS 0229+8016, HS 0417+7445, HS 0506+7725, HS 0642+5049, HS 1016+3412, HS 1340+1524, HS 1857+5144, HS 1857+7127, and HS 2214+2845.

2.1 An overview of CCD observations and data reduction

2.1.1 CCD photometry

Photometry is a technique of measuring the flux from a number of stars in the field of view. Absolute photometry requires very good atmospheric conditions and detailed calibrations. Differential photometry measures the variation in brightness of a given star relative to one or more comparison stars, and it can also be carried out under non-photometric conditions. To search for photometric variability of our objects, all photometric observations presented in this thesis were carried out on the basis of differential photometry. In our observations, CCD cameras with typical arrays of less than one million to a few million pixels, were used to record images of the sky of a few arcseconds to a few tens of arcminutes. A CCD is a semiconductor device in which incoming photons create free electrons via the photoelectric effect. At the end of an exposure these charges are read out by being electronically shifted from pixel to pixel towards the end of the device. The output signal will then be electronically converted from analogue voltage to digital counts and fed into a computer, producing a two-dimensional image.

Figure 2.1a shows a simple diagram of the optical elements of the Calar Alto Faint Object Spectrograph (CAFOS) on the Calar Alto 2.2 m telescope, comprising a slit, a grism, a filter, and a CCD camera which is used as a detector to record the light from the stars. For a photometric observation, the slit and grism are moved out of the beam and images are taken as shown in Figure 2.1b for a specific filter. Six filters are mounted in a filter-wheel, which we typically filled with the Johnson *UBVRI* broadband filters plus a clear slot for white light photometry.

In practice, for each night of the observation before taking a long series of target frames, we normally need to take bias, flat-field, and dark (if necessary) images which will be used in the data reduction process (see Section 2.1.3 for details).

2.1.2 CCD Spectroscopy

An efficient method to determine the orbital periods of CVs is to measure radial velocity variations from a series of spectra. These Doppler shifts of the spectral lines result from the orbital motion of the absorbing or emitting material within the systems. In practice, such spectra can be obtained by the technique of spectroscopy which measures the wavelength dependence of the flux emitted by stars using a spectrograph. In principle, the spectrograph allows an image of a slit to be dispersed and then re-imaged onto the CCD detector. A typical astronomical spectrograph comprises an entrance slit placed in the focal plane of the telescope, an internal light source for flat fielding and an arc lamp for wavelength calibration sources, a collimator, a dispersing element, and an imaging device, or camera optic to bring the spectrum to a focus onto the CCD detector. The collimator and spectrum imager may either be in the forms of lenses or mirrors. The dispersing element is normally either a glass prism, a diffraction grating, or a grism. In our time-resolved spectroscopic observations, grisms and gratings were used as a dis-

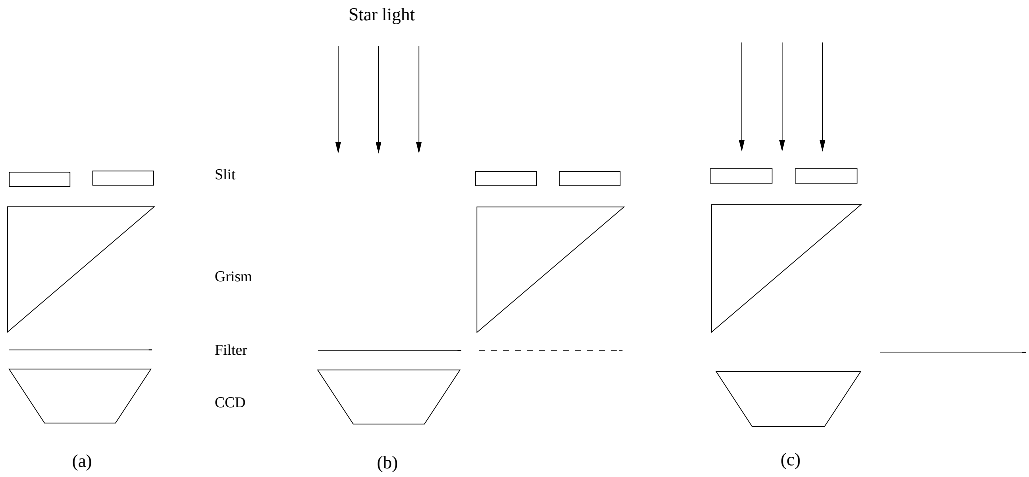

Figure 2.1: Schematic views of the different optical elements of CAFOS is illustrated in (a). The instrument configurations used for CCD photometric and spectroscopic observations are shown in (b) and (c), respectively.

persing element to provide intermediate/high spectral resolutions.

Figure 2.1c presents a simple schematic view of spectroscopic observations using CAFOS. In this case, the filter is moved out of the beam; star light is narrowed by a slit and is dispersed by a grism, and the final spectrum is then imaged onto the CCD detector.

Like the photometry, spectroscopic observation needs bias and flat-field frames to correct the two-dimensional images in the reduction process. Furthermore, exposures of arc lamps containing numerous spectral lines with accurately known wavelengths are required for wavelength calibration procedure.

2.1.3 CCD data reduction

The aim of CCD data reduction is to remove undesirable effects inherent into the CCD structure in the raw images and to translate the two-dimensional data recorded by the CCD into either one-dimensional data (i.e. a spectrum) or zero-dimensional data (i.e. a magnitude). In general, the process of the CCD reduction is carried out in the following steps which can be applied to both photometric and spectroscopic observations: (a) bias-subtraction, (b) dark current-subtraction (if necessary), and (c) flat-field correction. However, as all spectroscopic data were reduced by members of the team, it is then beyond the scope of this thesis to indulge into the details of spectral extraction. In this thesis, I shall focus on the description of photometric data reduction only.

Bias-subtraction. The bias level is an electronic offset added to the signal from the CCD to avoid negative numbers in the readout process. In general, the bias level can be removed simply by subtracting from each pixel across the CCD either a mean value determined from the overscan region (a number of columns which are not exposed to light) or subtracting a two-dimensional mean bias frame. All data that I reduced in this thesis were bias-corrected by subtraction of a mean bias frame. Bias frames can be obtained readily by taking exposures with zero exposure time and with the shutter closed. In practice, we take ten bias-frames or more to combine them into an average bias frame (e.g. Figure 2.2a). This mean bias image will be subtracted from each raw image as the first step in the data reduction.

Dark current-subtraction. Dark current-subtraction is the removal of electron counts which accumulate in each pixel due to thermal noise in the CCD chip. The number of dark counts is proportional to the exposure time. To correct for the dark current, we need a calibration image from a set of dark frames which can be obtained by taking exposures with the shutter closed. In modern CCDs, the dark current is so low that long dark exposures need to be obtained, and the resulting dark current rate is then scaled to the exposure time of the science images. In practice, apart from the detector at the Kryoneri 1.2 m telescope, all CCDs used for observations in this project were cooled down to very low temperatures in which the thermal noise was negligible. Our reduction then does not need to take into account the dark current correction. For the Kryoneri data, where the dark current is significant (~ 0.67 cts/sec), after the process of bias-subtraction, we subtracted the dark current with an average dark frame (e.g. Figure 2.2b) of three individual dark frames with an exposure time of 10 min.

Flat-fielding. CCDs do not have a uniform response to a constant flux of light across their surface. This may be caused either by the fabrication process or by optical attenuation effects such as dust on the CCD entrance window. This spatial sensitivity variation must be removed by flat-fielding. To create flat-field images, we need to illuminate the CCD with a uniform source of light using the same filter (photometry) or grism/grating (spectroscopy) as in the science frames. In practice, for CCD imaging, the flat-field frames are obtained either by using a tungsten lamp that illuminates a flat-field screen mounted inside the dome (dome flat), or using the twilight sky as a uniform light source (sky flat). For spectroscopic observations, flat-field spectra are usually obtained via illumination from a tungsten lamp located inside the spectrograph before the entrance slit. Typically, five to ten flats should be taken for each filter or grism/grating to be used for the data reduction procedure. An average flat-field frame (e.g. Figure 2.2c) is derived from these exposures. The average flat-field frame is then scaled to a mean value of unity with small deviations from the mean value which reflect the response variations of each pixel on the array. The object frames are simply divided by this mean flat-field frame.

Figures 2.2a–c show a sample of the average CCD frames (bias, dark, and flat-field) used for photometric data reduction. The pre-processed and corrected images are shown in Figure 2.2d and Figure 2.2e, respectively.

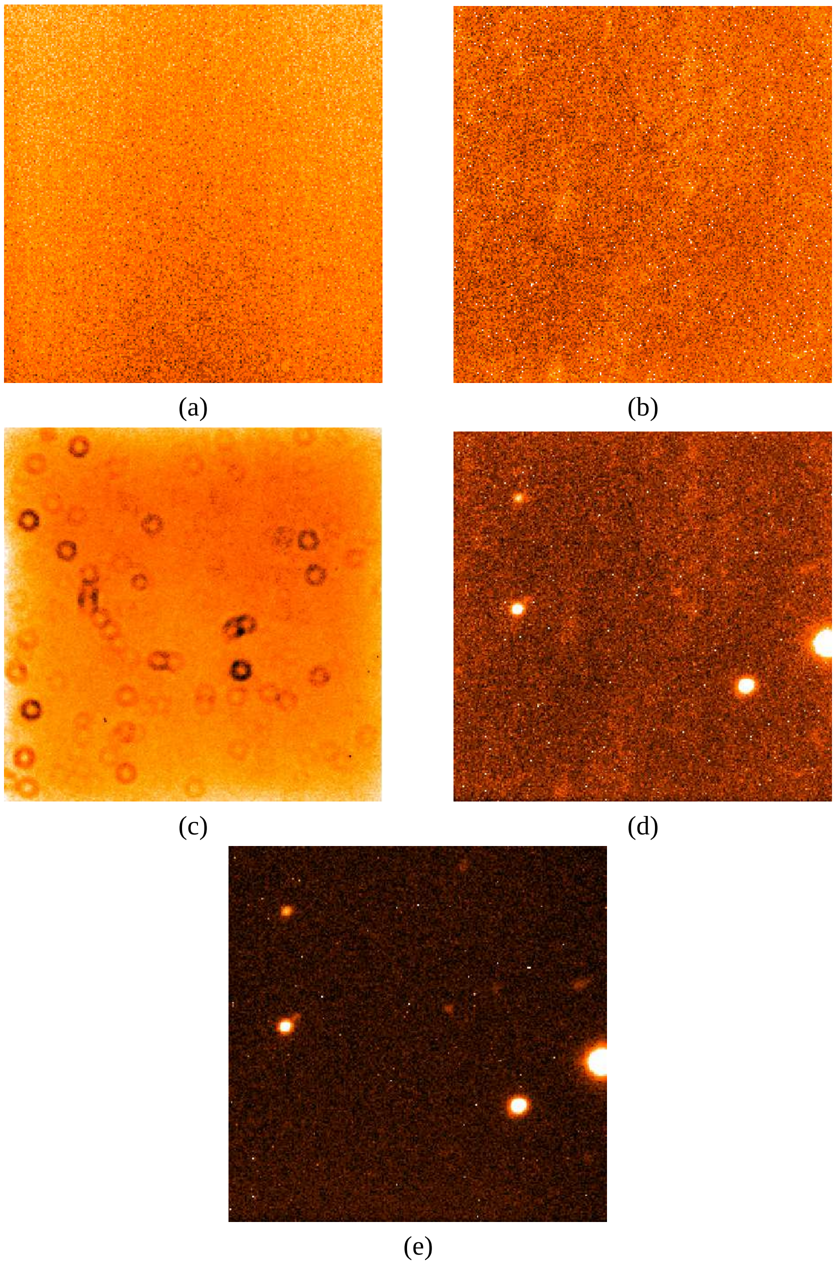

Figure 2.2: A sample of different types of 516 × 516 pixel CCD frames obtained at the Kryoneri 1.2 m telescope. (a) A mean bias frame averaged from ten individual bias images. (b) An average dark frame derived from three individual dark frames with an exposure time of 10 min. (c) A mean flat-field frame obtained from ten individual flat-field images. Note that donut-shaped attenuations result from dust/condensation on the CCD window. (d) A raw image comprises an object of interest and comparison stars in the same field. (e) A corrected image after bias- and dark-subtraction and flat-fielding. Note that figures (d) and (e) are displayed in the same dynamical range of 180 cts around the median count level.

2.2 Observations and data reduction for new ten HQS CVs/pre-CV

2.2.1 Spectroscopy

During 1981 to 1996, in the course of finding bright quasars in the northern sky by the HQS, low resolution spectra of the new ten CVs/pre-CV presented in Chapters 4–6 were obtained in the form of objective prism plates at the Calar Alto 0.8 m Schmidt telescope. Additional intermediate resolution identification spectroscopy of these objects was carried out at the Calar Alto Observatory throughout the period January 1989 to May 2001. In order to measure the orbital periods of the newly identified CVs/pre-CVs, follow-up time-resolved spectroscopy of HS 0139+0559 (56 spectra), HS 0229+8016 (74 spectra), HS 0506+7725 (76 spectra), HS 0642-+5049 (87 spectra), HS 1016+3412 (70 spectra), HS 1340+1524 (78 spectra), HS - 1857+5144 (35 spectra), HS 1857+7127 (41 spectra), and HS 2214+2845 (41 spectra) was performed at the Calar Alto Observatory, the Roque de los Muchachos Observatory, and the McDonald Observatory throughout the period September 2000 to July 2006. The follow-up spectroscopy was obtained in 600 s exposures, interleaved with arc calibrations every ~ 40 min to correct for instrument flexure. Flux standards were observed at the beginning and the end of the night – weather permitting – to correct for the instrumental response. The details of the instrument setup and data reduction are described below. Table 2.1 presents the details of the observations, along with the observers.

Calar Alto observatory. The Centro Astronómico Hispano Alemán (CAHA) at Calar Alto is located in the Sierra de Los Filabres north of Almeria at 2168 m height above sea level. It is operated jointly by the Max-Planck Institut für Astronomie (MPIA) in Heidelberg, Germany, and the Instituto de Astrofísica de Andalucía (CSIC) in Granada, Spain. During January 1989 to May 2001, intermediate resolution identification spectra of CV/pre-CV candidates were obtained mainly at the 2.2 m telescope except one occasion in January 1989 when the observation was carried out at the 3.5 m telescope as part of a program to find blue stars (Heber et al. 1991). Before the 1996 observing period, the telescopes were equipped with Boller & Chiven spectrographs, which were used in conjunction with 120Å/mm gratings. For the observations carried out after 1996, the CAFOS spectrograph in conjunction with either the B-400 or the B-200 grism and a 1.5″slit were used to record the spectra onto a 2k $\times$ 2k pixel SITe CCD. These identification spectra were reduced with the `MIDAS`[1] quicklook context available at the Calar Alto.

Additional time-resolved spectroscopy was obtained both at the 2.2 m telescope and at the 3.5 m telescope. At the 2.2 m telescope, we used CAFOS equipped with the G-100 grism and a 2k $\times$ 2k pixel SITe CCD to obtain the spectra of HS 0139+0559, HS 0229+8016, HS 0506+7725, HS 0642+5049, HS 1016+3412, HS 1340+1524, and HS 1857+7127. This setup, in conjunction with a 1.2″slit, provided a spectral resolution of $\sim$ 4.1 Å (full width at half maximum, FWHM), covering the wavelength range 4240–8300 Å. The B-100 and R-100 grisms along with a 1.5″slit were also used on one occasion (September 2000) to observe HS 2214+2845, which provided a resolution of $\sim$ 4 Å (FWHM) over the range 3500–6300 Å and 6000–9200 Å for the B-100 and R-100 grisms, respectively. At the 3.5 m telescope, the double-armed TWIN spectrograph equipped with the T05 grating in the blue and the T06 grating in the red was used to obtain the spectra of HS 0139+0559 and HS 0506+7725. This setup provided a spectral resolution of $\sim$ 1.2 Å (FWHM) in the ranges $\lambda\lambda 3810-4940$ and $\lambda\lambda 6440-7510$, respectively.

Observatorio del Roque de los Muchachos. The Observatorio del Roque de los Muchachos, on the island of La Palma, Spain, is located at 2400 m above sea level. The telescopes used in our observations were the 2.5 m Isaac Newton Tele-

[1]ESO-MIDAS is developed and maintained by the European Southern Observatory.

scope (INT) and the 4.2 m William Herschel Telescope (WHT). At the INT, the Intermediate Dispersion Spectrograph (IDS) together with a $2k \times 4k$ pixel EEV10a detector was mounted to carry out time-resolved spectroscopy of HS 0642+5049, HS 1016+3412, HS 1340+1524, HS 1857+7127, and HS 2214+2845. The R632V grating and a slit width of $1.5''$ provided a spectral resolution of ~ 2.3 Å (FWHM) and a useful wavelength range of $\sim 4400 - 6800$ Å. At the WHT, four high resolution spectra of HS 1857+5144 were obtained using the Intermediate Dispersion Spectrograph and Imaging System (ISIS) spectrograph together with the R1200B and R600R gratings on the blue and the red arms, providing a spectral resolution of $\simeq 1$ Å (FWHMs) over the wavelength range 4200–5000 Å, and 7500–9100 Å, respectively.

McDonald Observatory. The McDonald observatory is located on Mount Locke in Austin, Texas, at 2076 m above sea level. In our observations, the 2.7 m Harlan J. Smith telescope, owned by the University of Texas at Austin, was equipped with the Large Cassegrain Spectrograph (LCS). Time-series, intermediate resolution spectra of HS 1857+5144 were performed through a $1''$ slit and grating #43 and imaged onto the 800×800 pixel TI1 CCD camera. This setup provided access to the $\lambda\lambda 3670 - 5050$ wavelength range at 3.5 Å (FWHM) spectral resolution.

Time-resolved spectroscopic data reduction. The data reduction of the follow-up spectroscopy consisting of bias and flat-field corrections. Optimal extraction of the spectra (Horne 1986) was carried out using standard long-slit spectroscopy packages within `IRAF`[2] and using the `Figaro` package within `Starlink`. The wavelength calibration of the extracted spectra was performed in the program `Pamela` and `MOLLY` written by T. Marsh[3]. The dispersion relation was obtained by fitting

[2] `IRAF` is distributed by the National Optical Astronomy Observatories, which are operated by the Association of Universities for Research in Astronomy, Inc., under cooperative agreement with the National Science Foundation.

[3] www.warwick.ac.uk/go/trmarsh

a low-order polynomial to the arc lines, with the RMS less than one tenth of the reciprocal dispersion per pixel in all cases. The flexure of the telescope was accounted for by interpolating between the two arc exposures bracketing the target spectra. All time-resolved spectroscopic data presented in this thesis were reduced by P. Rodríguez-Gil except the August/September 2002 IDS and the April 2003 CAFOS spectra which were processed by S. Araujo-Betancor, and the July 2006 WHT spectra which were reduced by J. Southworth.

2.2.2 Photometry

The spectroscopy of the ten new CVs/pre-CV was supplemented by differential CCD photometry throughout the period December 1999 to June 2006 for a total of 92 nights using ten different telescopes (see Table 2.1 for the details of the observations). The individual objects (see finding charts in Appendix A) were observed for $\sim$ 8 h (HS 0139+0559), $\sim$ 15 h (HS 0229+8016), $\sim$ 25 h (HS 0417+7445), $\sim$ 34 h (HS 0506+7725), $\sim$ 24 h (HS 0642+5049), $\sim$ 14 h (HS 1016+3412), $\sim$ 68 h (HS 1340+1524), $\sim$ 65 h (HS 1857+5144), $\sim$ 50 h (HS 1857+7127), and $\sim$ 48 h (HS 2214+2845). Brief descriptions of the instrumentation and the data reduction techniques used are given below. Unless stated otherwise, the data reduction was carried out by myself using the pipeline described by Gänsicke et al. (2004a), which employs `MIDAS` for bias and dark-current (if necessary) subtraction and flat-fielding, and performs aperture photometry over all visible objects in the field using `Sextractor` (Bertin & Arnouts 1996). The USNO-A2.0 magnitudes of the comparison stars used to obtain differential photometry of the HQS targets are listed in Table 2.1; see the finding chart in Appendix A for their identifications.

Additional images of HS 0417+7445, HS 1016+3412, HS 1340+1524, and HS 2214+2845 were taken by P. Schmeer intermittently during the period May 2004 to April 2005 using the 0.37 m robotic Rigel telescope of the University of Iowa which is equipped with a 1k $\times$ 1k pixel SITe-003 CCD camera. For all four systems, filterless images with an exposure time of 25 s were obtained.

Braeside Observatory. The Braeside Observatory is a privately operated astronomical research facility located five miles West of downtown Flagstaff, Arizona, at 2238 m above sea level. At the Braeside Observatory, we used the 0.41 m reflector telescope together with a SITe 512 $\times$ 512 pixel CCD camera to obtain differential photometry of HS 0139+0559 and HS 2214+2845. The photometric reduction (bias-subtraction, dark current-subtraction, and flat-fielding) was performed by R. Fried in a standard way using a custom-made software suite.

Astrophysikalisches Institut Potsdam. The AIP 0.7 m telescope is built in the west dome of the main building at Sternwarte Babelsberg in Potsdam, Germany, at an elevation of 66 m above sea level. During our observations, the telescope was mounted with a 1k $\times$ 1k pixel SITe CCD detector to record *R*-band images of HS 1340+1524 and HS 1857+7127. The AIP data were reduced by R. Schwarz using a pipeline written on top of the Point Spread Function (PSF)-fitting program `DoPhot`.

Tuorla Observatory. The Tuorla Observatory is located at Tuorla and owned by University of Turku, Finland. During our observations, the 0.7 m Schmidt-Vaisala telescope was equipped with an SBIG ST-8 CCD camera to obtain the differential filterless photometry of HS 0229+8016, HS 0506+7725, and HS 0642+5049.

Wendelstein Observatory. The Wendelstein Observatory is situated on the summit of Mount Wendelstein in the Bavarian Alps, at an altitude of 1845 m above sea level. It is operated by the Institute for Astronomy and Astrophysics of the University of Munich, Germany. At the Wendelstein Observatory, we used the 0.8 m telescope to observe HS 0417+7445. The data were obtained through a Bessel *B* filter and in white light using the MONICA CCD camera (Roth 1992). The raw images were processed by B. Gänsicke.

Observatorio del Teide. The Observatorio del Teide is located at a height of 2400 m on Mount Teide, Tenerife, Spain, and operated by Instituto de Astrofísica de Canarias (IAC). At the Observatorio del Teide, the 0.82 m IAC80 telescope, operated by the IAC, and the 1 m Optical Ground Station (OGS) telescope, operated by the European Space Agency were used as main telescopes for our observations. The telescopes were equipped with Thomson 1k $\times$ 1k pixel CCD cameras. The filterless data of HS 0506+7725, HS 0642+5049, HS 1016+3412, HS 1340+1524, HS 1857+7127, and HS 2214+2845 were taken using 2×2 binning and windowing to improve the time resolution. The 2003 images were processed by P. Rodríguez-Gil, who performed bias and flat-fielding corrections within IRAF and extracted the instrumental magnitudes using PSF-fitting packages. The 2004/2005 images were reduced by myself using Gänsicke et al. (2004a)'s pipeline.

Fred Lawrence Whipple Observatory. Located near Amado, Arizona, on Mount Hopkins at an altitude of 2250 m above sea level, the Fred Lawrence Whipple Observatory (FLWO) is operated by the Smithsonian Institution. At the FLWO, we carried out filterless differential photometry of HS 1340+1524 and HS 1857+7127 using the 1.2 m telescope. Throughout our observations, the telescope was equipped with the 4-Shooter CCD camera, an array of four 2k $\times$ 2k pixel detectors, and only a small part of the CCD#3 was read out. The raw images were processed by P. Rodríguez-Gil within IRAF in an analogous manner as described for the 2003 IAC80 and OGS data reduction.

Hamburg Observatory. The Hamburger Sternwarte is an astronomical observatory located in Bergedorf near Hamburg and owned by the University of Hamburg, Germany. The 1.2 m Oskar Lühning Teleskop (OLT), the largest telescope at the observatory, was equipped with a 1k $\times$ 1k pixel SITe to obtain Johnson *R*-band photometry of HS 0417+7445. The OLT images were reduced by B. Gänsicke.

Kryoneri Observatory. Located at Kryoneri Korinthias on the top of mountain Kilini at 930 m above sea level, the Kryoneri Observatory is owned by the National Observatory of Athens (NOA), Greece. At the Kryoneri observatory, photometric observations of HS 0229+8016, HS 0506+7725, HS 1016+3412, HS 1340+1524, HS 1857+5144, HS 1857+7127, and HS 2214+2845 were carried out with the 1.2 m telescope together with Photometrics SI-502 516 $\times$ 516 pixel CCD camera throughout our observing runs. All raw data were processed by B. Gänsicke except the data sets obtained during May/June 2006 which were reduced by myself.

Calar Alto Observatory. Throughout the period of time-resolved photometric observations of HS 0506+7725, HS 0642+5049, and HS 1340+1524 obtained at the Calar Alto observatory, the CAFOS spectrograph with the SITe 2k $\times$ 2k pixel CCD camera on the 2.2 m telescope was used in the imaging mode. The images were taken only over a small part of the CCD to improve the time resolution. The data obtained in January/May 2003 were reduced by B. Gänsicke and S. Araujo-Betancor, respectively. For the 2004 data, the raw images were processed by myself.

Observatorio del Roque de los Muchachos. The 2.5 m INT on La Palma was equipped with the Wide Field Camera (WFC) to obtain Sloan g'-filter photometry of HS 0417+7445. The detector comprises an array of four EEV 2k $\times$ 4k pixel CCDs. Binning and windowing are not possible at this telescope, resulting in a dead time of $\sim$ 42 s per observation. Each WFC image comprises the images of four CCDs. The target of interest was centred on CCD 4. In the data reduction process, a small region of the centre of the CCD 4 was extracted in IRAF and then those raw images were processed using Gänsicke et al. (2004a)'s pipeline.

Table 2.1: Log of the observations.

Date	UT	Telescope[a]	Filter/ Grism	Exp. (s)	Frames	Comp.[b] star	Observer[c]
HS 0139+0559							
1981 Nov 01		CA08	Prism	3600	1	-	
1981 Nov 02		CA08	Prism	3600	1	-	
1989 Jan 22	19:21	CA35	120Å/mm	900	1	-	HJH
1999 Dec 30	02:15-07:04	BS	*R*	70	293	:	RF
2000 Jan 04	02:31-06:04	BS	*B*	50	136	:	RF
2002 Oct 28	23:53-00:03	CA35	T08/T01	300	1	-	BG
2002 Oct 29	22:36-03:21	CA35	T05/T06	600	16	-	BG
2003 Dec 24	18:25-00:10	CA22	G-100	600	27	-	AA
2003 Dec 26	18:34-20:48	CA22	G-100	600	12	-	AA
HS 0229+8016							
1986 Nov 05		CA08	Prism	3600	1	-	
1986 Nov 06		CA08	Prism	3600	1	-	
1992 Aug 08	03:16	CA22		900	1	-	HJH
1994 Nov 12		CA08	Prism	3600	1	-	
1998 Oct 05	01:37	CA22	B-200	1800	1	-	HJH
2002 Sep 20	01:30-03:28	KY	*R*	5	840	C1	SK
2002 Sep 20	22:37-03:27	KY	*R*	5	1680	C1	SK
2003 Jan 10	15:41-23:45	TO	Clear	30	695	C1	HL
2003 Dec 14	19:18-00:55	CA22	G-100	600	24	-	BG & AA
2003 Dec 16	20:21-03:08	CA22	G-100	600	27	-	BG & AA
2003 Dec 23	18:49-21:01	CA22	G-100	600	12	-	AA
2003 Dec 26	21:34-22:53	CA22	G-100	600	7	-	AA

Continued on next page

Date	UT	Telescope[a]	Filter/ Grism	Exp. (s)	Frames	Comp.[b] star	Observer[c]
2003 Dec 27	18:46-19:22	CA22	G-100	600	4	-	AA
HS 0417+7445							
1992 Jun		CA08	Prism	-	1	-	
1995 Oct		CA08	Prism	-	1	-	
1996 Oct 05	02:52	CA22	B-400	600	1	-	
2000 Dec 21	22:41-02:37	WD	*B*	240	53	C2	HB
2001 Jan 14	00:40-04:40	WD	*B*	240	54	C2	HB
2003 Feb 27	20:35-23:47	OLT	*R*	300	37	C3	DE
2004 Nov 12	17:40-02:03	WD	Clear	150	162	C3	HB
2005 Jan 03	02:18-04:40	INT	g'	80	71	C3	AA
2005 Jan 04	23:07-02:27	INT	g'	30-35	162	C3	AA
HS 0506+7725							
1987 Oct 29		CA08	Prism	3600	1	-	
1994 Jan 12		CA08	Prism	3600	1	-	
1995 Oct 23		CA08	Prism	3600	1	-	
1998 Feb 02	19:43	CA22	B-400	180	1	-	HJH
2002 Oct 08	22:46-01:25	KY	*R*	10	599	C4	CP
2002 Dec 03	03:22-05:09	CA35	T05/T06	600	10	C4	BG
2002 Dec 09	00:19-00:30	CA22	G-100	600	2	C4	BG
2003 Jan 01	01:01-03:24	CA22	*V*	30	85	C4	SAB
2003 Jan 04	16:13-20:16	TO	Clear	120	32	C4	HL
2003 Jan 06	15:47-20:46	TO	Clear	60	213	C4	HL
2003 Jan 16	20:18-22:40	TO	Clear	60	115	C4	HL
2003 Nov 15	03:21-06:37	OGS	Clear	5	1110	C4	PRG
2003 Dec 13	23:25-03:53	CA22	G-100	600	23	C4	BG & AA

Continued on next page

Date	UT	Telescope[a]	Filter/ Grism	Exp. (s)	Frames	Comp.[b] star	Observer[c]
2003 Dec 15	01:34-06:13	CA22	G-100	600	23	C4	BG & AA
2003 Dec 16	00:05-05:11	CA22	Clear	15-30	346	C4	BG & AA
2003 Dec 17	03:40-05:57	CA22	G-100	600	12	-	BG & AA
2003 Dec 23	22:19-00:31	CA22	G-100	600	12	C4	AA
2003 Dec 25	19:15-02:29	CA22	Clear	15-30	296	C4	AA
2003 Dec 26	02:52-03:28	CA22	G-100	600	4	-	AA
2003 Dec 27	04:03-06:16	CA22	Clear	20	149	C4	AA
2003 Dec 27	20:33-23:55	CA22	Clear	20	288	C4	AA
HS 0642+5049							
1991 Nov 10		CA08	Prism	3600	1	-	
1993 Oct 24		CA08	Prism	3600	1	-	
1999 Mar 07	19:11	CA22	B-400	300	1	-	
2003 Apr 25	21:21-22:14	INT	R632V	600	6	-	PRG
2003 Apr 26	21:17-21:49	INT	R632V	600-900	4	-	PRG
2003 Apr 27	20:03-21:53	CA22	G-100	600	9	-	SAB
2003 Apr 28	21:15-22:08	INT	R632V	600	6	-	PRG
2003 May 10	20:20-21:21	CA22	G-100	600	6	-	Service
2003 May 11	20:17-21:20	CA22	G-100	600	6	-	Service
2003 Dec 25	00:56-05:35	CA22	G-100	600	24	-	AA
2003 Dec 26	04:20-06:14	CA22	Clear	20-30	149	C5	AA
2003 Dec 27	02:50-03:01	CA22	G-100	600	2	-	AA
2003 Dec 30	19:58-21:06	TO	Clear	120	46	C5	HL
2004 Jan 01	18:37-23:27	TO	Clear	60	250	C5	HL
2004 Oct 22	04:01-05:25	CA22	Clear	15	59	C5	AA
2004 Oct 24	02:12-05:26	CA22	G-100	600	17	-	AA

Continued on next page

Date	UT	Telescope[a]	Filter/ Grism	Exp. (s)	Frames	Comp.[b] star	Observer[c]
2004 Oct 25	01:42-05:51	CA22	Clear	10-15	463	C5	AA
2004 Oct 26	04:25-05:31	CA22	G-100	600	7	-	AA
2004 Dec 02	04:01-05:00	IAC80	Clear	10	150	C5	AA
2004 Dec 07	05:10-06:11	IAC80	Clear	15	139	C5	AA
2004 Dec 08	01:00-04:41	IAC80	Clear	10	528	C5	AA
2004 Dec 09	00:13-05:14	IAC80	Clear	10	738	C5	AA
HS 1016+3412							
1991 Mar 19	22:14	CA08	Prism	3600	1	-	
1996 Apr 04	20:24	CA08	Prism	3600	1	-	
2001 Apr 30	21:35	CA22	B-200	600	1	-	
2003 Apr 07	21:54	CA22	G-100	600	1	-	BG
2003 Apr 08	21:09-22:19	CA22	G-100	600	7	-	BG
2003 Apr 10	22:28	CA22	G-100	600	1	-	BG
2003 Apr 12	22:28-00:10	CA22	G-100	600	9	-	BG
2003 Apr 24	22:07-23:01	INT	R632V	600	6	-	PRG
2003 Apr 25	23:31-00:24	INT	R632V	600	6	-	PRG
2003 Apr 27	22:27-23:28	CA22	G-100	600	6	-	SAB
2003 Apr 28	22:31-23:24	INT	R632V	600	6	-	PRG
2003 May 18	22:08-22:51	INT	R632V	600	6	-	PRG
2004 May 23	19:52-21:59	KY	Clear	45-90	104	C6	SK
2004 May 24	20:09-21:47	KY	Clear	60	55	C6	SK
2004 May 26	19:51-22:20	KY	Clear	45	157	C6	SK
2004 May 27	19:58-23:10	KY	Clear	60-75	116	C6	SK
2004 May 28	20:12-22:48	KY	Clear	60	101	C6	SK
2004 May 29	22:52-23:57	IAC80	Clear	125	29	C6	AA

Continued on next page

Date	UT	Telescope[a]	Filter/ Grism	Exp. (s)	Frames	Comp.[b] star	Observer[c]
2004 May 30	22:55-23:58	IAC80	Clear	120	28	C6	AA
2004 May 31	21:18-22:48	IAC80	Clear	113	45	C6	AA
2005 Feb 12	23:34-05:24	CA22	G-100	600	24	-	Service
HS 1340+1524							
1994 May 05		CA08	Prism	3600	1	-	
1996 Apr 18		CA08	Prism	3600	1	-	
2001 May 01	02:14	CA22	B-200	600	1	-	BG
2001 May 08	20:17-02:00	AIP	*R*	120	200	C9	RS
2001 May 09	20:51-00:23	AIP	*R*	120	83	C9	RS
2002 Jul 02	18:57-22:42	KY	*R*	120	86	C7	SK
2002 Jul 04	20:02-22:17	KY	*R*	120	58	C7	SK
2003 Apr 07	22:37-23:29	CA22	G-100	600	5	-	BG
2003 Apr 08	22:42-23:41	CA22	G-100	600	6	-	BG
2003 Apr 09	23:48-00:10	CA22	G-100	600	3	-	BG
2003 Apr 10	22:46-00:29	CA22	G-100	600	7	-	BG
2003 Apr 11	00:39-04:52	CA22	*V*	30	179	C7	BG
2003 Apr 11	21:45-01:35	CA22	G-100	600	11	-	BG
2003 Apr 13	00:31-03:28	CA22	G-100	600	12	-	BG
2003 Apr 24	00:26-01:19	INT	R632V	600	6	-	PRG
2003 Apr 25	00:34-01:26	INT	R632V	600	6	-	PRG
2003 Apr 28	22:54-00:32	CA22	G-100	600	7	-	SAB
2003 May 29	19:44-22:03	KY	*R*	90	69	C7	DM
2003 May 30	19:17-01:12	KY	*R*	90	212	C7	DM
2003 Jun 24	19:28-22:08	KY	*R*	90	101	C7	OG
2003 Jun 28	19:21-22:10	KY	*R*	120	76	C7	OG

Continued on next page

Date	UT	Telescope[a]	Filter/ Grism	Exp. (s)	Frames	Comp.[b] star	Observer[c]
2004 Mar 17	07:18-11:38	FLWO	Clear	40	297	C8	PRG
2004 Mar 18	07:23-12:00	FLWO	Clear	40	273	C8	PRG
2004 May 19	23:14-03:01	IAC80	Clear	60	193	C9	AA
2004 May 20	22:43-00:58	IAC80	Clear	90	78	C9	AA
2004 May 22	21:39-00:34	KY	Clear	30	262	C7	SK
2004 Jun 10	20:01-21:54	KY	Clear	30	176	C7	SK
2005 Feb 18	01:13-05:10	CA22	G-100	600	15	-	Service
2005 May 11	23:10-03:04	IAC80	Clear	45-60	203	C9	AA
2005 May 12	22:41-04:20	IAC80	Clear	60	213	C9	AA
2005 May 13	22:07-04:09	IAC80	Clear	60	270	C9	AA
HS 1857+5144							
1987 Jul 30	23:03	CA08	Prism	3600	1	-	
1992 Aug 10	21:51	CA22		1500	1	-	
2003 Jul 10	21:03-01:01	OGS	Clear	17	610	C10	PRG
2003 Jul 13	21:16-01:00	OGS	Clear	12	751	C10	PRG
2003 Jul 21	19:15-02:25	KY	Clear	30	671	C10	CP
2003 Jul 23	18:56-02:32	KY	Clear	20-45	311	C10	CP
2004 May 21	01:43-05:25	IAC80	Clear	40	231	C11	AA
2004 May 23	00:52-02:07	KY	Clear	20-30	199	C10	SK
2004 May 25	21:34-02:26	KY	Clear	20	587	C10	SK
2004 May 26	23:14-02:29	KY	Clear	20	335	C10	SK
2004 May 27	02:51-05:12	IAC80	Clear	40	286	C11	AA
2004 Jun 09	21:40-02:20	KY	Clear	20	608	C10	SK
2004 Jul 16	04:13-11:01	McD	#43	600	31	-	CAP
2004 Jul 19	04:25-08:58	McD	#43	600	4	-	CAP

Continued on next page

Date	UT	Telescope[a]	Filter/ Grism	Exp. (s)	Frames	Comp.[b] star	Observer[c]
2006 May 28	21:21-02:14	KY	*R*	70-80	212	C10	AA & OG
2006 May 29	19:53-02:21	KY	*R*	80	267	C10	AA
2006 May 30	20:58-02:21	KY	*R*	80	186	C10	AA
2006 Jun 04	20:15-02:14	KY	*B*	90-110	196	C10	AA
2006 Jul 02	21:17	WHT	R1200B/R600R	600	1	-	BG
2006 Jul 03	21:21	WHT	R1200B/R600R	600	1	-	BG
2006 Jul 04	21:17	WHT	R1200B/R600R	600	1	-	BG
2006 Jul 05	21:16	WHT	R1200B/R600R	600	1	-	BG
HS 1857+7127							
1990 Jul 31	02:32	CA22	120 Å/mm	3600	1	-	
2002 Apr 03	23:30-03:29	AIP	*R*	120	118	C14	RS
2002 Apr 22	19:52-02:38	AIP	*R*	120	185	C14	RS
2002 Sep 16	18:16-23:44	KY	*R*	5	1700	C13	SK
2002 Sep 17	18:31-21:50	KY	*R*	5-10	683	C13	SK
2002 Oct 24	18:05-04:27	AIP	*R*	60	447	C14	RS
2003 Apr 08	02:44-03:44	CA22	G-100	600	6	-	BG
2003 Apr 09	02:10-04:47	CA22	G-100	600	10	-	BG
2003 Apr 13	02:25-04:50	CA22	G-100	600	9	-	BG
2003 Apr 22	19:45-03:04	AIP	*R*	60	386	C14	RS
2003 Apr 25	04:01-05:03	INT	R632V	600	7	-	PRG
2003 Apr 27	05:32-05:43	INT	R632V	600	2	-	PRG
2003 Apr 29	04:18-04:30	CA22	G-100	600	2	-	SAB
2003 Apr 29	04:46-05:28	INT	R632V	600	5	-	PRG
2003 Jul 08	03:18-05:19	OGS	Clear	20	279	C12	PRG
2003 Aug 17	03:28	HST/STIS	G140L	800	1	-	BG

Continued on next page

Date	UT	Telescope[a]	Filter/ Grism	Exp. (s)	Frames	Comp.[b] star	Observer[c]
2003 Aug 17	22:42-23:08	KY	*V*	8	147	C13	BG
2004 May 03	00:21-05:46	IAC80	Clear	15	922	C12	PRG
2004 May 03	06:11-07:53	FLWO	Clear	10	487	C12	MT
2004 May 04	08:25-11:15	FLWO	Clear	10	809	C12	MT
HS 2214+2845							
1987 Aug 25	23:48	CA08	Prism	3600	1	-	
2000 Sep 20	21:26	CA22	B-200	600	1	-	BG
2000 Sep 21	03:28-11:04	BS	*R*	100	245	:	RF
2000 Sep 24	02:44-10:53	BS	*R*	100	254	:	RF
2000 Sep 24	20:10-23:55	CA22	B-100	600	16	-	BG
2000 Sep 24	20:23-20:54	CA22	R-100	600	2	-	BG
2002 Aug 29	02:25-03:48	INT	R632V	600	9	-	SAB
2002 Sep 01	03:07-03:58	INT	R632V	600	6	-	SAB
2002 Sep 02	02:51-03:22	INT	R632V	600	4	-	SAB
2002 Sep 04	00:23-00:54	INT	R632V	600	4	-	SAB
2003 Jun 23	23:54-02:08	KY	*R*	90	85	C16	OG
2003 Jun 25	00:06-02:11	KY	*R*	90	80	C16	OG
2003 Jun 27	23:35-00:44	KY	*R*	30	113	C16	OG
2003 Jun 28	22:49-00:35	KY	*R*	60	93	C16	OG
2003 Jul 15	02:29-05:09	OGS	Clear	15	442	C15	PRG
2003 Sep 20	21:31-02:30	IAC80	Clear	10	871	C15	PRG
2003 Sep 21	19:53-02:52	IAC80	Clear	10	1187	C15	PRG
2003 Sep 22	20:14-03:10	IAC80	Clear	10	772	C15	PRG
2003 Sep 24	00:16-03:59	IAC80	Clear	10	689	C15	PRG

[a]AIP: 0.7 m telescope of the Astrophysikalisches Institut Potsda, BS: 0.41 m telescope at Braeside Observatory, CA08: 0.8 m Schmidt telescope at Calar Alto Observatory, CA22: 2.2 m telescope at Calar Alto Observatory, CA35: 3.5 m telescope at Calar Alto Observatory, FLWO: 1.2 m telescope at Fred Lawrence Whipple Observatory, HST/STIS: Hubble Space Telescope, IAC80: 0.82 m telescope at Observatorio del Teide, INT: 2.5 m Isaac Newton Telescope on Observatorio del Roque de los Muchachos, KY: 1.2 m telescope at Kryoneri Observatory, OGS: 1 m Optical Ground Station at Observatorio del Teide, OLT: 1.2 m Oskar Lühning Teleskop at Hamburg Observatory, TO: 0.7 m telescope at Tuorla Observatory, WD: 0.8 m telescope at Wendelstein Observatory

[b]The comparison stars used in instrumental magnitude extractions from Braeside are unknown (marked by colons).

[c]AA: Amornrat Aungwerojwit, BG: Boris Gänsicke, CAP: Carlos Allende Prieto, CP: Christos Papadimitriou, DE: Dieter Engels, DM: Dimitris Mislis, HB: Heinz Barwig, HJH: Hans-Jürgen Hagen, HL: Harry Lehto, MT: Manuel Torres, OG: Omiros Giannakis, PRG: Pablo Rodríguez-Gil, RF: Robert Fried, RS: Robert Schwarz, SAB: Sofía Araujo-Betancor, SK: Spyridon Kitsionas

Chapter 3

Time-series analysis methods for orbital period measurement

The primary aim of obtaining the time-resolved spectroscopy and photometry described in Chapter 2 is to measure orbital periods of the new HQS CVs/pre-CVs by means of determining periodic signals from their radial velocity variations and/or photometric variability using time-series analysis. Techniques of analysing variability and periodicities in time-series data can be divided into two general methods, broadly termed Fourier-type methods, and phase-folding methods. Phase-folding procedures are effective for variations that display abrupt changes, such as in light curves of eclipsing binaries. The Fourier-type methods are well-suited for more subtle signals.

Throughout this thesis, the orbital period determinations of the new HQS CVs/pre-CV were carried out using the utilities for time-series analysis within the `MIDAS/TSA` package, written by A. Schwarzenberg-Czerny, which provides some powerful tools to handle unevenly sampled data. More specifically, the `MIDAS/TSA` context provides two Fourier-type analyses and two analysis of variance (AOV) methods. In the following section, I briefly outline the method of Fourier analysis, which is a standard form of time-series analysis, and apply it to different synthetic data sets to illustrate the problems of aliasing in the resulting periodograms. In Section 3.2, I describe the different time-series analysis methods within `MIDAS/TSA` and compare the results obtained with each method for a small sample of the systems presented in Chapters 4–6.

3.1 Fourier analysis

Broadly speaking, time-series analysis methods that transform the time-series data from time-domain information, i.e. the change of an observable quantity as a function of time, into the frequency domain, are called Fourier analysis. In this process, the time variability is decomposed into an infinite number of sine waves with frequencies ranging from zero to infinity. The amplitude of each sine wave is determined by its relative contribution to the observed time-variable signal, and a plot of these amplitudes against frequency is called a power spectrum, or periodogram. In the simplest case of an infinitely long observation of a time-variable signal consisting of a pure sine wave, the power spectrum will contain a single peak in a form of a δ-function at the frequency of the variability. A more complex waveform with the same frequency will translate into a power spectrum with peaks at the fundamental frequency and its harmonics. Similarly, if a time-variable signal is the superposition of two or more signals with different frequencies, the power spectrum will resolve that variability into different peaks.

In the context of astronomy, two major points have to be taken into consideration. Firstly, the observations will be limited in duration, with the typical length being at best one night (except for observations carried out from different latitudes on Earth). The accuracy of which a periodicity can be determined then depends on the duration of the observation, or more specifically depends on the number of cycles covered by the data. In general, the shorter the data set, the less accurately can the period be determined. Figure 3.1 compares two periodograms for a syn-

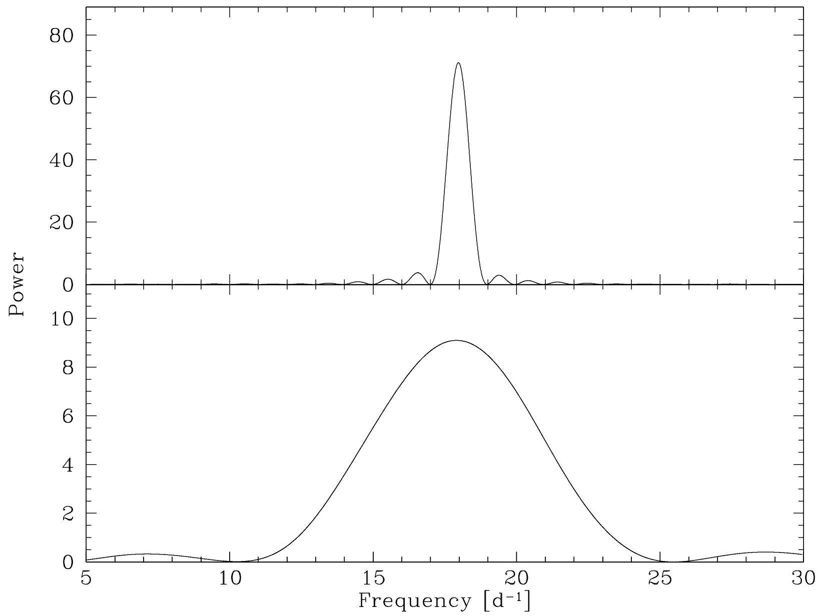

Figure 3.1: Periodograms of two different synthetic data sets of a sinusoidal variation with a period of 80 min. *Top panel*: The power spectrum resulting from a 24 h long observation. *Bottom panel*: The power spectrum from a 160 min long observation. It is apparent that the longer data set allows a more precise determination of the periodicity in the data.

thetic data set of a sinusoidal variation with a period of 80 min, spanning 24 h (top panel) and 160 min (bottom panel). It is clear that the longer data set produces a better frequency resolution, i.e. a narrower peak, and a stronger amplitude than that of the shorter one, allowing a more precise determination of the periodicity in the observations.

To achieve higher accuracy in the period determination, one commonly accumulates data over several nights, which leads to the second important phenomenon in Fourier analysis. In the case that the data contain gaps, the transform will suffer from alias structure, where several different peaks appear along with the “real” peak (e.g. Figure 3.2). These alias peaks are separated from the true frequency by integer multiples of the frequency of the observations, i.e. if observations are carried out every night, they will be split by 1 d^{-1}. If the true period is short compared to the frequency of the observations, and the data are obtained just with that regular sampling, the power spectrum will contain several alias peaks with equally statistical significance, even if large amounts of data are accumulated. This is also known as *cycle count ambiguity*, i.e. because of the long gaps between individual data sets, it is not possible to unambiguously determine how many orbital cycles have passed between one night and the next.

Figure 3.2 (top panel) displays the periodogram of three synthetic data sets "taken" over three consecutive nights in which each single observation spans two 80 min orbital cycles. Consequently, the aliases are exactly separated by $1\,\mathrm{d}^{-1}$. As the sampling frequency ($1\,\mathrm{d}^{-1}$) is much lower the orbital frequency ($18\,\mathrm{d}^{-1}$) and the data sets have a gap of 16 orbital cycles, the one-day aliases of the signal of the true frequency are very strong. The power of these $1\,\mathrm{d}^{-1}$ peaks can be diminished, if the data are obtained frequently with an uneven sampling, e.g. in Figure 3.2 (middle panel) which shows the periodogram of the same three "observations" as above, but with a 0.9 d and a 1.3 d separation. However, in practice, real data sets are subject to varying of observing conditions, and may have a wide degree of temporal coverage. The bottom panel in Figure 3.2 shows a worst-case scenario of an observation with large gaps between the individual data sets, and none of which covers the full orbital period of 80 min. Specifically, the data train consists of four short data sets of 1/2, 3/4, 1/3, and 1/2 orbital cycles, with three of them taken on consecutive nights, plus the fourth observation obtained three years later. In this case, the resulting periodogram displays a complex alias structure that prevents a secure determination of the actual orbital period.

3.2 `MIDAS` utilities for time series analysis

The significance of the detection of a periodic signal in the transformed data depends on the type of data and the method employed for the analysis. The `MIDAS/TSA` context offers four different methods, which are the two Fourier-type methods

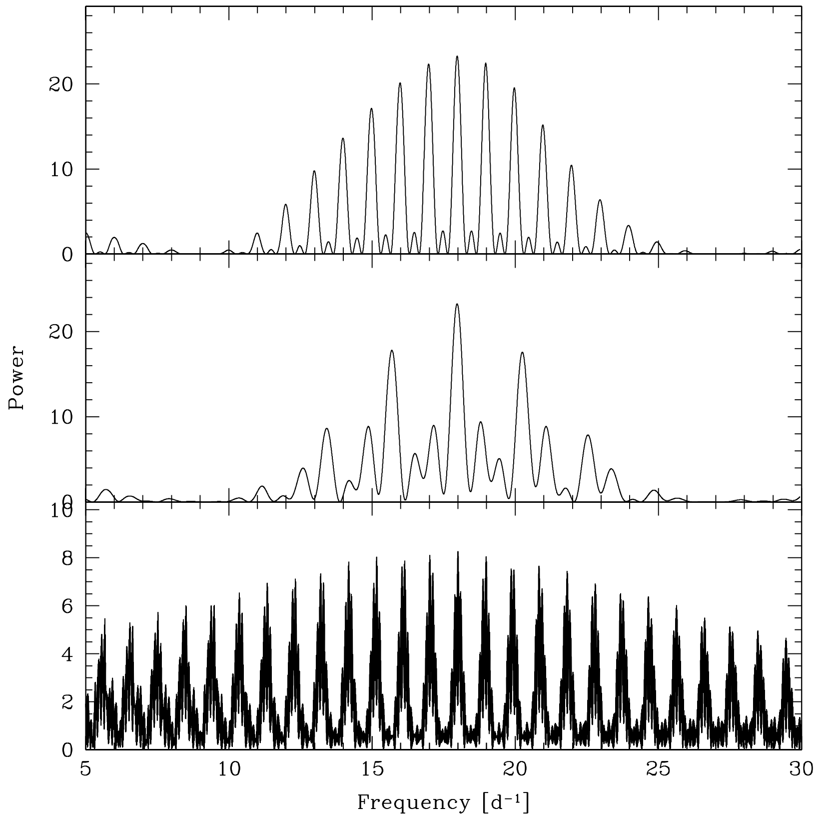

Figure 3.2: Periodograms of three different samples represent different alias structures. *Top panel*: one-day aliases produced by three data trains which cover two orbital cycles of 80 min each, "observed" over three consecutive nights. *Middle panel*: the reduced alias peaks result from the same data sets, but with a 0.9 d and a 1.3 d separation. *Bottom panel*: a complex alias pattern results from four different data sets in which each data set does not cover the orbital cycle and contains several gaps between the individual "observations".

(POWER/TSA and SCARGLE/TSA) and the two phase-folding/AOV methods (AOV/TSA and ORT/TSA).

- POWER/TSA computes a discrete Fourier transform from unevenly sampled data, and represents the most simple and straightforward method of time-series analysis.

- SCARGLE/TSA computes a periodogram for unevenly spaced observations following Scargle (1982) by fitting a pure sine model to the data. It is, hence, suitable for the evaluation of smooth, quasi-sinusoidal variations.

- AOV/TSA folds the data over a set of trial periods and computes the variance of the resulting phase-binned light curve, using the algorithm described by Schwarzenberg-Czerny (1989). The AOV statistic is a powerful method for the detection of non-sinusoidal signals with narrow sharp features, such as eclipses.

- ORT/TSA folds the data over a set of trial periods, and then fits a set of orthogonal multi-harmonic sine waves to the phase-folded data (Schwarzenberg-Czerny 1996). Similar to the AOV method, it is very well suited for highly non-sinusoidal variations, but results in a smoother power spectrum than produced by AOV.

In general, the relative power of these methods depends on the type of the signal. For the detection of smooth signals, e.g. sinusoidal wave, either Scargle, ORT or AOV is suitable. For the detection of sharp signals or strongly pulsed variations, such as eclipses or superhumps, either ORT or AOV is more efficient than Scargle. However, there is no universally best method for time-series analysis. A method that is good for one type of signals may be poor for another one.

Figures 3.3–3.6 illustrate the periodograms calculated from the different methods used for a sample of signal patterns presented in Chapters 4–6. Figure 3.3 (top panel) shows the large-amplitude smooth sinusoidal light curve of a pre-CV, HS 1857+5144, which results from a strong reflection effect of the low-mass companion irradiated by the hot white dwarf (see Chapter 6 for details). In this case, the orbital period is clearly determined by all methods. The strong peaks at the low frequencies of the ORT periodogram result from sub-harmonics of the orbital period which are artifacts typical of this method. In other cases, however, the AOV and the ORT methods are less efficient in detecting low-amplitude sinusoidal signals, e.g. in Figure 3.4 which depicts the resulting periodogram of the Hα radial velocity variations of the novalike variable HS 0506+7725 (Chapter 4). The strength of AOV and ORT in the case of non-sinusoidal variations is demonstrated in Figure 3.5 and Figure 3.6, where the superhump and the double-humped pattern in the light curves of HS 0417+7445 during superoutburst and in the light curve of HS 2214+2845 during quiescence, respectively, are analysed. In the case of HS 0417+7445, the Scargle periodogram provides the superhump period with a large uncertainty compare to that of the ORT method (see Chapter 5 for details). For HS 2214+2845, the orbital period was defined on the basis of the appearance of the commensurate fundamental frequency and its harmonic, as found in the periodogram calculated using the AOV method (see Chapter 5 for details). In this case, the power in the Scargle periodogram goes into nearly equally strong one-day aliases.

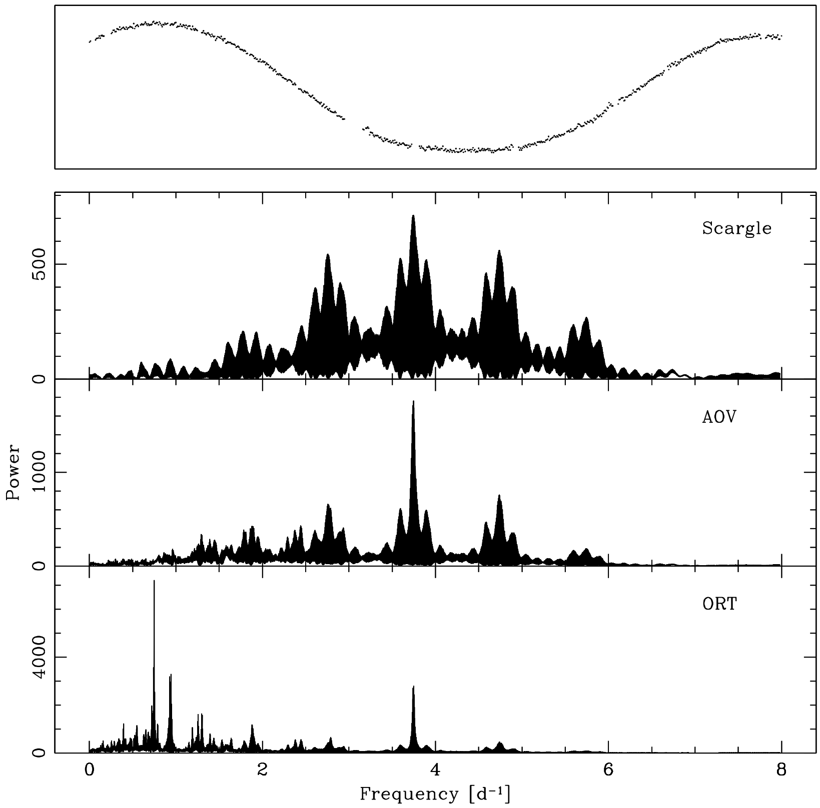

Figure 3.3: Scargle, `AOV`, and `ORT` periodograms (*bottom three panels*) computed from the smooth variablity in the light curves of HS 1857+5144. In this case, all periodograms contain a strong signal at the same frequency. A sample light curve is shown in *Top panel*. The strong peaks at low frequency in the `ORT` periodogram result from sub-harmonics of the orbital frequency.

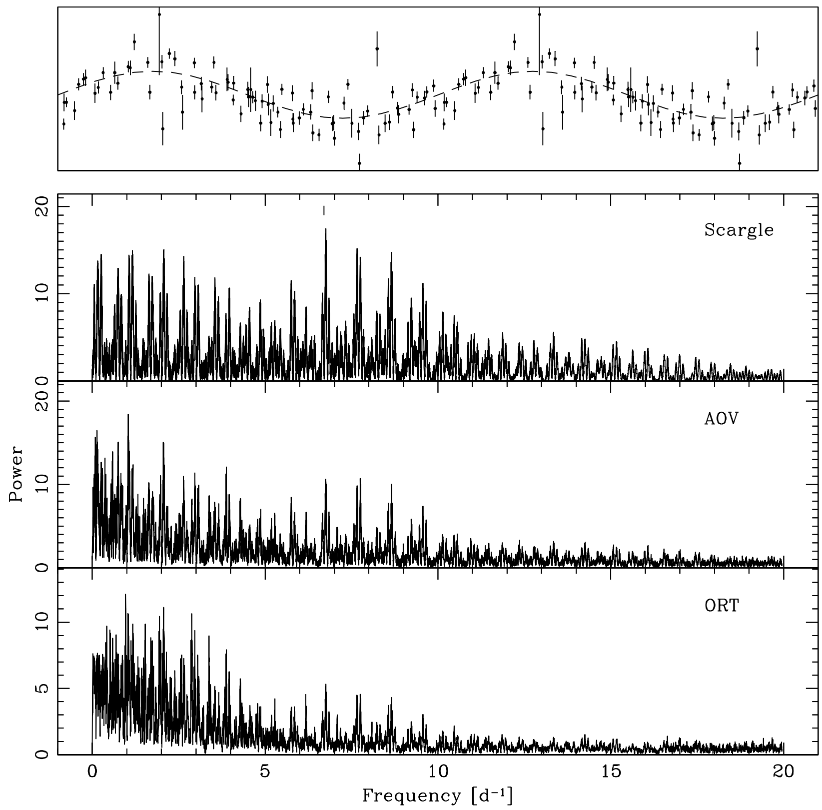

Figure 3.4: Scargle, AOV and ORT periodograms (*bottom three panels*) of the Hα radial velocity variations of HS 0506+7725 (*top panel*). The AOV and ORT methods show less sensitivity in detecting the correct orbital frequency (a tick mark in the Scargle periodogram).

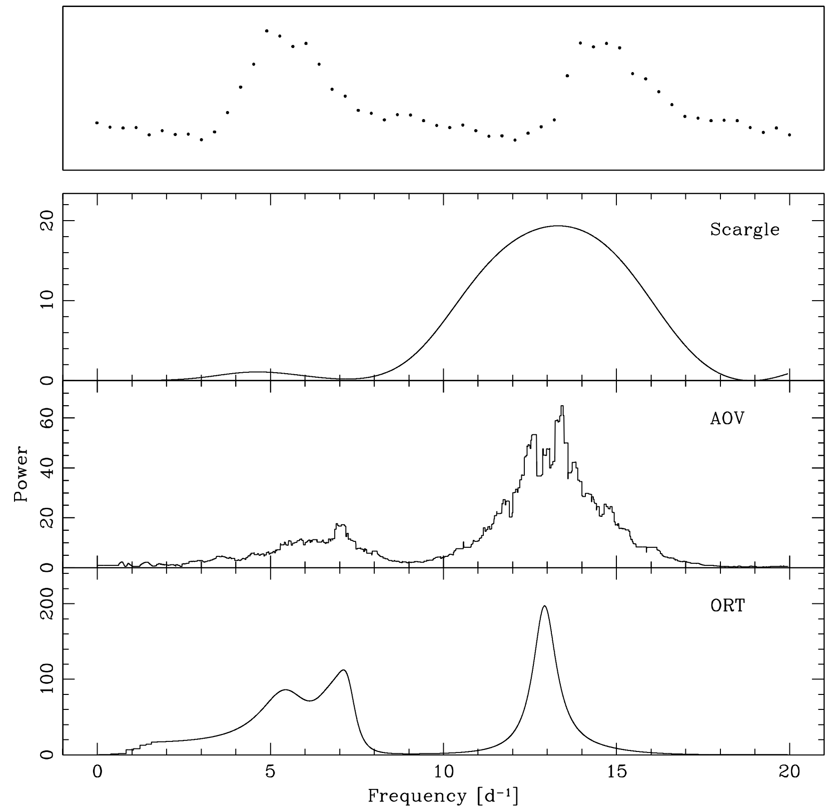

Figure 3.5: Scargle, AOV and ORT periodograms (*bottom three panels*) of the superhump structure found in the light curve of HS 0417+7445 during superoutburst (*top panel*). The ORT periodogram provides a much narrower signal than the Scargle method, as it can draw on the information from the non-sinusoidal variation.

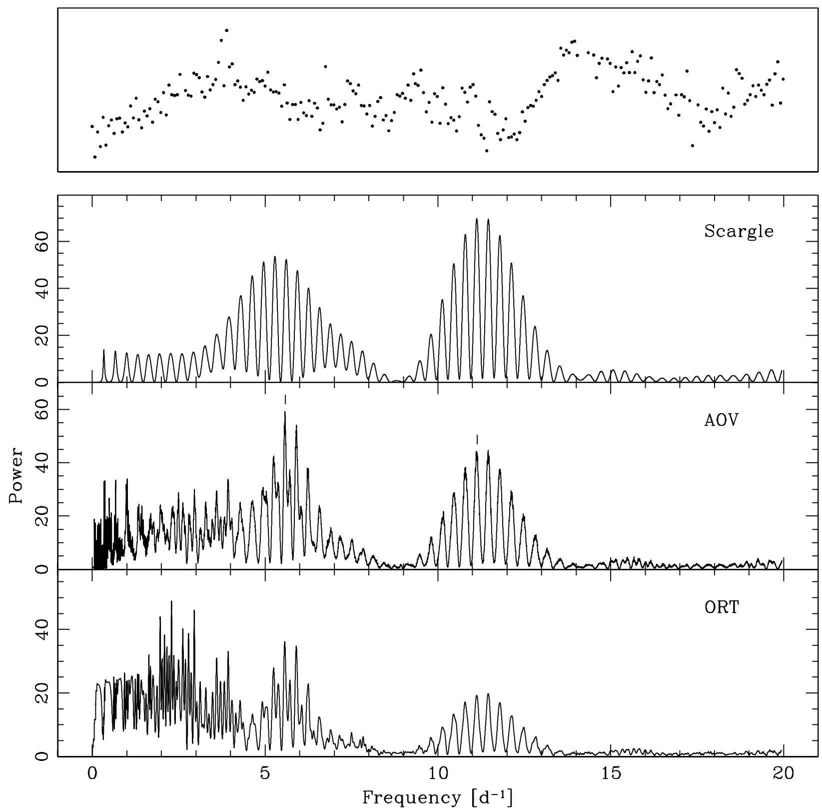

Figure 3.6: Scargle, AOV, and ORT periodograms (*bottom three panels*) computed from the double-humped signal found in the quiescent light curves of the dwarf nova HS 2214+2845. In this case, the correct orbital period is determined from the AOV method based on the detection of the commensurate fundamental frequency and its harmonic (tick marks).

Chapter 4

Four new long-period cataclysmic variables

4.1 Introduction

According to the disc instability model (e.g. Cannizzo et al. 1986; Osaki 1996), dwarf nova outbursts occur when the accretion rate is below a critical value, $\dot{M}_{\rm crit}$. For the systems having a mass-transfer rate above $\dot{M}_{\rm crit}$, accretion takes place in a stable condition and quasi-periodic outbursts do not occur. Such systems appear as novalike variables, or non-eruptive CVs. CVs above the conventional 2–3 h period gap, which have high mass-transfer rates driven by magnetic braking, are therefore mostly novalike variables and a fair fraction of Z Cam-type dwarf novae which are poised on the borderline between dwarf novae and novalike variables. Novalike variables are divided into the following distinct subclasses based on their spectroscopic and photometric properties: UX UMa type, VY Scl stars, and SW Sex stars (see Section 1.3 for details on the classification scheme).

As part of the large scale search for new CVs/pre-CVs in the HQS, I here present the identification of four new long-period CVs from this survey which are HS 0139+0559, HS 0229+8016, HS 0506+7725, and HS 0642+5049, with periods close to 4 h. Despite having similar orbital periods, these systems differ dramatically in their observed characteristics. The details on observations and data reduction for these new CVs are given in Chapter 2. The characteristics of these new CVs and their orbital period measurements are described in Sections 4.2–4.5. In Section 4.6, I discuss in detail the properties of the HQS and the previously known CVs in the 3–4 h period range.

4.2 HS 0139+0559

4.2.1 Spectroscopic characteristics

An identification spectrum of HS 0139+0559 obtained in January 1989, at the Calar Alto 3.5 m telescope (Figure 4.1) is characterised by a blue continuum with strong absorption lines of the Balmer series, as well as that of He I λ4471. The absorption profiles have a rectangular shape with a full width at zero intensity (FWZI) of $\sim 3500\,\mathrm{km\,s^{-1}}$. The cores of the broad Hβ and Hγ absorption lines show weak emission cores. No emission of He II λ4686 is observed. Overall, the identification spectrum of HS 0139+0559 resembles that of a high mass-transfer rate accretion disc seen at a moderately low inclination, e.g. a dwarf nova in outburst or a nova-like variable (e.g. Hessman et al. 1984; Morales-Rueda & Marsh 2002).

56 additional time-resolved spectra of HS 0139+0559 were obtained at the Calar Alto 3.5 m and 2.2 m telescopes during October 2002 and December 2003, respectively. These spectra are similar to the identification spectrum shown in Figure 4.1, with Hβ and Hγ in absorption for most of the time and occasionally showing signs of emission cores. However, the time-resolved spectra cover Hα as well, which is observed in emission throughout, with low equivalent widths in the range $3-5$ Å.

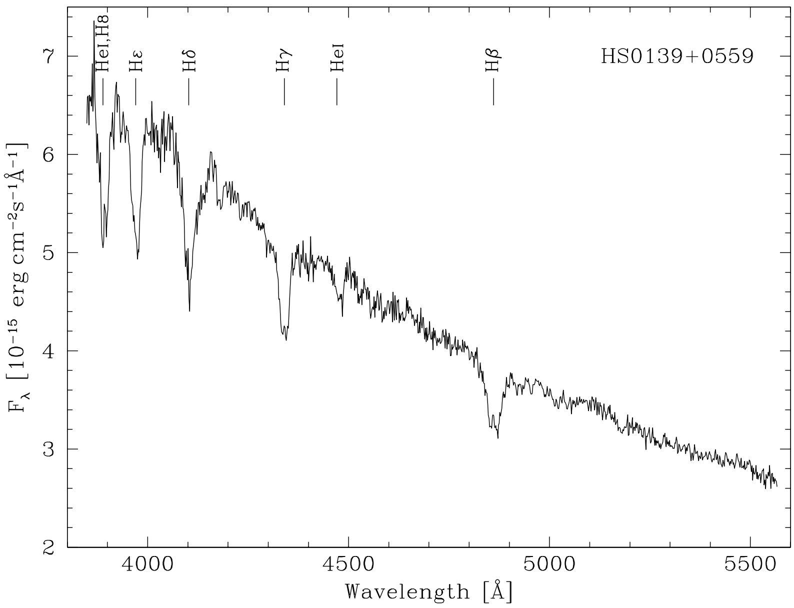

Figure 4.1: Identification spectrum of HS 0139+0559 obtained at the Calar Alto 3.5 m telescope on January 22, 1989.

4.2.2 Photometric characteristics

Differential *B*- and *R*-band photometry of HS 0139+0559 was obtained in December 1999 and January 2000 at Braeside observatory. The light curves display very little variability on nightly time scales, with amplitudes $\lesssim 0.02$ mag (Figure 4.2). There is no sign of orbital variation in the light curves. The USNO-A2.0 catalogue lists HS 0139+0559 with $B = R = 14.4$, and we found $B \simeq 14.9$ and $V \simeq 15.4$ during our observations in 1981 and 2003, respectively.

4.2.3 The orbital period

In order to determine the orbital period of HS 0139+0559, we measured the radial velocity variations of Hα by convolving the observed line profiles with a single Gaussian of FWHM=600 km s^{-1}. The spectra were continuum-normalised prior to this analysis. A Scargle (1982) period analysis of the radial velocity measurements was performed using the `MIDAS/TSA` context. The resulting periodogram

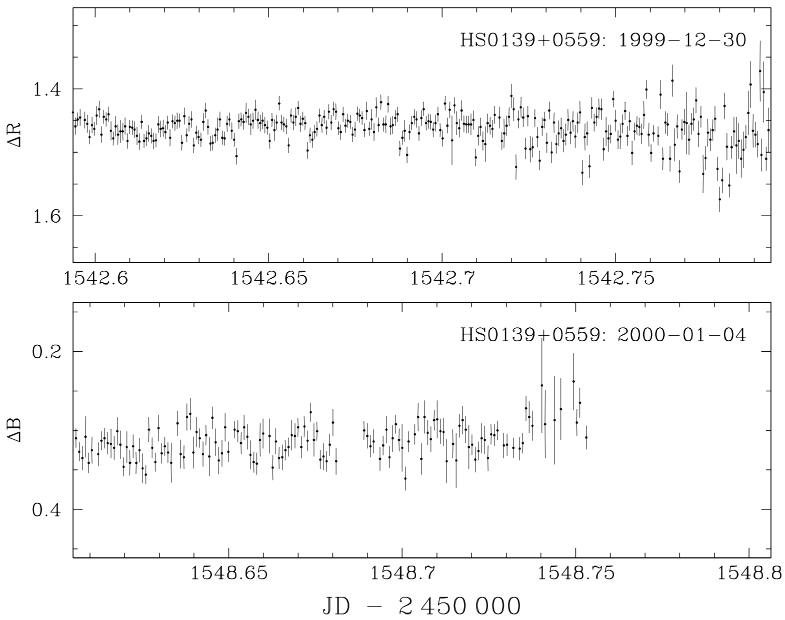

Figure 4.2: Differential CCD *R*-band *(top panel)* and *B*-band *(bottom panel)* photometry of HS 0139+0559 obtained at the Braeside observatory.

(Figure 4.3) shows a strong signal at $5.909 \pm 0.012\,\mathrm{d}^{-1}$ surrounded by one-day aliases, where the error is determined from fitting a sine wave to the radial velocity variation (see Table 4.1 for the full fit parameters). In order to test the significance of the detected signal, we created a set of faked radial velocities by evaluating a sine function with a frequency of $5.909\,\mathrm{d}^{-1}$ at the exact times of the observed spectroscopic data. The amplitude of the sine wave was adjusted to reflect the observed radial velocity amplitude, and the faked radial velocity measurements were randomly offset from the computed sine wave using the observed errors. The periodogram of the faked data reproduces the alias structure of the periodogram computed from the observations very well. We conclude that the orbital period of HS 0139+0559 is $P_{\mathrm{orb}} = 243.69 \pm 0.49\,\mathrm{min}$. Folding the radial velocity measurements over that period results in a quasi-sinusoidal radial velocity curve with an amplitude of $84.4 \pm 4.8\,\mathrm{km\,s^{-1}}$ (Figure 4.4, top panel).

For completeness, we also used the Braeside *B*- and *R*-band photometry for a period analysis. As suggested by the flat light curve (Figure 4.2), no significant

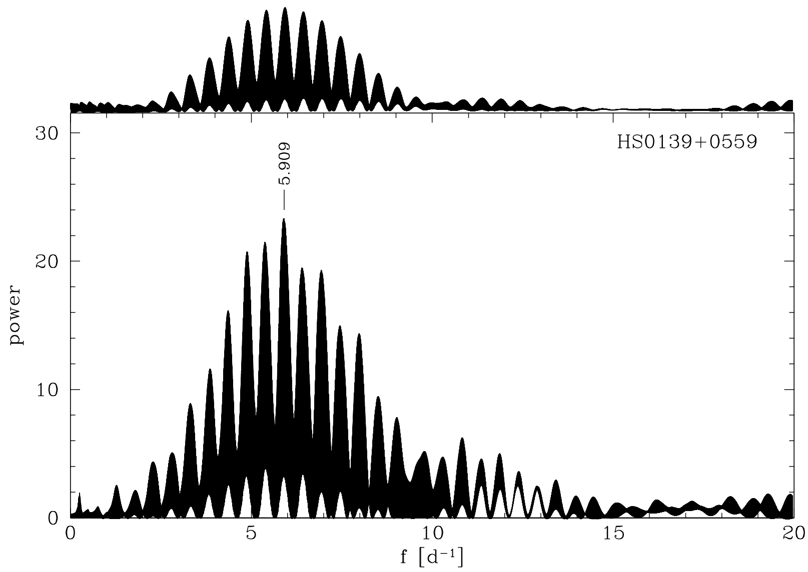

Figure 4.3: Scargle periodogram of the radial velocities of HS 0139+0559 measured from the radial velocity variations of Hα emission line. The periodogram from a set of faked radial velocities is shown in the *top panel*.

signal is detected in the Scargle periodogram.

4.3 HS 0229+8016

4.3.1 Spectroscopic characteristics

HS 0229+8016 was first spectroscopically observed at the Calar Alto 2.2 m telescope in August 1992. The spectrum (Figure 4.5, top panel) shows a blue continuum with the Balmer jump in emission, superimposed by moderately strong Balmer emission lines. The higher Balmer line profiles show evidence of a P-Cygni like structure with blue absorption wings increasing in strength for the higher members of the series. He I λ4471 is observed in absorption, and an emission line near 4630 Å is detected, which we tentatively identify as the N/C Bowen blend emission. Rather unusual is, however, the fact that He II λ4686 is not detected in emission along with the Bowen blend. HS 0229+8016 was observed again in October 1998,

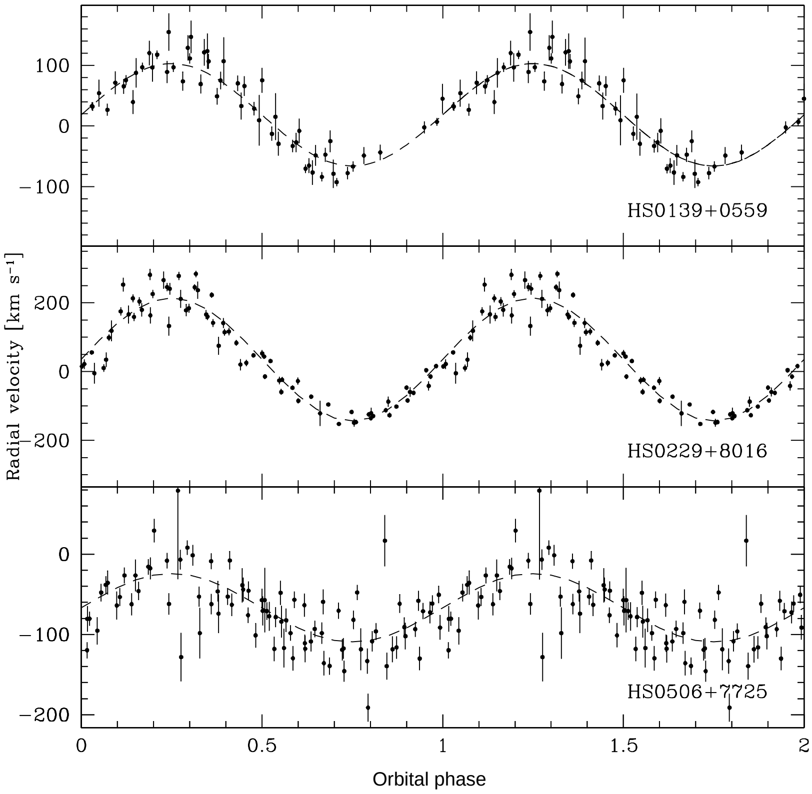

Figure 4.4: Hα radial velocities of HS 0139+0559 *(top panel)*, HS 0229+8016 *(middle panel)*, and HS 0506+7725 *(bottom panel)* folded over the orbital periods of 243.69 min, 232.550 min, and 212.7 min, respectively. The dashed lines are the best sine fits to the folded velocities.

on this occasion looking nearly identical to HS 0139+0559, showing a rectangular shape of the Balmer and He I absorption profiles (Figure 4.5, bottom panel). The spectral characteristics and the variability clearly identify HS 0229+8016 as a CV.

The time-resolved spectra of HS 0229+8016 (74 spectra) obtained with CAFOS in December 2003 are similar to the October 1998 spectrum shown in Figure 4.5 (bottom panel) in which Hβ, Hγ, and He I are present in broad absorption with weak emission cores. In addition, Hα emission is observed in the these spectra and shows a low equivalent width of ~ 5 Å.

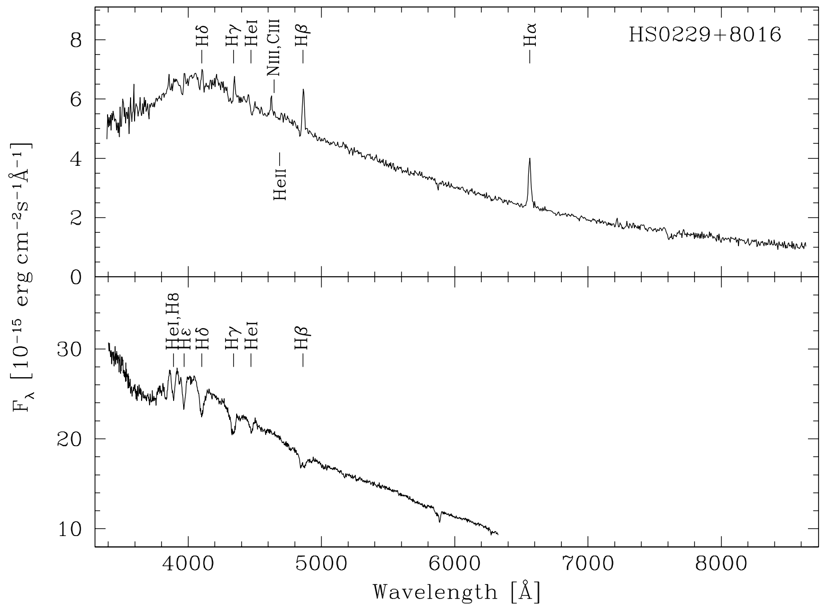

Figure 4.5: Identification spectra of HS 0229+8016 obtained at the Calar Alto 2.2 m telescope on August 8, 1992 *(top panel)* and October 5, 1998 *(bottom panel)*.

4.3.2 Photometric characteristics

We obtained differential CCD photometry of HS 0229+8016 during September 2002 and January 2003 using the Kryoneri and Tuorla telescopes, respectively. The light curves of HS 0229+8016 reveal a little variability on nightly time scales, with amplitudes ~ 0.1 mag (Figure 4.6). A low-amplitude modulation with a period of ~ 4 h is consistently detected during the two longest observations. HS 0229+8016 has $B = 13.9$ and $R = 13.8$ in the USNO-A2.0 catalogue, and it was found during our observations (1986–2003) mostly near $B \simeq V \simeq 14.6 - 14.0$, and $R \simeq 14.3$, except on one occasion (August 1992) when it was as faint as $V \simeq 15.0$.

4.3.3 The orbital period

An analogous radial velocity analysis as described in Section 4.2.3 was carried out for HS 0229+8016. Inspection of the Scargle periodogram (Figure 4.7) shows a somewhat more complex alias structure as a result of the inhomogeneous spac-

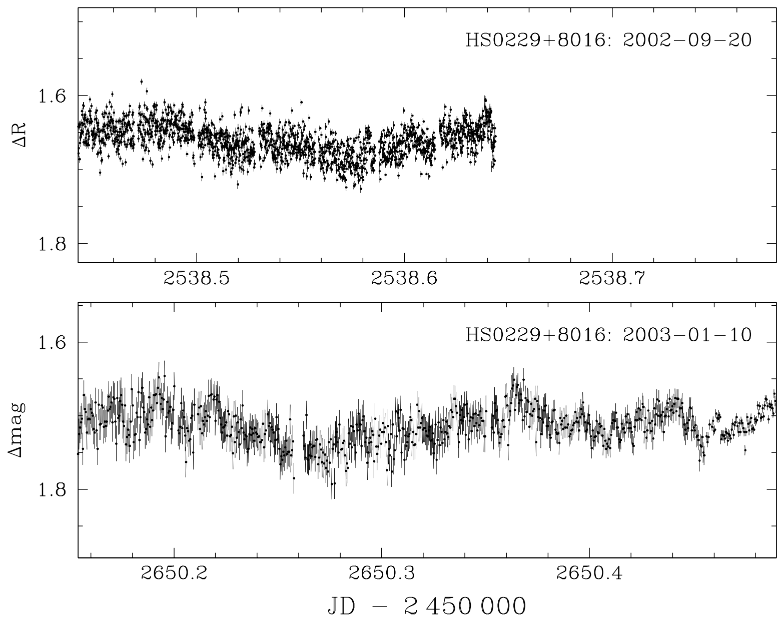

Figure 4.6: Sample light curves of HS 0229+8016. *Top panel*: *R*-band data obtained at the Kryoneri observatory. *Bottom panel*: filterless data obtained at the Tuorla observatory.

ing of the spectroscopic observations. The strongest signal is found at $6.1922 \pm 0.0013\,\mathrm{d}^{-1}$, where the error is again computed from a sine fit to the radial velocity data (Table 4.1), and a faked data set computed using this frequency reproduces the overall alias structure well. We conclude that the most likely value for the orbital period of HS 0229+0559 is $P_{\mathrm{orb}} = 232.550 \pm 0.049$ min. The phase-folded radial velocity curve shows a quasi-sinusoidal modulation with an amplitude of $179.0 \pm 5.2\,\mathrm{km\,s}^{-1}$ (Table 4.1).

Scargle periodograms computed from the two longest photometry runs on HS 0229+0559 are dominated by a broad signal near $5.2\,\mathrm{d}^{-1}$ (Kryoneri data) and $6.2\,\mathrm{d}^{-1}$ (Tuorla data), which are consistent with the spectroscopic period or its one-day alias. While our photometric data are not sufficient to improve the period determination of HS 0229+0559, it suggests that the orbital period of HS 0229+0559 can be refined by a sufficiently long series of photometric observations.

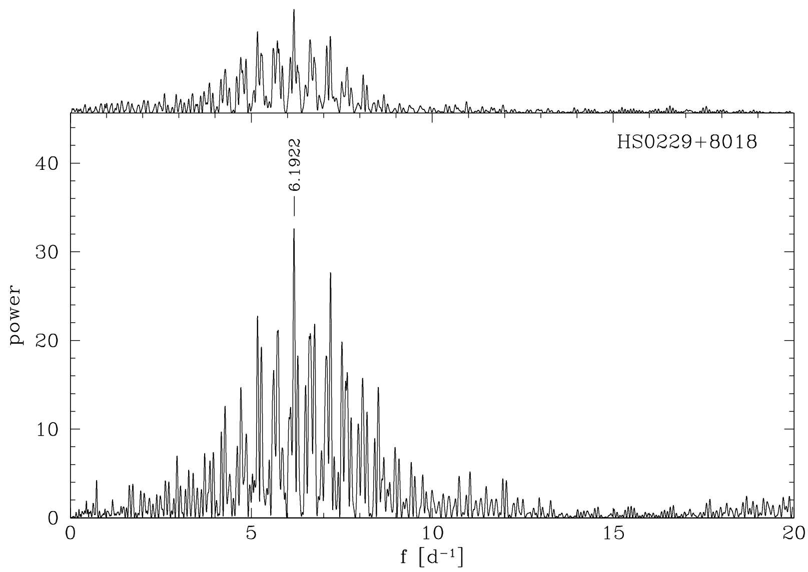

Figure 4.7: Scargle periodogram of the radial velocities of HS 0229+8016 measured from the Hα emission line. The periodogram from a set of faked radial velocities is shown in the *top panel*.

4.4 HS 0506+7725

4.4.1 Spectroscopic characteristics

An identification spectrum of HS 0506+7725 was obtained in February 1998, at the Calar Alto 2.2 m telescope. The spectrum (Figure 4.8, top panel) displays a blue continuum with the Balmer and Paschen jumps in emission, plus emission lines of hydrogen and He I. The $\lambda\lambda 4630-4650$ N/C Bowen blend and the He II $\lambda 4686$ emission lines are also detected. The strength of these high-ionisation lines is typical of novalike variables, magnetic CVs, or nova remnants.

Time-resolved spectroscopy of HS 0506+7725 was carried out using TWIN and CAFOS in December 2002/2003 obtaining 86 spectra in total. These spectra are characterised by prominent Balmer series and He I in emission, as previously found in the identification spectrum, with the difference of having a strong Balmer line decrement (see the CAFOS average spectrum in Figure 4.8, bottom panel). The

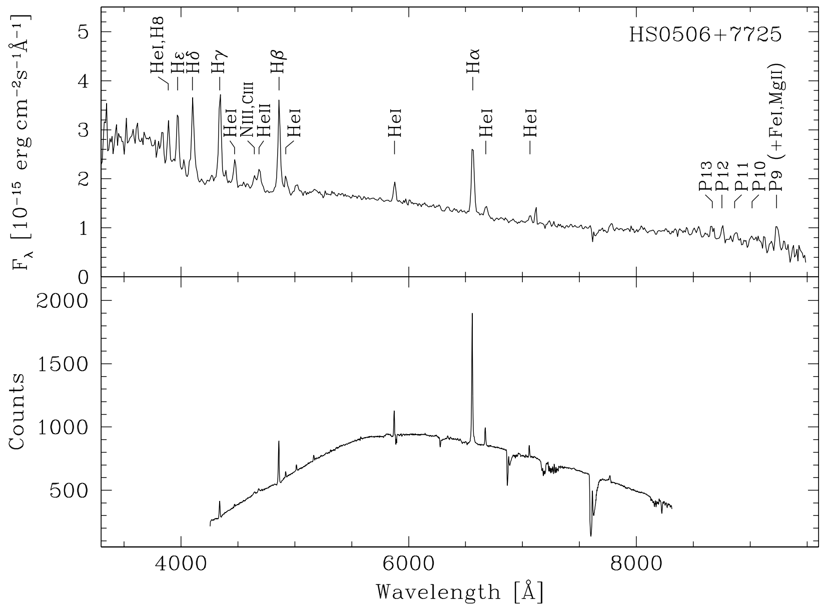

Figure 4.8: *Top panel*: flux-calibrated identification spectrum of HS 0506+7725 obtained at the Calar Alto 2.2 m telescope on February 2, 1998. The hydrogen lines display a flat Balmer decrement. *Bottom panel*: the average CAFOS time-resolved spectrum obtained during December 2003 observing run. No flux standard was obtained. During this observation, the spectrum of HS 0506+7725 differs markedly from the identification spectrum, with a strong Balmer decrement.

Hα emission line has an average equivalent width of ~ 15 Å. No sign of the N/C Bowen blend or the He II λ4686 emission was detected during these observations.

4.4.2 HS 0506+7725 as a VY Scl

Time-series differential CCD photometry of HS 0506+7725 was performed during 2002 and 2003 for a total of ~ 34 h using the Kryoneri 1.2 m, the Tuorla 0.7 m, the OGS 1 m, and the Calar Alto 2.2 m telescopes. The light curves exhibit short-term variability with an amplitude of $\sim 0.2-0.4$ mag, on time scales of $\sim 10-20$ min which appears to be quasi-periodic over brief amounts of time (Figure 4.9). No clearly repeating variation is detected on time scales of several hours (i.e. a putative orbital modulation).

HS 0506+7725 is listed with $B = 15.3$ and $R = 15.6$ in the USNO-A2.0 cat-

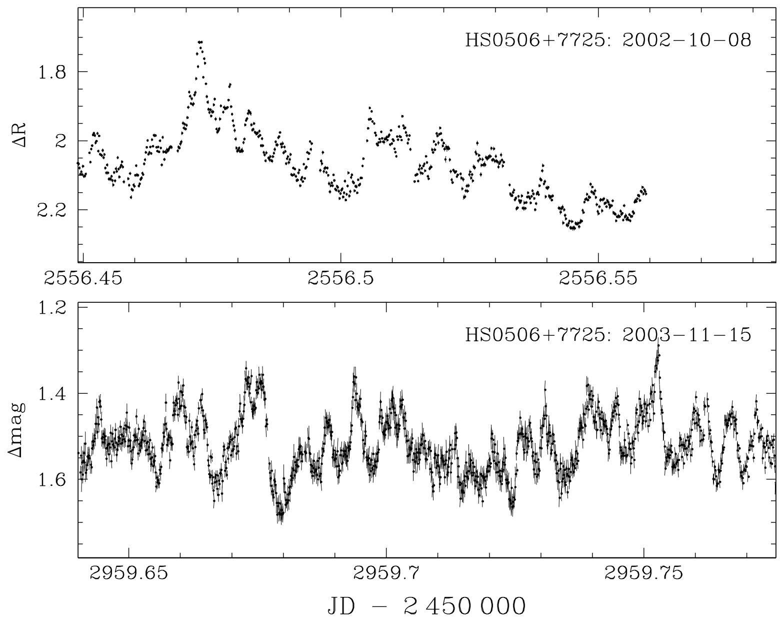

Figure 4.9: Sample light curves of HS 0506+7725. *Top panel*: *R*-band data obtained at the Kryoneri observatory. *Bottom panel*: filterless data obtained at the OGS telescope.

alogue, and we obtained $B \simeq 15.1/15.3$ (January 1987/1994), $R \simeq 15.2$ (October 2002), and $V \simeq 15.4$ (December 2002). In addition, our data provide evidence of long-term variability of ~ 1 mag. During 2003, the mean magnitude was $\simeq 15.8$, 14.6, and 14.8 in January, November, and December, respectively. However, a deep low state of HS 0506+7725 was detected at $B \simeq 18.3$ on a HQS photographic plate taken in October 1995, on the basis of which we identify HS 0506+7725 as a member of the VY Scl novalike variable.

4.4.3 The orbital period

Our initial analysis of the HS 0506+7725 Hα radial velocity variations was carried out by applying a single-Gaussian convolution to the continuum-normalised line profiles. However, the Scargle periodogram computed from the measured radial velocity variations turned out to be dominated by a variety of signals in the range $\sim 1 - 5\,\mathrm{d}^{-1}$, none of which resulted in a plausible phase-folded radial ve-

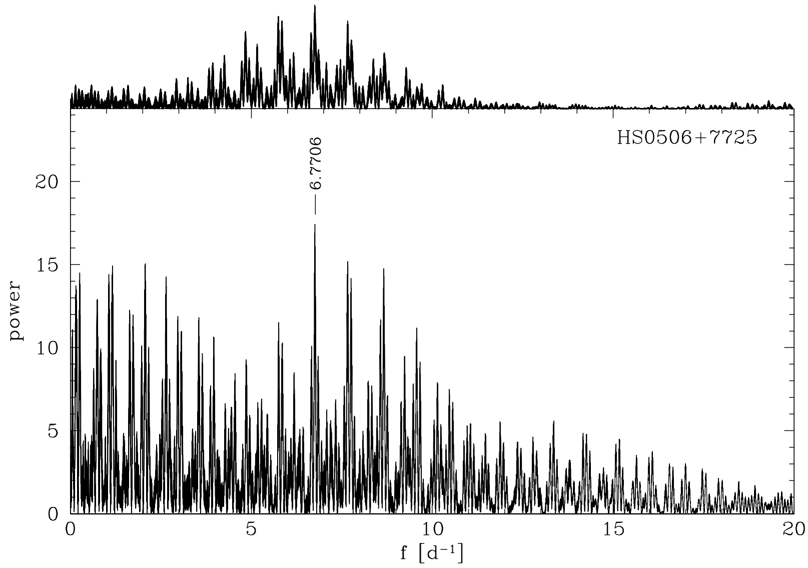

Figure 4.10: Scargle periodogram of the radial velocities of HS 0506+7725 measured from the Hα emission line by using the double-Gaussian method. The periodogram from a set of faked radial velocities is shown in the *top panel*.

locity curve. In a second attempt, we applied the double-Gaussian method of Schneider & Young (1980), using a Gaussian FWHM=700 $\mathrm{km\,s^{-1}}$ and a separation of 1500 $\mathrm{km\,s^{-1}}$ to measure the radial velocity variation of the line wings. The Scargle periodogram resulting from these radial velocity measurements includes several peaks in the range $5-9\,\mathrm{d^{-1}}$ (Figure 4.10). The strongest signal is found at $6.7706 \pm 0.0065\,\mathrm{d^{-1}}$, which we identify as the likely orbital period of HS 0506+7725, $P_{\mathrm{orb}} \simeq 212.7 \pm 0.2$ min, where the error is determined from a sine fit to the radial velocity data (Table 4.1). The Scargle periodogram computed from a faked data set results in a much cleaner periodogram than the one obtained from the observed data, suggesting that the line wings are affected by additional velocity contributions apart from the orbital motion. The Hα radial velocities folded over the orbital period (Figure 4.4) display a low amplitude of $42.6 \pm 4.4\,\mathrm{km\,s^{-1}}$ and a relatively large amount of scatter, again suggesting that the orbital motion measured from the line wings is contaminated by another velocity component.

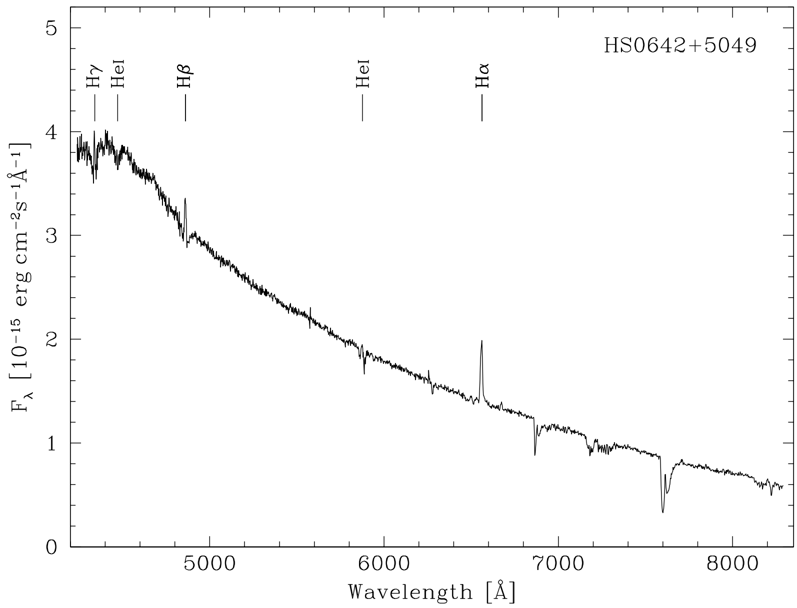

Figure 4.11: Average of the 17 CAFOS G-100 spectra of HS 0642+5049 obtained at the Calar Alto 2.2 m telescope on October 24, 2004.

Our time-series analysis of the photometry of HS 0506+7725 did not lead to the detection of any significant signal, either at long (orbital) or at short (putative white dwarf spin) frequencies, making the observed short-term variability (Figure 4.9) a nice example of non-coherent CV flickering.

4.5 HS 0642+5049

4.5.1 Spectroscopic characteristics

HS 0642+5049 was spectroscopically identified as a CV in March 1999, at the Calar Alto 2.2 m telescope. The identification spectrum contains a blue continuum with moderately strong Hα emission. The Hβ and Hγ emission is embedded in broad absorption troughs, and weak He I λ4471 absorption is also detected. Neither He II λ4686 nor the λλ4630 – 4650 N/C Bowen blend are detected.

87 time-resolved spectra of HS 0642+5049 were obtained using CAFOS and

IDS throughout the period April 2003 to October 2004. These spectra are very similar to the identification spectrum. Figure 4.11 displays the flux-calibrated average spectrum of HS 0642+5049 from the October 2004 observing run, showing Hα in emission with an average equivalent width of ~ 5 Å, along with weak emission cores of Hβ and Hγ embedded in board absorption lines.

4.5.2 Photometric characteristics

Time-resolved photometry of HS 0642+5049 was obtained in December 2003 to December 2004 at the Tuorla 0.7 m telescope, the Calar Alto 2.2 m telescope, and the IAC80 telescope. The Tuorla light curve displays brightness variation of ~ 0.25 mag in the longest run (January 1, 2004), suggesting an orbital modulation with a large scatter due to the poor quality of the data. A prominent orbital modulation is found in the CAFOS (October 25, 2004) and the IAC80 (December 8 & 9, 2004) light curves. Figure 4.12 shows the IAC80 light curves with a modulation of ~ 0.22 mag for a period of ~ 3.5 h, which we interpret as the orbital period of the system. No substantial flickering activity is detected. HS 0642+5049 is found in the USNO-A2.0 catalogue with $B = 16.6$ and $R = 16.9$, and we found $V \simeq 15.5 - 15.3$ without significant long-term variability of the system.

4.5.3 The orbital period

The 87 available spectra of HS 0642+5049 were subjected to radial velocity studies as outlined above, using both the single-Gaussian and double-Gaussian convolution techniques. None of the resulting Scargle periodograms contained any significant signal. Inspecting trailed spectra assembled from our data, we concluded that HS 0642+5049 does not show any radial velocity variation at our spectral resolution.

Considering the ~ 3.5 h modulation observed in the HS 0642+5049 light

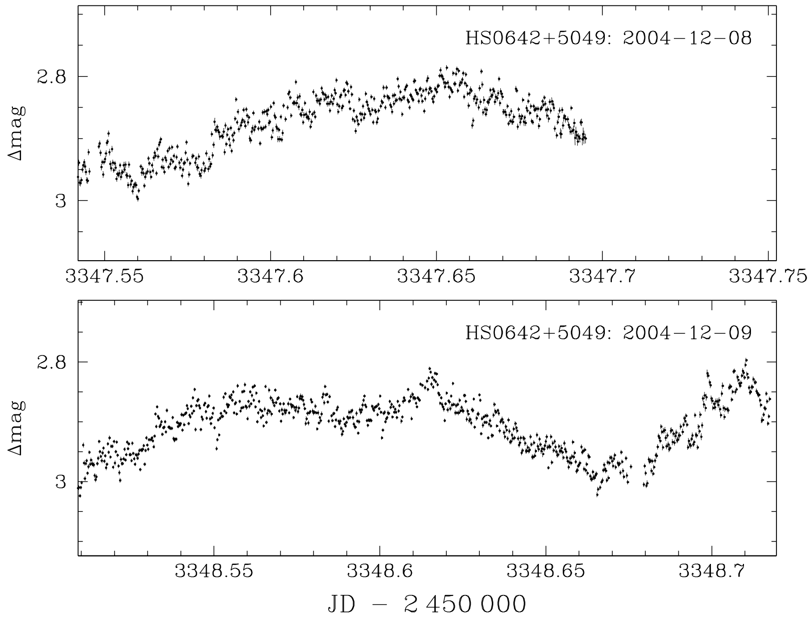

Figure 4.12: Sample filterless light curves of HS 0642+5049 obtained at the IAC80 telescope.

curves, we used the three longest and closest spaced photometric data sets obtained at the Calar Alto 2.2 m telescope (October 25, 2004) and the IAC80 (December 8 & 9, 2004) to determine the orbital period of the system. The strongest peak detected in the Scargle periodogram computed from these data is found at $6.3746 \pm 0.0065\,\mathrm{d}^{-1}$, surrounded by one-day aliases (Figure 4.13). In order to test the significance of the signal, we created a set of faked data from a sine wave with a frequency of $6.3746\mathrm{d}^{-1}$, evaluated at the exact times of the observations. The alias structures of the periodograms calculated from the faked data and the real data agree well. We conclude that the orbital period of HS 0642+5049 is $P_{\mathrm{orb}} \simeq 225.90 \pm 0.23\,\mathrm{min}$.

Figure 4.14 shows the Calar Alto 2.2 m and the IAC80 photometry folded over the orbital period of 225.90 min and averaged into 30 phase bins, which reflects the morphology of the individual light curves (e.g. Figure 4.12).

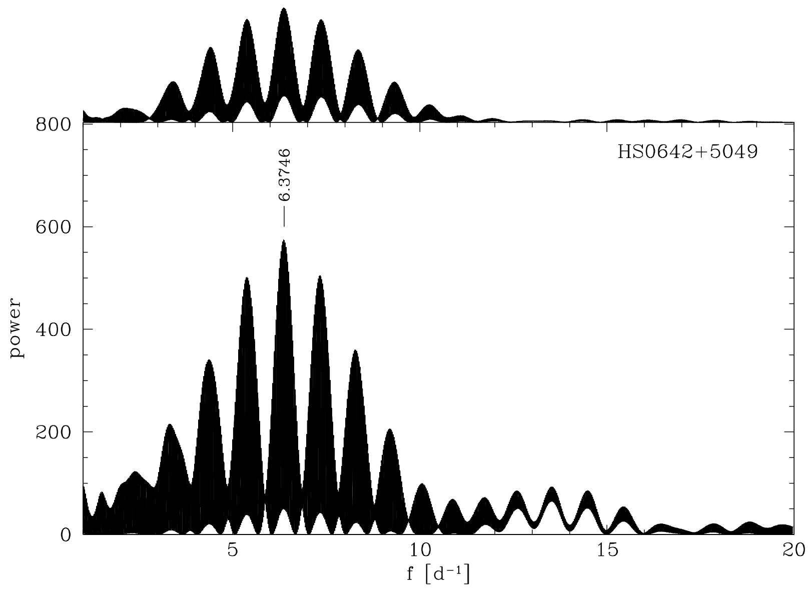

Figure 4.13: Scargle periodogram of HS 0642+5049 computed from the three longest nights of differential photometry obtained at the Calar Alto 2.2 m telescope (October 25, 2004) and the IAC80 telescope (December 8 & 9, 2004). The periodogram from a faked data set assuming a period of 225.90 min is shown in the *top panel*.

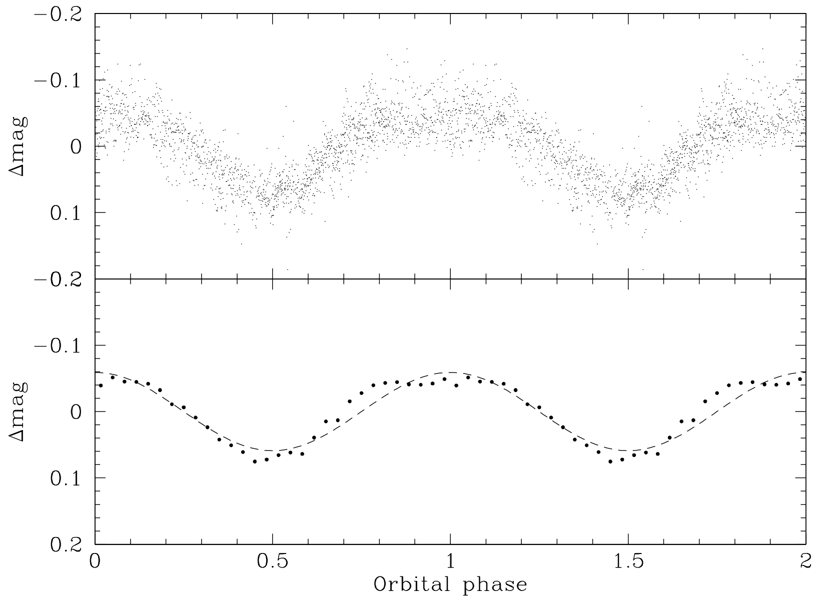

Figure 4.14: HS 0642+5049 photometric data from the Calar Alto 2.2 m telescope (October 25, 2004) and the IAC80 telescope (December 8 & 9, 2004) folded over $P_{\rm orb} = 225.90$ min *(top panel)*. The average light curve, binned into 30 phase, is shown in the *bottom panel* along with a sine fit (dashed line).

Table 4.1: Sine fits to the Hα emission line radial velocities. The methods employed were a convolution with a single Gaussian (SG) or Schneider & Young's (1980) double-Gaussian prescription (DG).

Object	Method	FWHM/Sep. ($\mathrm{km\,s^{-1}}$)	T_0 (days)	Period ($\mathrm{km\,s^{-1}}$)	K ($\mathrm{km\,s^{-1}}$)	γ
HS 0139+0559	SG	600	2452998.985 ± 0.013	0.16923 ± 0.00034	84.4 ± 4.8	18.4 ± 3.5
HS 0229+8016	SG	600	2452992.457 ± 0.006	0.161493 ± 0.000034	179.0 ± 5.2	35.5 ± 3.5
HS 0506+7725	DG	700/1500	2452990.679 ± 0.022	0.14770 ± 0.00014	42.6 ± 4.4	-66.7 ± 3.0

4.6 Discussion, part I

4.6.1 The inventory of the 3–4 h orbital period range

The primary aim of our search for CVs in the HQS is to establish the orbital periods and CV subtypes for a large sample of CVs that were selected in a homogeneous way based on their spectroscopic properties. The properties of this sample will then be compared with the predictions of CV evolution theory. Here, we present the spectroscopic identifications and detailed follow-up studies of HS 0139+0559, HS 0229+8016, HS 0506+7725, and HS 0642+5049, which have orbital periods of 243.69 min, 232.550 min, 212.7 min, and 225.90 min, respectively. This follows the trend noticed by Gänsicke et al. (2002b) and, more recently, by Gänsicke (2004) and Rodríguez-Gil (2005) that the majority of the new CVs identified in the HQS have orbital periods above the period gap and the bulk of them are concentrated in the 3–4 h orbital period range. Currently, orbital periods have been determined for 42 systems out of a total of 53 new HQS CVs, and Figure 4.15 compares the period distribution of these new HQS CVs with the period distribution of the CVs from the Ritter & Kolb catalogue (2003, V7.4). Although the follow-up of the new HQS CVs is not yet complete, it is already now clear that our survey *did not* identify the large number of short-period CVs predicted by the population models (e.g. Kolb 1993; Howell et al. 1997), even though our selection method (= detection of Balmer emission lines) is best suited for the identification of low mass-transfer systems that might be inconspicuous in other ways (variability, X-rays), such as the short-period dwarf novae HS 1449+6415 (Nogami et al. 2000) and HS 2219+1824 (Rodríguez-Gil et al. 2005a), or the ultra-short period HS 2331+3905, which might be a WZ Sge-type dwarf novae with extremely long outburst recurrence times (Araujo-Betancor et al. 2005a). The (somewhat preliminary) conclusion is that, if a large number of short-period CVs does indeed exist, they must look different from the well-known examples such as WZ Sge.

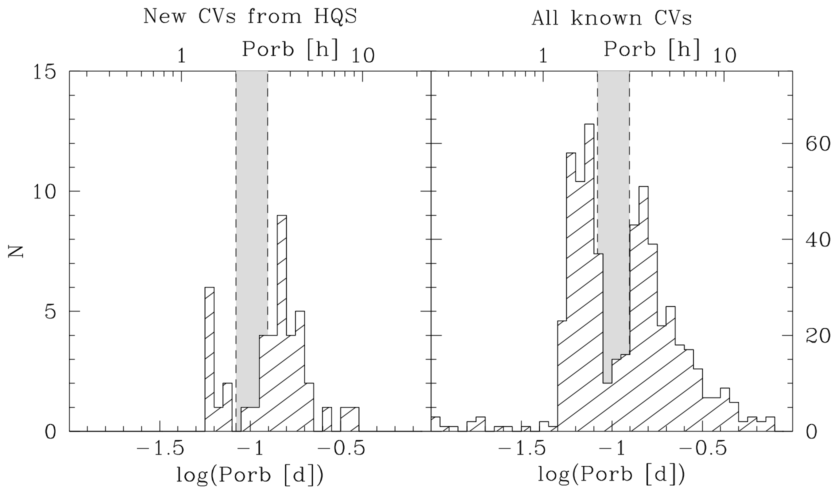

Figure 4.15: Period distribution of 42 new CVs discovered in the HQS *(left panel)* and that of all known CVs *(right panel*, from Ritter & Kolb 2003, V7.4). The 2–3 h period gap is shaded in gray.

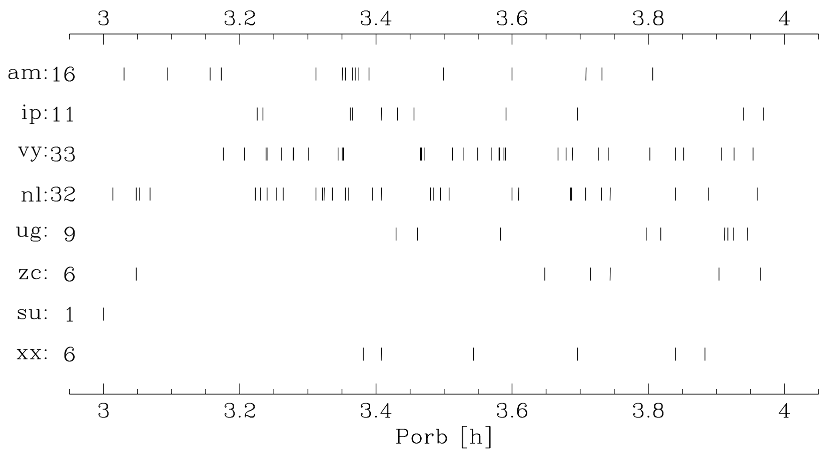

Figure 4.16: Period distribution of the individual CV subtypes in the 3–4 h period range. From *top* to *bottom*: polars (am), intermediate polars (ip), VY Scl and SW Sex stars (vy), novalike variables and nova remnants that are neither VY Scl nor SW Sex stars (nl), U Gem-type dwarf novae (ug), Z Cam-type dwarf novae (zc), SU UMa-type dwarf novae (su), and systems with undetermined CV subtype (xx).

The HQS CV survey has been very prolific in identifying relatively bright long-period CVs with a distinct preference for the 3–4 h period range (Figure 4.15, right panel), including the four new CVs presented in this chapter. The majority of these new long-period CVs are weak or no X-ray emitters, and they display little long-term variability – in fact, there are only five confirmed dwarf novae among the 28 new systems found above the gap. Gänsicke (2004) and Rodríguez-Gil (2005) pointed out the large number of SW Sextantis stars among the new HQS CVs, which represent 25% of all newly identified CVs above the gap, and nearly half of all new CVs in the 3–4 h period range. For comparison, we show in Figure 4.16 the inventory of the 3–4 h orbital period range according to Ritter & Kolb (2003, V7.4). We find that 114 CVs (20% of all CVs with known $P_{\rm orb}$) inhabit the 3–4 h period range, of which 27 (24%) are confirmed magnetic systems (intermediate polars, polars). 33 (29%) belong to the group of either VY Scl or SW Sex stars, which share similar properties, and are suspected to contain magnetic white dwarfs as well (e.g. Rodríguez-Gil et al. 2001; Hameury & Lasota 2002). While the ratio of definite magnetic CVs in the 3–4 h period range (24%) is already very high compared to the incidence of magnetism in isolated white dwarfs (Liebert et al. 2003), confirmation of significant magnetism in the white dwarfs in VY Scl/SW Sex stars would raise the ratio of magnetic/non-magnetic CVs well above 50%, which conflicts with any of the current models of CV evolution. Whatever the verdict on the magnetic properties of VY Scl/SW Sex stars will be, the large number of CVs belonging to this type suggests that they represent an important phase of CV evolution rather than some unusual combination of their physical properties. For completeness, 32 (28%) novalike variables that do not belong to either the VY Scl or SW Sex class populate the 3–4 h period range[1]. While a number of those systems definitely do not share any of the VY Scl/SW Sex properties, a fair fraction of these systems has been studied only in a very limited way, and hence some of them might well join the VY Scl/SW Sex class upon more detailed scrutiny. Rodríguez-Gil et al. (2007a) have started a spectroscopic program to provide more detailed studies of these systems, classifying 35 out of 93 of novalike/classical nova population as SW Sex stars.

[1]The classification of Ritter & Kolb 2003 is somewhat confusing, as their use of the UX UMa type disagrees with the more common definition of systems characterised by persistent broad Balmer absorption lines.

Finally, 16 (14%) dwarf novae are known in the 3–4 h period range, and the scarcity of systems undergoing thermal disc instabilities just above the period gap is a well-known fact (e.g. Shafter et al. 1986; Shafter 1992).

4.6.2 The nature of the four new CVs

Based on observational characteristics (summarised in Table 4.2), we discuss the likely nature of the four new CVs.

HS 0506+7725 shows short time scale flickering with quasi-periodic oscillations on time scales of $\sim$15 min. The relatively narrow emission lines and the low amplitude of the radial velocity variations suggest a low inclination. The system has been detected in the RASS (Voges et al. 2000) at 0.07 cts s^{-1} (1RXS J051336.1+772836) with a hard spectrum, and has been previously detected as an X-ray source by EINSTEIN (2E 0506.1+7725). The presence of moderately strong He II λ4686 emission in the identification spectrum independently confirms the presence of ionising radiation in the system. The detection of a deep low state at $B \simeq 18.3$ on one of the HQS prism plates clearly identifies the system as a VY Scl star. The system does not display evidence *at face value* of being an SW Sex star; but as it is obviously a low-inclination binary, a spectroscopic study at higher resolution would be useful to test for anomalous radial velocity behaviour in the emission lines.

The other three systems, HS 0139+0559, HS 0229+8016, and HS 0642+5049 are spectroscopically very similar, being characterised by thick-disc absorption line spectra. The fact that we have observed them on various occasions and found them always at nearly the same magnitude and with the same spectral properties[2] makes it very unlikely that these systems are U Gem-type dwarf novae observed during outburst. While HS 0139+0559 and HS 0229+8016 are not detected in the RASS, a faint X-ray source is found near HS 0642+5049 (1RXS J066618.4+504601, 0.02-

[2]With one exception: HS 0229+8016 was observed in August 1992 in a somewhat fainter state, $V \simeq 15.0$, compared to its typical brightness near 14 mag. On that occasion, the Balmer and He I absorption lines were absent/weak, and the strength of the emission lines had markedly increased.

cts s^{-1}), which coincides within the 29$''$ position error of the RASS detection with the CV. The fact that there are no other nearby objects suggests that HS 0642+5049 is a weak X-ray emitter. None of the systems shows strong flickering activity. One puzzling difference among the three systems is that, whereas HS 0139+0559 and HS 0229+8016 show no or only very low-amplitude orbital photometric variability but exhibit clean quasi-sinusoidal radial velocity variations in their emission lines, HS 0642+5049 does not display any radial velocity variation but shows a 0.2 mag photometric modulation. It is very difficult to reconcile this opposite difference in spectroscopic/photometric behaviours in the simple picture of a high mass-transfer CV with a steady-state accretion disc. Based on our data, we identify all three systems either as UX UMa-type novalike variables or as Z Cam-type dwarf novae observed in periods of standstill. Optical long-term monitoring will be necessary to distinguish between these two possibilities.

4.7 Summary

We have identified HS 0139+0559, HS 0229+8016, HS 0506+7725, and HS 0642-+5049 as long-period CVs with orbital periods of 243.69 ± 0.49 min, 232.550 ± 0.049 min, 212.7 ± 0.2 min, and 225.90 ± 0.23, respectively. HS 0506+7725 is a VY Scl novalike variable characterised by a strong emission-line spectrum. HS 0139-+0559, HS 0229+8016, and HS 0642+5049 have thick-disc spectra and are either UX UMa-type novalike variables or Z Cam-type dwarf nova. None of the objects is a strong X-ray source or displays large-amplitude outbursts, which underlines the strength of CV surveys of spectroscopically selected candidates.

Table 4.2: Comparison of the observational characteristics of the four new CVs. The (non-)detection of X-ray emission refers to the ROSAT All Sky Survey (Voges et al. 2000). The CV subtypes are abbreviated as UX = UX UMa-type novalike variable, ZC = Z Cam-type dwarf nova, VY = VY Scl star.

Object	$P_{\rm orb}$ [min]	Radial velocity variation	Photometric variability: Orbital	Photometric variability: Flickering	Photometric variability: Long-term	X-ray	type
HS 0139+0559	243.7	clean, moderate amplitude	none	none	none	no	UX or ZC
HS 0229+8016	232.6	clean, large amplitude	very low amplitude	none	$\sim$ 1.3 mag	no	UX or ZC
HS 0506+7725	212.7	scatter, low amplitude	not obvious	large amplitude	$\sim$ 3 mag low state	yes	VY
HS 0642+5049	225.9	very low amplitude	moderate amplitude	low amplitude	none	maybe	UX or ZC

Chapter 5

Dwarf novae in the Hamburg Quasar Survey: Rarer than expected

5.1 Introduction

Dwarf novae are a subset of non- (or weakly) magnetic CVs that quasi-periodically brighten by several magnitudes. They are further subclassified into three types according to their outburst behaviours, i.e. U Gem-type dwarf novae, Z Cam-type dwarf novae, and SU UMa-type dwarf novae (see Section 1.3 for classification scheme). The commonly accepted cause for dwarf nova outbursts is a thermal instability in the accretion disc (e.g. Cannizzo et al. 1986; Osaki 1996). Within this theoretical framework, accretion discs undergo outbursts if the accretion rate is below a critical value, $\dot{M}_{\rm crit}$. Above the $2-3$ h period gap, the mass-transfer rate in CVs is typically larger than $\dot{M}_{\rm crit}$, and consequently only ~ 25 % of all CVs with $P_{\rm orb} > 3$ h are dwarf novae. For $P_{\rm orb} < 3$ h, the fraction of dwarf novae is ~ 62 %. The large difference in mass-transfer rate between short- and long-period systems is explained within the standard CV evolution theory by the cessation of magnetic braking once the systems evolve down to 3 h. Below $P_{\rm orb} = 3$ h, the evolution of CVs proceeds then much slower, and with lower mass-transfer rates, driven only by gravitational radiation as the angular momentum loss mechanism (e.g. Rappaport et al. 1983; King 1988). For such low mass-transfer rates, the disc instability model predicts thermally unstable accretion discs that produce dwarf-nova outbursts (Cannizzo 1993; Osaki 1996).

As suggested by their name, dwarf novae are predominantly discovered because of their outbursts (Gänsicke 2005), and hence CVs with very long outburst recurrence times or low-amplitude outbursts could be substantially underrepresented in the known CV population. In this chapter, I present five new dwarf novae discovered in the HQS independently of their variability. Their identification spectra suggest that they are dwarf novae observed in quiescence, dominated by low-excitation emission lines and lacking strong He II λ4686 emission. These systems are HS 0417+7445, HS 1016+3412, HS 1340+1524, HS 1857+7127, and HS 2214+2845. Their orbital periods span from ~ 1.5 h to nearly 5 h. The details of observations and data reduction of these objects are provided in Chapter 2. Apart from several sets of time-resolved observations, additional images of these objects were taken intermittently at the the 0.37 m robotic Rigel telescope of the University of Iowa to record their variability during the period May 2004 to April 2005. The observed properties of the five new dwarf novae and their orbital period measurements are described in Sections 5.2–5.7. In Section 5.8, I compare the period distribution of dwarf novae found in the HQS to that of all known dwarf novae and discuss the implications of the HQS survey work on the space density of CVs.

Table 5.1: Properties of the five new dwarf novae.

	HS 0417+7445	HS 1016+3412	HS 1340+1524	HS 1857+7127	HS 2214+2845
Right ascension (J2000)	$04^{h}23^{m}32.8^{s}$	$10^{h}19^{m}47.3^{s}$	$13^{h}43^{m}23.2^{s}$	$18^{h}57^{m}20.4^{s}$	$22^{h}16^{m}31.2^{s}$
Declination (J2000)	$+74^{\circ}52'50.30''$	$+33^{\circ}57'53.9''$	$+15^{\circ}09'16.9''$	$+71^{\circ}31'19.2''$	$+29^{\circ}00'20.6''$
Period (min)	$\simeq 105.1/\simeq 109.9$	114.3 ± 2.7	92.66 ± 0.17	272.317 ± 0.001	258.02 ± 0.56
Magnitude range	18.0 – 13.5	18.6 – 15.4:	18.5 – 14.2	17.2 – 13.9	16.5 – 12.3
Hα EW [Å] / FHWM [Å]	172 / 43	184 / 27	121 / 28	39 / 32	53 / 33
Hβ EW [Å] / FHWM [Å]	98 / 43	125 / 25	88 / 23	33 / 32	42 / 31
Hγ EW [Å] / FHWM [Å]	73 / 38	85 / 24	59 / 22	27 / 33	30 / 32
He I λ5876 EW [Å] / FHWM [Å]	40 / 43	52 / 31	36 / 30	7 / 34	7 / 25
He I λ6678 EW [Å] / FHWM [Å]	7 / 30	26 / 35	18 / 32	3 / 46	5 / 39
RASS source (1RXS J)	042332.8+745300	101946.7+335811	134323.1+150916	185722.6+713126	221631.2+290025
RASS count rate $(0.01\,\mathrm{cts\,s^{-1}})$	6.0 ± 1.3	2.5 ± 1.0	7.3 ± 1.7	3.4 ± 4.5	9.9 ± 1.5
Hardness ratio HR1	1.00 ± 0.09	1.00 ± 0.91	0.18 ± 0.23	1.00 ± 0.04	0.92 ± 0.06
Hardness ratio HR2	0.21 ± 0.20	-0.32 ± 0.38	-0.05 ± 0.27	0.69 ± 0.10	0.10 ± 0.14

Notes. The coordinates are taken from the USNO-B catalogue (Monet et al. 2003); the ROSAT PSPC count rates and hardness ratios HR1 and HR2 have been obtained from the ROSAT All Sky Survey (RASS) Bright Source Catalogue (Voges et al. 1999) and from the RASS Faint Source Catalogue (Voges et al. 2000); the Hα–Hγ and He I λ5876, 6678 equivalent widths (EW) and full width at half maximum (FWHM) were measured from CAFOS average spectra (Figure 5.1) using the `integrate/line` task in `MIDAS`; the outburst of HS 1016 is uncertain (marked by a colon), as only one outburst was observed.

5.2 HS 0417+7445

5.2.1 HS 0417+7445 as a SU UMa dwarf nova

HS 0417+7445 was spectroscopically identified as a CV in October 1996, at the Calar Alto 2.2 m telescope. The identification spectrum (Figure 5.1) contains strong Balmer emission lines together with weaker lines of He I that are a characteristic of CVs. He II λ4686 is very weak, suggesting that HS 0417+7445 is a dwarf nova observed in quiescence. HS 0417+7445 is contained in the ROSAT Bright Source Catalogue as 1RXS J042332+745300 (Voges et al. 1999), and has been independently identified as a CV by Wu et al. (2001). HS 0417+7445 displayed large-amplitude variability on the HQS spectral plates, where it was detected at $B \simeq 18.0$ in June 1992 and at $B \simeq 13.5$ in January 2001, supporting the suggested dwarf nova nature of the object.

Throughout the period December 2000 to January 2005, supplement photometric observations for HS 0417+7445 were obtained at the Wendelstein telescope, the OLT, and the INT (~ 25 h, in total). The object was found near a mean magnitude of $\simeq 17.5$ (December 2000: $B \simeq 17.9$, February 2003: $R \simeq 17.3$, November 2004: filterless $\simeq 17.6$, January 2005: $g' \simeq 17.5$), consistent with the USNO-A2.0 measurements, $R \simeq 17.2$ and $B \simeq 16.8$, except during January 2001, when the system was found in an outburst near $B \simeq 13.5$. In the quiescent state, the light curve of HS 0417+7445 is characterised by a double-humped pattern with a period of ~ 100 min (Figure 5.2, bottom panel). The light curve obtained during the January 2001 outburst (Figure 5.2, top panel) reveals superhumps that identify HS 0417+7445 as a SU UMa-type dwarf nova, and therefore this outburst as a superoutburst. An additional outburst of HS 0417+7445 was caught on the rise in April 10, 2005 by P. Schmeer with the Rigel telescope, and ~ 3 h, V-band data obtained by D. Boyd on the evening of April 11, 2005 showed the object already declining at a rate of ~ 0.85 mag d^{-1} and no evidence of superhumps was found.

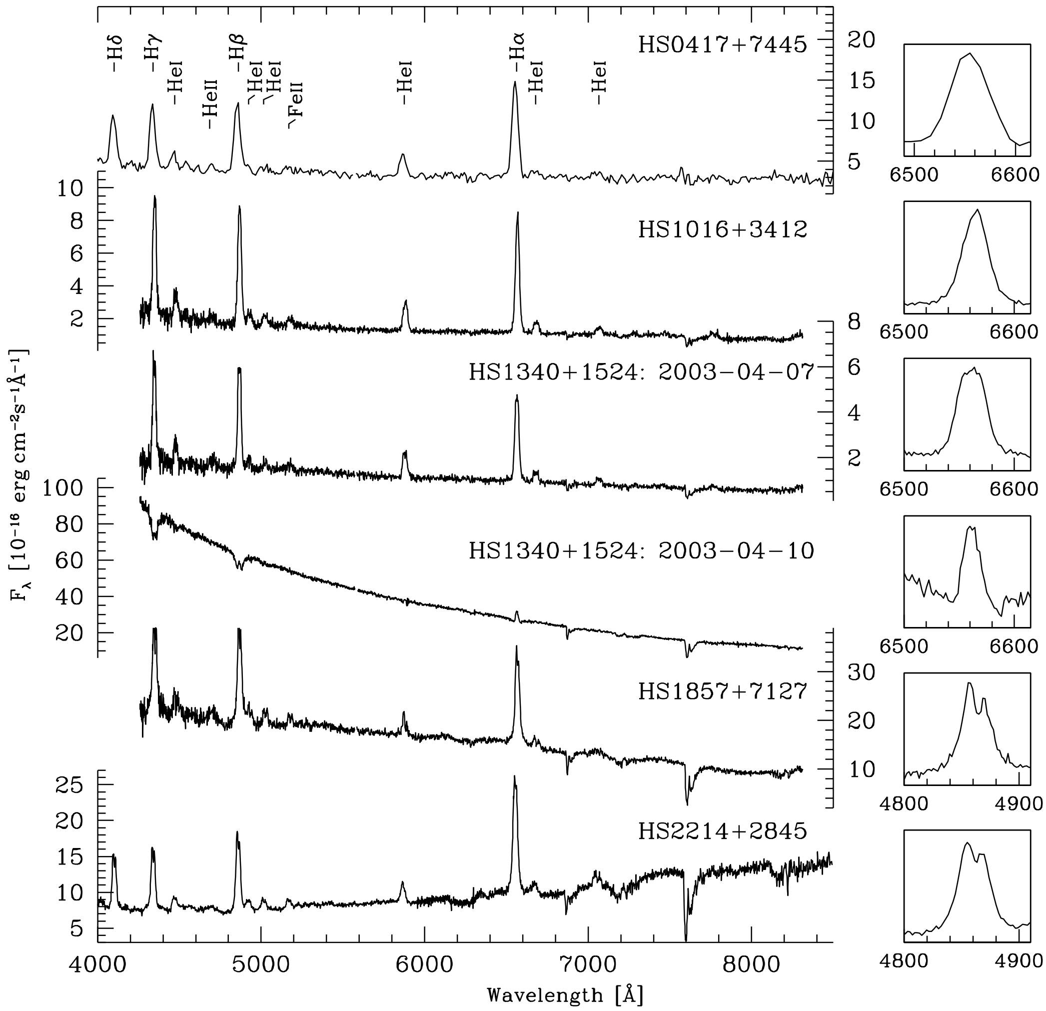

Figure 5.1: *Main panel*: flux-calibrated CAFOS spectra of HS 0417+7445, HS 1016+3412, HS 1340+1524, HS 1857+7127, and HS 2214+2845. Fluxes are labelled alternatingly on the left and right side. HS 1340+1524 was observed in quiescence and outburst, respectively. *Right panel*: close-up plots of the Hα and Hβ profiles.

By April 18, the system reached again its quiescent magnitude of $V \simeq 17.5$.

5.2.2 The orbital and superhump periods

In order to measure the orbital period of the system, a Scargle (1982) periodogram was computed within the `MIDAS/TSA` context from all quiescent data, except the

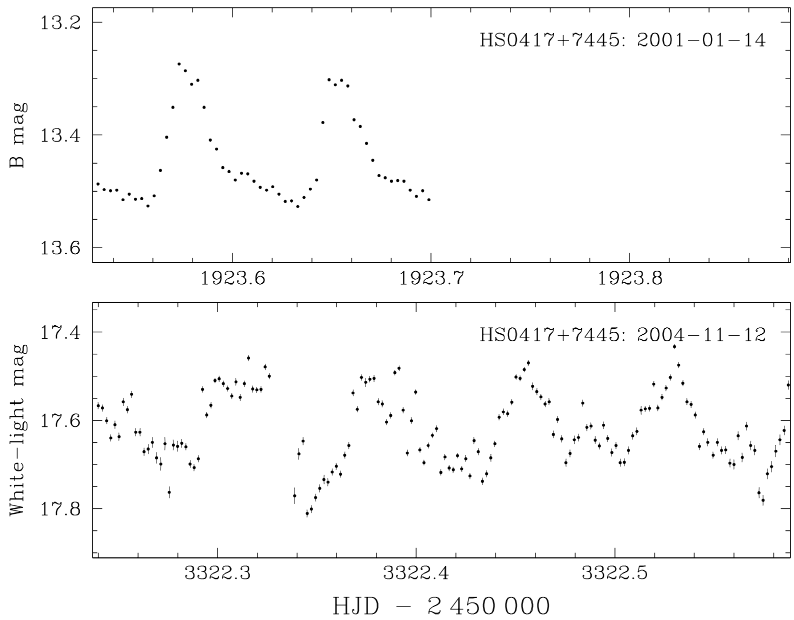

Figure 5.2: Sample light curves of HS 0417+7445 obtained at the Wendelstein observatory. *Top panel*: *B*-band data obtained during superoutburst on January 14, 2001. *Bottom panel*: filterless data obtained during quiescence.

February 2003 observations in which the data were of too poor a quality. The periodogram (Figure 5.3) contains a fairly broad sequence of aliases spaced by 1 d^{-1}, with the strongest signal at 13.7 d^{-1} and a nearly equally strong signal at 13.1 d^{-1}. The high-frequency range of the periodogram of HS 0417+7445 is nicely reproduced by the window function (shifted to 13.7 d^{-1} in the top panel of Figure 5.3), but excess power is present at frequencies below 10 d^{-1}, most likely associated with the short lengths of the observing runs. Sine-fits to the data result in the periods corresponding to the two highest peaks in the periodogram, $P \simeq 105.1$ min and $P \simeq 109.9$ min, respectively. We interpreted these values as possible orbital periods of HS 0417+7445.

The Scargle periodogram computed from the superoutburst data obtained on January 14, 2001 provides a broad signal with a peak at $\simeq 13.3\,\mathrm{d}^{-1}$, or $P \simeq 108.3$ min. The light curve folded over this period shows, however, a significant offset between the two observed superhump maxima. A periodogram computed

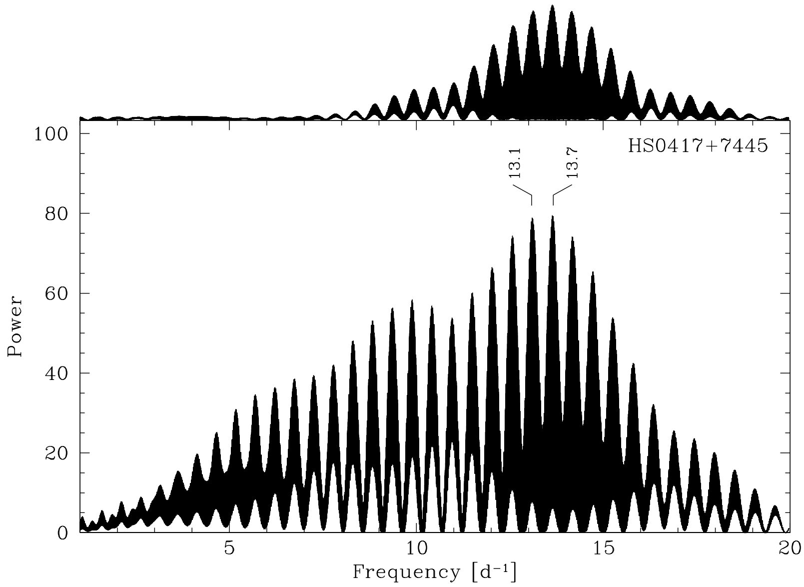

Figure 5.3: *Main panel*: Scargle periodogram of HS 0417+7445 during quiescence computed from all photometric data except February 27, 2003. *Top panel*: the window function shifted to 13.7 d^{-1}.

using Schwarzenberg-Czerny's (1996) analysis-of-variance (AOV) method using orthogonal polynomial fits to the data (implemented as `ORT/TSA` in `MIDAS`) results in a much narrower peak compared to the Scargle analysis, centred at 12.95 d^{-1} ($P \simeq 111.2$ min). This period provides a clean folded light curve. This improvement in the period analysis underlines the fact that AOV-type methods provide better sensitivity for strongly non-sinusoidal signals (such as superhumps) compared to Fourier-transform based methods.

The analysis of our photometric data left us with two candidate orbital periods, $P_{\rm orb} = 105.1$ min or $P_{\rm orb} = 109.9$ min, and two candidate superhump periods, $P_{\rm sh} = 108.3$ min or $P_{\rm sh} = 111.2$ min. Table 5.2 lists the fractional superhump excess, $\varepsilon = (P_{\rm sh} - P_{\rm orb})/P_{\rm orb}$ calculated from all possible combinations of the candidate periods. We consider cases (2) and (3) as very unlikely, as no dwarf nova with $\varepsilon > 5\%$ is found below the period gap and no short-period dwarf nova with a negative superhump excess is known (e.g. Nogami et al. 2000; Patterson et al. 2003;

Table 5.2: The fractional superhump excess of HS 0417+7445 computed from $\varepsilon = (P_{\rm sh} - P_{\rm orb})/P_{\rm orb}$.

Case	$P_{\rm orb}$ (min)	$P_{\rm sh}$ (min)	ε
1	105.1	108.3	0.030
2	105.1	111.2	0.058
3	109.9	108.3	-0.015
4	109.9	111.2	0.012

Rodríguez-Gil et al. 2005a). In fact, most dwarf novae with $P_{\rm orb} \sim 100 - 115$ min have $\varepsilon \sim 3 - 4\%$ (Patterson et al. 2005), which would make case (1) look most likely. However, based on our data, we prefer case (4) as $P_{\rm sh} = 111.2$ min gave the cleanest folded superhump light curve. In this case, HS 0417+7445 would have a rather low value of ε, similar only to KV And ($P_{\rm orb} = 105.49 \pm 0.30$ min) which has $\varepsilon = 0.0145$ (Patterson et al. 2003). An unambiguous determination of both $P_{\rm orb}$ and $P_{\rm sh}$ would be important, as ε may be used to estimate the mass ratio of a CV (Patterson et al. 2005).

5.3 HS 1016+3412

5.3.1 Spectroscopic characteristics

An identification spectrum of HS 1016+3412 was obtained at the Calar Alto 2.2 m telescope in April 2001. The spectrum is similar to that of HS 0417+7445 dominated by low-excitation emission lines as well as lacking strong He II λ4686, suggesting that HS 1016+3412 is a dwarf nova observed in quiescence.

In addition, we obtained time-resolved spectroscopy of HS 1016+3412 (70 spectra) with CAFOS and IDS during the period April/May 2003 and Febuary 2005. The CAFOS (Figure 5.1) and IDS average spectra of HS 1016+3412 are similar to the identification spectrum, with strong Balmer emission lines together with weaker

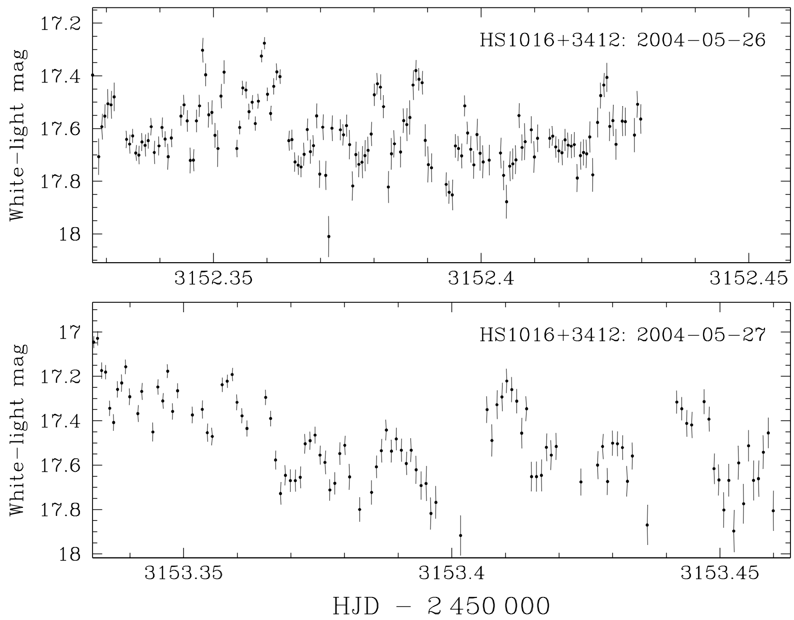

Figure 5.4: Sample filterless light curves of HS 1016+3412 obtained at the Kryoneri observatory.

He I and Fe II lines and practically absent He II λ4686. The single-peaked profile found in the emission lines suggests a relatively low orbital inclination. No spectral contribution from the secondary star is detected in the red part of the spectrum. The equivalent widths (EWs) from the CAFOS and IDS average spectra do not show any noticeable variation in each epoch throughout our run. Table 5.1 lists FWHM and EW parameters of the CAFOS average spectrum measured from Gaussian fits.

5.3.2 Photometric characteristics

The spectroscopic observations of HS 1016+3412 were supplemented by time-resolved photometry obtained in May 2004, using the Kryoneri and IAC80 telescopes. The light curves of HS 1016+3412 display short-time scale flickering with an amplitude of $\sim 0.2-0.3$ mag with no sign of orbital modulation (Figure 5.4). During the May 2004 observations, the system was found consistently at a magnitude of $\simeq 17.5$; the USNO-A2.0 catalogue lists $R \simeq B \simeq 17.8$. In April 2003, however, the system was found fainter, $V \simeq 18.6$, in the CAFOS acquisition images. The only known outburst of HS 1016+3412 was detected using the Rigel telescope on November 2, 2004, where an unfiltered magnitude of 15.4 was recorded. The next image obtained on November 11, 2004, showed the system again at its quiescent magnitude of $\simeq 17.5$.

5.3.3 The orbital period

In order to determine the orbital period of HS 1016+3412, we measured the radial velocity variations of Hα, the strongest emission line, from the CAFOS and IDS spectra. We first rebinned the individual spectra to a uniform velocity scale centred on Hα, and followed by normalising the slope of the continuum. We then measured the Hα radial velocity variation using the double-Gaussian method of Schneider & Young (1980) with a separation of $1000\,\mathrm{km\,s^{-1}}$ and an FWHM of $200\,\mathrm{km\,s^{-1}}$. A Scargle periodogram calculated from the Hα radial velocity variation contains a set of narrow aliases spaced by $1\,\mathrm{d^{-1}}$, with the strongest signal found at $f \simeq 12.6\,\mathrm{d^{-1}}$ (Figure 5.5, top panel). We tested the significance of this signal by creating a faked set of radial velocities computed from a sine function with a frequency of $12.6\,\mathrm{d^{-1}}$, and randomly offset from the computed sine wave using the observed errors. The periodogram of the faked data set is plotted in a small window of the top panel in Figure 5.5 which reproduces well the alias structure of the periodogram calculated from the observation. A sine-fit to the folded radial velocities (Figure 5.6, see Table 5.3 for the fit parameters) refined the period to 114.3 ± 2.7 min, which we interpreted as the orbital period of HS 1016+3412.

As suggested by visual inspection of the light curves, a Scargle periodogram computed from the entire photometry as well as from individual subsets did not reveal any significant signal.

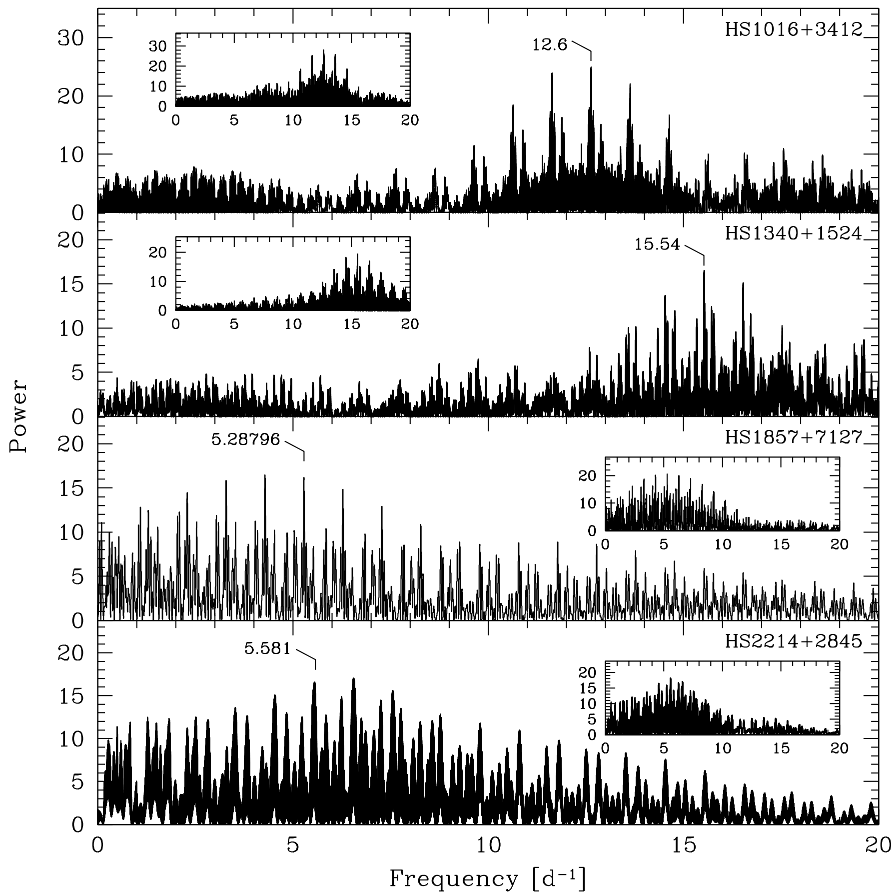

Figure 5.5: *Main panel*: Scargle periodograms calculated from the radial velocities of HS 1016+3412, HS 1340+1524, HS 1857+7127, and HS 2214+2845 measured from their Hα emissions (for first three systems) and from Hα plus Hβ (for HS 2214+2845). *Small windows*: the periodograms constructed from faked sets of data generated for the corresponding orbital frequency.

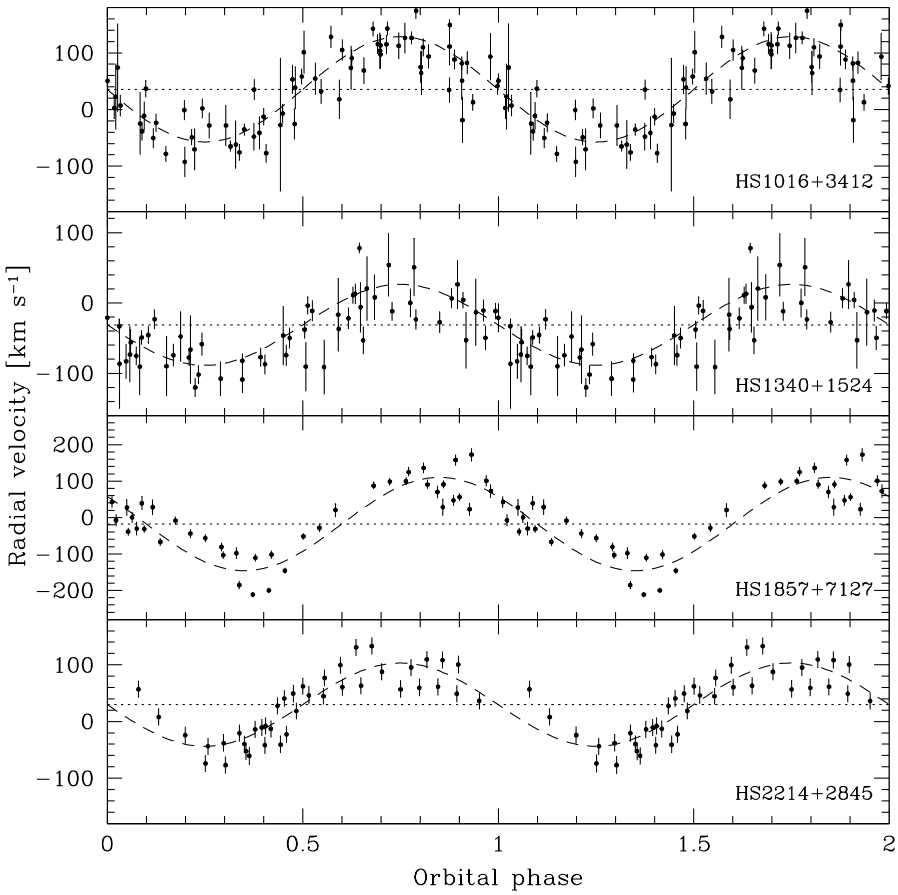

Figure 5.6: *Top two panels*: the Hα radial velocities of HS 1016+3412 and HS 1340+1524 folded over their spectroscopic periods of 114.3 min and 92.66 min, respectively. *Bottom two panels*: the Hα radial velocities of HS 1857+7127 and Hα plus Hβ radial velocities of HS 2214+2845 folded over their photometric periods of 272.317 min and 258.02 min, respectively. The data of HS 1857+7127 were folded using the eclipse ephemeris given in Equation 5.1 while the other three systems were folded, defining phase zero as the time of red-to-blue crossing of the radial velocities.

Table 5.3: Sine fits to the Hα radial velocities of HS 1016+3412, HS 1340+1524, and HS 1857+7127. For HS 2214+2845, a combination of Hα and Hβ radial velocities were fitted, as the September 2000 Calar Alto spectra did not cover Hα. For HS 1857+7127 and HS 2214+2845, the periods were fixed to their values determined from the photometry.

Object	T_0	Period (days)	K ($\mathrm{km\,s^{-1}}$)	γ ($\mathrm{km\,s^{-1}}$)
HS 1016+3412	2452737.4039 ± 0.0012	0.0794 ± 0.0019	93.0 ± 5.3	35.6 ± 3.9
HS 1340+1524	2452737.4438 ± 0.0018	0.06435 ± 0.00012	57.5 ± 6.2	-31.1 ± 4.1
HS 1857+7127	$2452368.53243 \pm 0.00098$	0.189109 ± 0.000001	128.0 ± 9.6	-17.9 ± 7.4
HS 2214+2845	2451812.3309 ± 0.0028	0.17918 ± 0.00039	73.5 ± 6.5	29.8 ± 5.0

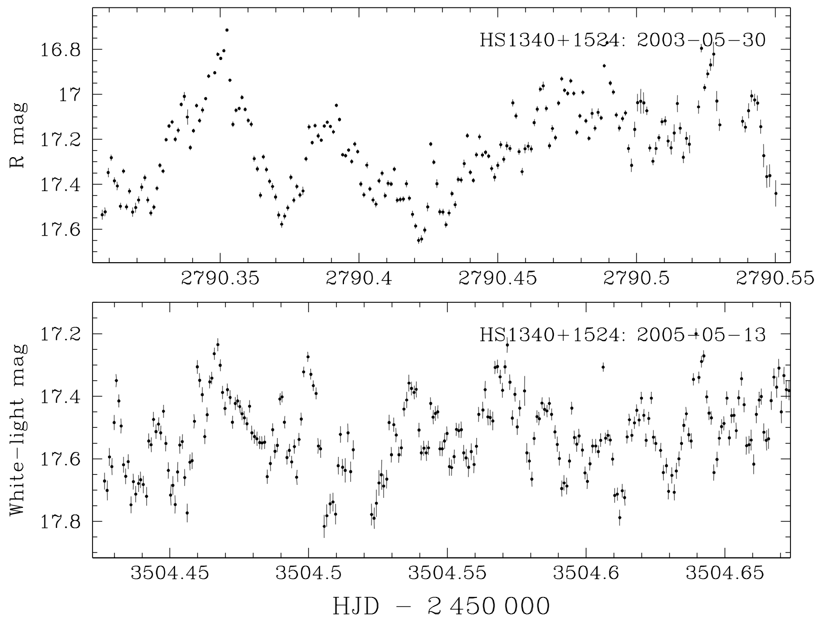

Figure 5.7: Sample light curves of HS 1340+1524. *Top panel*: *R*-band data obtained at the Kryoneri observatory. *Bottom panel*: filterless data obtained at the IAC80 telescope.

5.4 HS 1340+1524

HS 1340+1524 was identified as a non-magnetic CV in May 2001 from its spectrum, which looks identical to that of HS 0417+7445 and HS 1016+3412. Time-resolved spectroscopy of HS 1340+1524 (78 spectra) was obtained in April 2003 and Febuary 2005 at the Calar Alto 2.2 m telescope and at the INT. HS 1340+1524 was classified as a dwarf nova when an outburst was detected in our CAFOS data, on April 10, 2003. Figure 5.1 (middle two panels) shows the average CAFOS spectra of HS 1340+1524 during quiescence and outburst, respectively. The average spectrum during quiescence is similar to that of HS 0417+7445 and HS 1016+3412, showing strong single-peaked line profiles of Balmer emission along with the weaker lines of He I and Fe II. The line parameters during quiescence are given in Table 5.1.

5.4.1 Long and short term variability

Throughout our time-series photometry (May 2001 to May 2005) obtained at the AIP, IAC80, FLWO, and Kryoneri telescopes, HS 1340+1524 was found at a mean magnitude in the range $\sim 17.7 - 16.8$ (see Figure 5.8, main window). A first outburst of HS 1340+1524 was detected on the evening of April 10, 2003 during spectroscopic observations with the Calar Alto 2.2 m telescope. The outburst magnitude was $V \simeq 14.7$ on the CAFOS acquisition image. The spectra obtained immediately thereafter showed weak emission at Hα, with an equivalent width of ~ 4.7 Å, whereas Hβ and Hγ were in absorption with narrow emission cores, which are typical of an optically thick accretion disc (Figure 5.1). Similar spectra were observed in the three HQS CVs: HS 0139+0559, HS 0229+8016, and HS 0642+5049 (Chapter 4). As the conditions during the night deteriorated, we switched to time-series photometry, recording a decline at $\sim 0.05\,\mathrm{mag\,hr^{-1}}$. The CAFOS acquisition images showed that HS 1340+1524 faded to $V \simeq 16.1$ and $V \simeq 17.3$ in the two subsequent nights, April 11 and 12, 2003, respectively. A puzzling fact is that acquisition images taken on three nights, April 7, 8, and 9, 2003, before the outburst showed HS 1340+1524 at $V \simeq 18.5$, i.e. nearly one magnitude fainter than the usual quiescent value (see Figure 5.8, small window). On April 28, a CAFOS acquisition image showed the system again at a filterless magnitude of 17.6, consistent with the typical quiescent brightness. The duration of the entire outburst was less than two days.

A second outburst reaching an unfiltered magnitude of ~ 14.2 was recorded on April 15, 2005 with the Rigel telescope; again, the duration of the outburst was of the order of $2 - 3$ days.

The light curves of HS 1340+1524 obtained during quiescence are predominantly characterised by variability on time scales of $\sim 15 - 20$ min with peak-to-peak amplitudes of ~ 0.4 mag (Figure 5.7, bottom panel). On some occasions, the light curves show hump-like structures which last for one to several hours, superim-

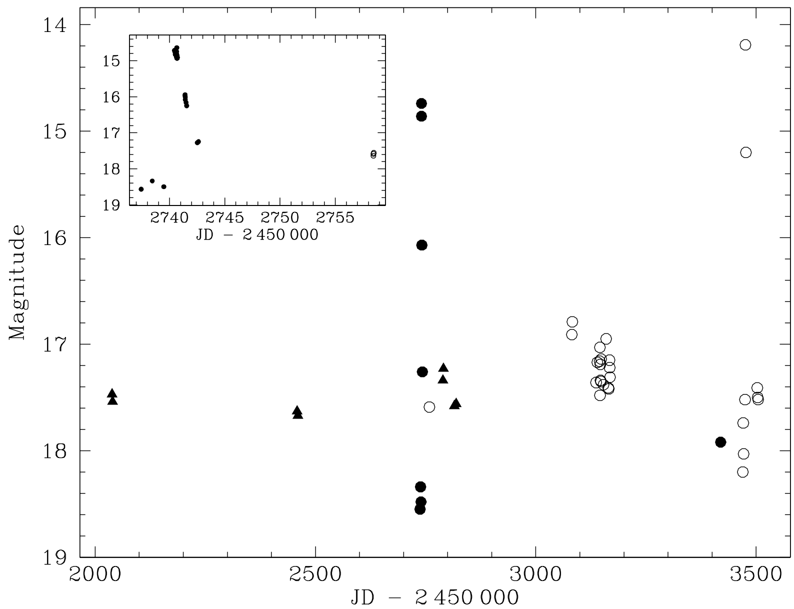

Figure 5.8: *Main window*: the mean magnitudes of HS 1340+1524 obtained from May 2001 to May 2005 in *R*-band (filled triangles), *V*-band (filled circles), and white light (open circles). The photometric error on the individual points is < 0.05 mag. An additional systematic uncertainty arises from the combination of different band passes. Considering the apparent magnitudes of HS 1340+1524 listed in the Sloan Digital Sky Survey which are $g = 17.3$, $r = 17.1$, and $i = 17.1$, the errors due to colour terms are likely to be within ± 0.1 mag. *Small window*: close up of the April 2003 CAFOS run. The first three points show the deeply faint state with a mean magnitude of $V \simeq 18.5$ before the outburst on April 10, 2003.

posed by short-time scale flickering (e.g. Figure 5.7, top panel). Our period analysis of the photometric data did not reveal any stable signal in the combined data.

In summary, HS 1340+1524 appears to have rather infrequent and short-lived outbursts, and displays a substantial amount of short-term variability as well as variability of its mean magnitude during quiescence.

5.4.2 The orbital period

The orbital period of HS 1340+1524 was determined using the spectroscopic data taken in quiescence both with CAFOS and IDS. The Hα radial velocity variation was measured in the same manner as in HS 1016+3412 with a separation of 1000 $\mathrm{km\,s^{-1}}$ and an FWHM of 200 $\mathrm{km\,s^{-1}}$. Figure 5.5 (second panel) shows the Scargle periodogram of HS 1340+1524. The strongest signal is found at $f = 15.54 \pm 0.03\,\mathrm{d^{-1}}$, where the error is estimated from the FWHM of the strongest peak in the periodogram, corresponding to an orbital period of $P_{\mathrm{orb}} = 92.66 \pm 0.17$ min. The Hα radial velocity curve folded over this period is shown in Figure 5.6 (second panel) along with a sine-fit; the fit parameters are given in Table 5.3. The periodogram of a faked data set constructed from this frequency agrees well with the entire observed alias structure (insert in Figure 5.5, second panel).

With the spectroscopic period being determined, we re-analysed the time-series photometry of HS 1340+1524, and found no significant signal in the range of the orbital frequency when we combined all quiescent data. However, a weak signal at a frequency of $\sim 15.5\,\mathrm{d^{-1}}$ and its one-day aliases were detected intermittently on some occasions, e.g. in the 2003 Kryoneri data and the 2004 FLWO observations.

5.5 HS 1857+7127

HS 1857+7127 was identified as a typical CV, showing Balmer and He I emission in its spectrum, in July 1990 at the Calar Alto 2.2 m telescope. Additional time-resolved spectroscopy of HS 1857+7127 (41 spectra) was obtained in April 2003 with CAFOS and IDS. The CAFOS average spectrum of HS 1857+7127 (Figure 5.1) is similar to the spectra of HS 0417+7445, HS 1016+3412, and HS 1340+1524, presenting a blue slope superimposed by Balmer and He I emission lines. Slight flux depressions are observed near 6200 Å and 7200 Å, which might be associated with the TiO bands of an M-type donor, however, the quality of the data is insufficient to unambiguously establish the detection of the secondary star. The Balmer emission line profiles are double-peaked, with a peak-to-peak separation of $\sim 800\,\mathrm{km\,s^{-1}}$, suggesting a moderate to high inclination of the system. A high orbital inclination of HS 1857+7127 was confirmed by the detection of eclipses in

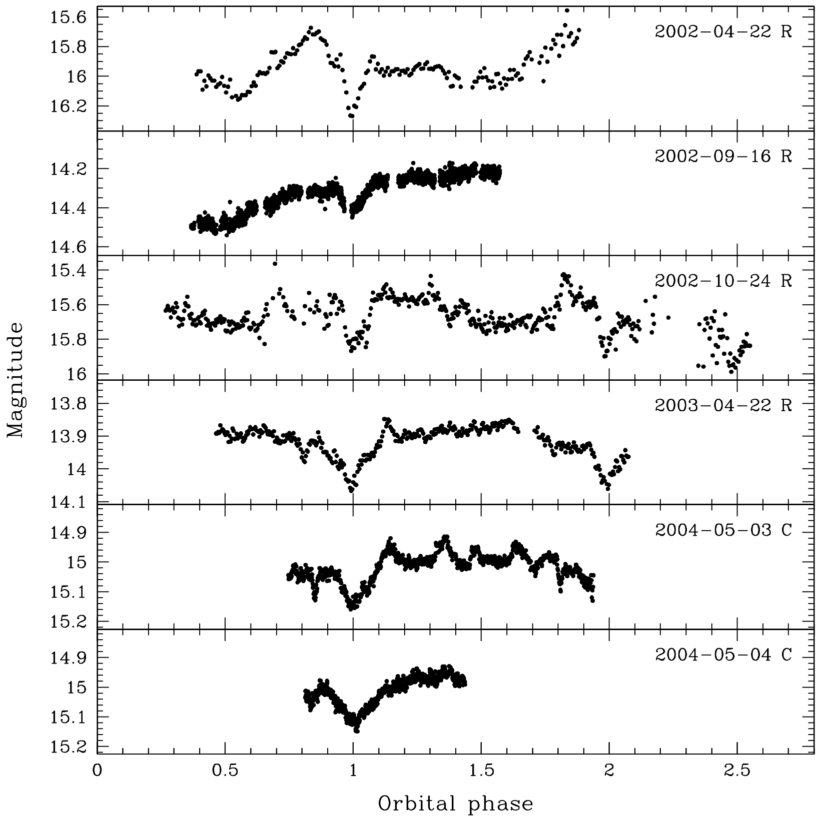

Figure 5.9: Sample *R*-band and filterless light curves of HS 1857+7127 folded over the ephemeris in Equation 5.1. See Section 5.5.2 for details.

the light curves of the system (Figure 5.9).

5.5.1 Long term variability

Throughout our photometric observing runs in April 2002 to May 2004, at the AIP, Kryoneri, Calar Alto 2.2 m, INT, OGS, IAC80, and FLWO telescopes, HS 1857+7127 was found to vary over a relatively large range between 17.2 – 13.9 mag in average brightness, suggesting a frequent outburst activity (Figure 5.9); the USNO-A2.0 catalogue listed $R = 15.0$ and $B = 15.6$. Combined with the long-orbital period (see below), it appears likely that HS 1857+7127 is a Z Cam-type dwarf nova. The IDS spectra obtained in April 2003 showed the system with a broad absorption trough around Hβ, with a weak (EW ~ 3.5 Å) single-peaked emission core,

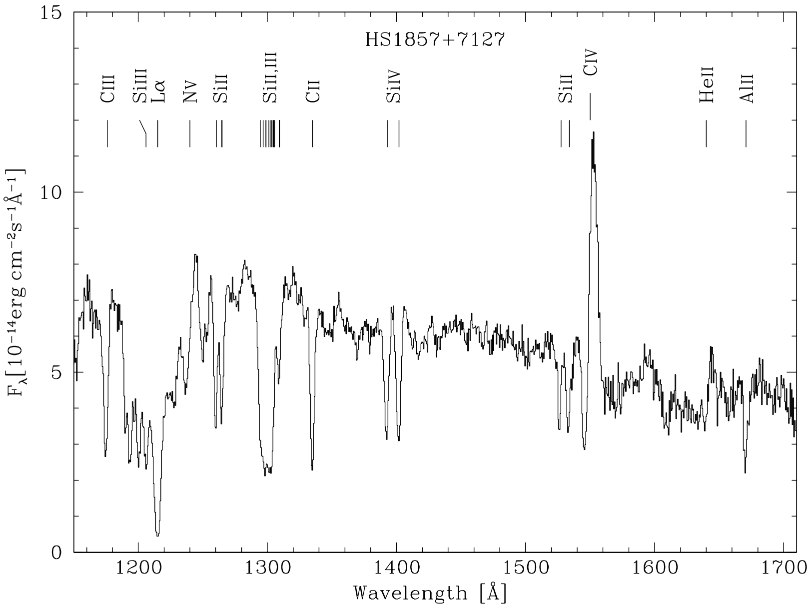

Figure 5.10: The HST/STIS spectrum of HS 1857+7127 taken on August 17, 2003 during an outburst.

typical of dwarf novae during outburst (Hessman et al. 1984). As we did not obtain a spectrophotometric flux standard on that occasion, and have no simultaneous photometric data, the magnitude of that outburst could not be determined. An additional outburst spectrum was obtained in the ultraviolet using HST/STIS on August 17, 2003, showing a range of low and high ionisation lines of C, N, Si, and Al in absorption, as well as a P-Cygni profile in C IV λ1550 (Figure 5.10). We derived an *R*-band equivalent magnitude of 14.1 from the STIS acquisition image taken before the ultraviolet spectroscopy (see Araujo-Betancor et al. 2005b for details on the processing of STIS acquisition images), and ground-based photometry obtained at Kryoneri a few hours after the STIS observations found HS 1857+7127 at $V = 13.9$. The STIS spectrum resembles qualitatively the ultraviolet spectrum of Z Cam obtained during an outburst (Knigge et al. 1997). The P-Cygni profile provides evidence for the presence of a wind outflow during the outburst.

5.5.2 Eclipse ephemeris

We obtained light curves of HS 1857+7127 throughout the period 2002 and 2004 and covered nine eclipses. We measured the times of the eclipse minima, and determined the cycle count by fitting $(\phi_0^{\rm fit} - \phi_0^{\rm observed})^{-2}$, leaving the period as a free parameter (Figure 5.11). The following ephemeris was derived as:

$$T_0 = \mathrm{HJD}\,2452368.53243(98) + 0.189109(1) \times E \tag{5.1}$$

where T_0 is defined as the time of mid-eclipse. The errors (given in brackets) of the zero phase and period were determined from a least-squares fit to the observed eclipse times versus the cycle count number. We conclude that the orbital period of HS 1857+7127 is $P_{\rm orb} = 272.317 \pm 0.001$ min.

The overall shape of the light curves and that of the eclipse profiles show a large degree of variability (Figure 5.9). On April 22, 2002, the light curve shows an orbital modulation with a bright hump preceding the eclipse, typically observed in quiescent eclipsing dwarf novae (e.g. Zhang & Robinson 1987), produced by the bright spot. A shallow (~ 0.4 mag) eclipse is recorded, implying a partial eclipse of the accretion disc in the system. On September 16, 2002, the system was apparently caught on the rise to an outburst, with the eclipse depth reduced to ~ 0.2 mag. During several intermediate and bright states, the signature of the bright spot disappeared, and was replaced by a broad orbital modulation with maximum light near phase 0.5, superimposed on short time scale flickering (Figure 5.9, bottom four panels). On May 3, 2004, a narrow dip ($\Delta\phi \simeq 0.05$) centred at $\phi \simeq 0.85$ precedes the eclipse during both observed cycles. A similar feature, though of lower depth, has been observed on April 22, 2003.

5.5.3 Radial velocities

As for HS 1016+3412 and HS 1340+1524, we measured the Hα radial velocities of HS 1857+7127 using the double-Gaussian method with a separation of 1500 km s^{-1}

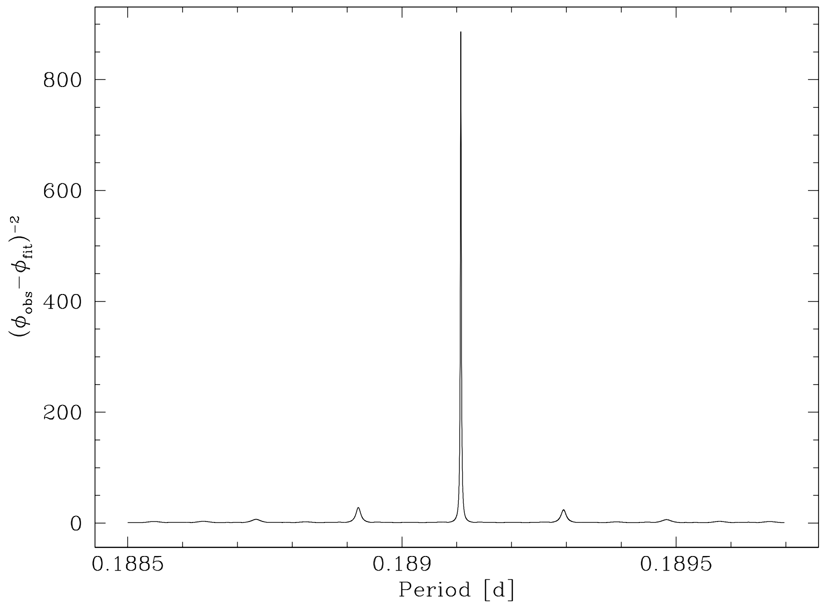

Figure 5.11: Periodogram of HS 1857+7127 computed from nine eclipses obtained during the 2002 to 2004 runs.

and an FWHM of 400 km s^{-1}. The Scargle periodogram computed from these data contains a set of narrow peaks at 3.3 d^{-1}, 4.3 d^{-1}, and 5.3 d^{-1}, consistent with the photometric frequency, $f \simeq 5.29\,\mathrm{d}^{-1}$, computed from the eclipse ephemeris in the previous section, and its one-day aliases (Figure 5.5, third panel). A periodogram calculated from a faked data set assuming the photometric frequency of 5.28796 d^{-1}, is shown in the insert in Figure 5.5 (third panel). We folded the Hα radial velocity curve using the eclipse ephemeris given in Equation 5.1, resulting in a quasi-sinusoidal modulation with an amplitude of $128.0 \pm 9.6\,\mathrm{km\,s^{-1}}$ and $\gamma = -17.9 \pm 7.4\,\mathrm{km\,s^{-1}}$, as determined from a sine-fit (Table 5.3). The red-to-blue crossing of the Hα radial velocities occurs at the photometric phase ~ 0.1 (Figure 5.6, third panel). Such a shift is not too much of a surprise, as our radial velocity measurements were extracted from spectra sampling different brightness (outburst) states of HS 1857+7127, covering less than one orbital cycle in all cases, and are not expected to represent a uniform and symmetrical emission from the accretion disc.

Table 5.4: The times of eclipse minima of HS 1857+7127 obtained during the 2002 to 2004 runs .

Date	Eclipse minima (HJD)
2002 Apr 03	2452368.53446
2002 Apr 22	2452387.44260
2002 Sep 16	2452534.38100
2002 Oct 24	2452572.39500, 2452572.57893
2003 Apr 22	2452752.42275, 2452752.61229
2004 May 03	2453128.56222
2004 May 04	2453129.88816

5.6 HS 2214+2845

HS 2214+2845 was first spectroscopically observed in September 2000 at the Calar Alto 2.2 m telescope. The identification spectrum suggests that the system is a typical non-magnetic CV observed during low mass-transfer activity. Time-resolved spectroscopy of HS 2214+2845 (41 spectra) was obtained in September 2000 and in August/September 2002 at the Calar Alto 2.2 m telescope and the INT, respectively. The CAFOS average spectrum of HS 2214+2845 (Figure 5.1) is characterised by a fairly red continuum superimposed by strong Balmer emission lines and weaker emission lines of He I, and Fe II; these emission lines are also observed in the IDS spectra which cover a narrower wavelength range, $\sim 4400 - 6800$ Å. The Balmer line profiles are double-peaked with a peak-to-peak separation of $\sim$ $800 - 1000\,\mathrm{km\,s^{-1}}$, suggesting an origin in an accretion disc (Horne & Marsh 1986). TiO absorption bands are present in the red part of the spectrum, revealing the late-type secondary star.

Time-resolved photometry of HS 2214+2845 was carried out at the Braeside, Kryoneri, OGS, and IAC80 telescopes during 2000 and 2003. Overall, the light curves display low amplitude flickering of $\sim 0.2 - 0.3$ mag with a short-time scale of $\sim 10 - 20$ min, superimposed on a low amplitude orbital modulation. A

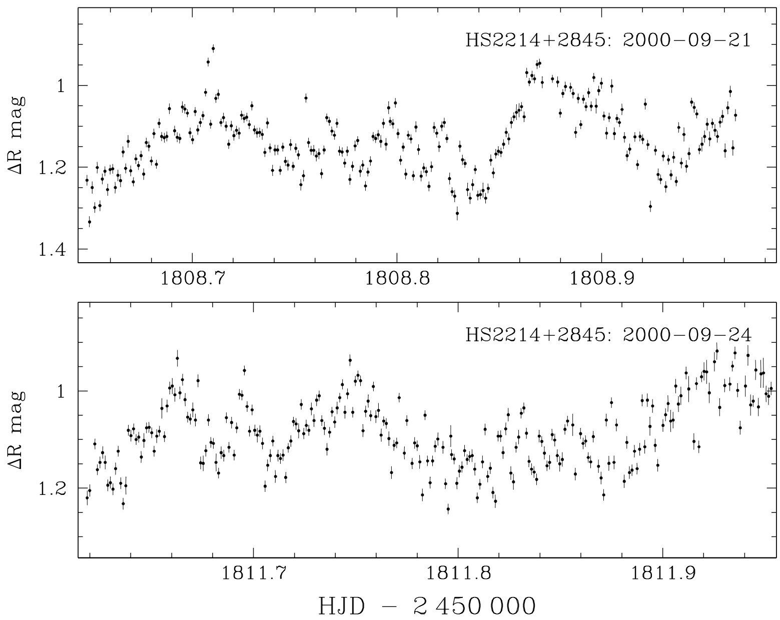

Figure 5.12: Sample *R*-band light curves of HS 2214+2845 obtained at the Braeside observatory.

double-humped structure with a period of ~ 4 h was detected in the two longest light curves obtained at the Braeside observatory in September 2000 (Figure 5.12) which were used as a crucial clue in determining the orbital period of HS 2214+2845 (see Section 5.6.2).

During our spectroscopic and photometric follow-up studies, HS 2214+2845 was consistently found at $\sim 16.5 - 15.5$ mag, with night-to-night variations of the mean magnitude of $\sim 0.2 - 0.4$ mag; the USNO-A2.0 catalogue listed $R = 15.0$ and $B = 15.6$. The dwarf nova nature of HS 2214+2845 was confirmed through the visual monitoring by P. Schmeer, which led to the detection of outbursts on December 10, 2004, and on May 2, July 14, September 22, 2005, and April 23, 2006. The mean cycle length appears to be ~ 71 d, and the maximum brightness recorded during outburst was $V \simeq 12.3$.

5.6.1 The spectral type of the secondary and distance

Overall, the spectrum of HS 2214+2845 resembles that of the U Gem-type dwarf novae, e.g. CZ Ori (Ringwald et al. 1994), PG 0935+075 (Thorstensen & Taylor 2001), and U Gem itself (Wade 1979; Stauffer et al. 1979), which have secondary stars with spectral types in the range M2–M4, and orbital periods in the range 255–315 min.

In order to determine the spectral type of the secondary star in HS 2214+2845, we used a library of spectral templates created from Sloan Digital Sky Survey data, covering spectral types M0–M9 (Rebassa-Mansergas et al. 2007). For each spectral type, we varied the flux contribution of the M-dwarf template until the molecular absorption bands cancelled out as much as possible in the difference spectrum of HS 2214+2845 minus template. The best match in the relative strength of the TiO absorption bands is achieved for a spectral type M2.5 $\pm$ 0.5, contributing 25% of the observed V-band flux of HS 2214+2845 (Figure 5.13). The extrapolated JHK_s fluxes spectrum of the secondary star[1] agrees fairly well with the 2MASS JHK_s fluxes of HS 2214+2845 (14.5, 13.9, and 13.5, respectively), suggesting that the accretion disc contributes only a small amount to the infrared flux.

Using Beuermann & Weichhold's (1999) calibration of the surface brightness in the 7165/7500 Å TiO band, and assuming a radius of $R_2 = (3.0 \pm 0.3) \times 10^{10}$ cm, based on the orbital period determined below and various radius-orbital period relations (e.g. Warner 1995; Beuermann & Weichhold 1999), we estimate the distance of HS 2214+2845 to be $d = 390 \pm 40$ pc, where the error is dominated by the uncertainty of the secondary's radius.

[1] Using LHS399 from Sandy Leggett's library of M-dwarf spectra, http://ftp.jach.hawaii.edu/ukirt/skl/dM.spectra/

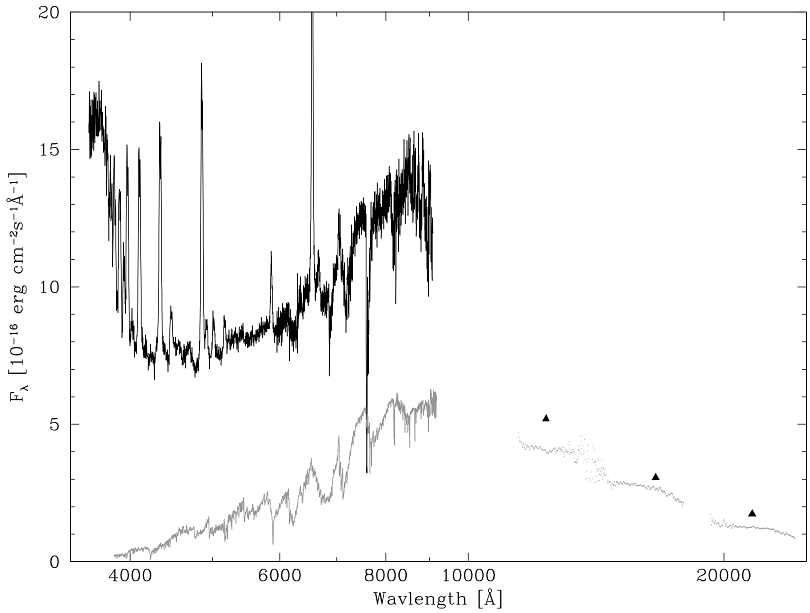

Figure 5.13: The average CAFOS spectrum of HS 2214+2845 (black line) along with the best-matching M-dwarf template of spectral type M2.5, scaled to fit the strength of the molecular bands in HS 2214+2845. The 2MASS JHK_s infrared fluxes of HS 2214+2845 are represented by filled triangles, the JHK_s spectrum of the M-dwarf template is shown as gray dots.

5.6.2 The orbital period

We first measured the radial velocity variation of Hα in the IDS spectra and in the R-100 CAFOS spectra, as well as that of Hβ in the B-100 CAFOS spectra by using the double Gaussian method of Schneider & Young (1980). The Scargle periodogram calculated from these measurements contained a peak near $\sim 5.5\,\mathrm{d}^{-1}$, but was overall of poor quality. In a second attempt, we determined the Hα and Hβ radial velocities by means of the V/R ratios, calculated from having equal fluxes in the blue and red line wing, fixing the width of the line to $\sim 2500\,\mathrm{km\,s}^{-1}$ in order to avoid contamination by the He I λ6678 line adjacent to Hα. The Scargle periodogram calculated from these sets of radial velocities contains the strongest signal at $6.6\,\mathrm{d}^{-1}$ and a $1\,\mathrm{d}^{-1}$ alias of similar strength at $5.6\,\mathrm{d}^{-1}$ (see Figure 5.5, bottom panel). Based on the spectroscopy alone, an unambiguous period determination is not possible.

A crucial clue in determining the orbital period of HS 2214+2845 came from the analysis of the two longest photometric time series obtained at the Braeside Observatory in September 2000 (Figure 5.12). These light curves display a double-humped structure with a period of ~ 4 h, superimposed by relatively low-amplitude flickering. The analysis-of-variance periodogram (AOV, Schwarzenberg-Czerny 1989) calculated from these two light curves contains two clusters of signals in the range of $4-7\,\mathrm{d}^{-1}$and $10-13\,\mathrm{d}^{-1}$, respectively (see Figure 5.14). The strongest peaks in the first cluster are found at $\simeq 5.58\,\mathrm{d}^{-1}$and $\simeq 5.92\,\mathrm{d}^{-1}$ and at $\simeq 11.14\,\mathrm{d}^{-1}$and $\simeq 11.48\,\mathrm{d}^{-1}$ in the second cluster. Based on the fact that two of the frequencies are commensurate, we identify $f_1 = 5.58\,\mathrm{d}^{-1}$ and $f_2 = 11.14\,\mathrm{d}^{-1}$ as the correct frequencies, with f_1 being the fundamental and f_2 being its harmonic. The periodogram of a faked data set computed from a sine wave with a frequency of $5.58\,\mathrm{d}^{-1}$, evaluated at the times of the observations and offset by the randomised observational errors reproduces the alias structure observed in the periodogram of the data over the range $4-7\,\mathrm{d}^{-1}$ very well (Figure 5.14, top panel). A two-frequency sine fit with $f_2 = 2 \times f_1$ to the data results in $f_1 = 5.581(12)\,\mathrm{d}^{-1}$. The Braeside photometry folded over that frequency displays a double-hump structure (Figure 5.15, two bottom panels). We identify f_1 as the orbital frequency of the system, hence, $P_{\mathrm{orb}} = 258.02 \pm 0.56$ min based on the following arguments. (a) The fundamental frequency detected in the photometry coincides with that of the second-strongest peak in the periodogram determined from the Hα and Hβ V/R-ratio radial velocity measurements (Figure 5.5, bottom panel). (b) Double-humped orbital light curves are observed in a large number of short-period dwarf novae, e.g. WX Cet (Rogoziecki & Schwarzenberg-Czerny 2001), WZ Sge (Patterson 1998), RZ Leo, BC UMa, MM Hya, AO Oct, HV Vir (Patterson et al. 2003), HS 2331+3905 (Araujo-Betancor et al. 2005a), and HS 2219+1824 (Rodríguez-Gil et al. 2005a); the origin of these double-humps is not really understood, but most

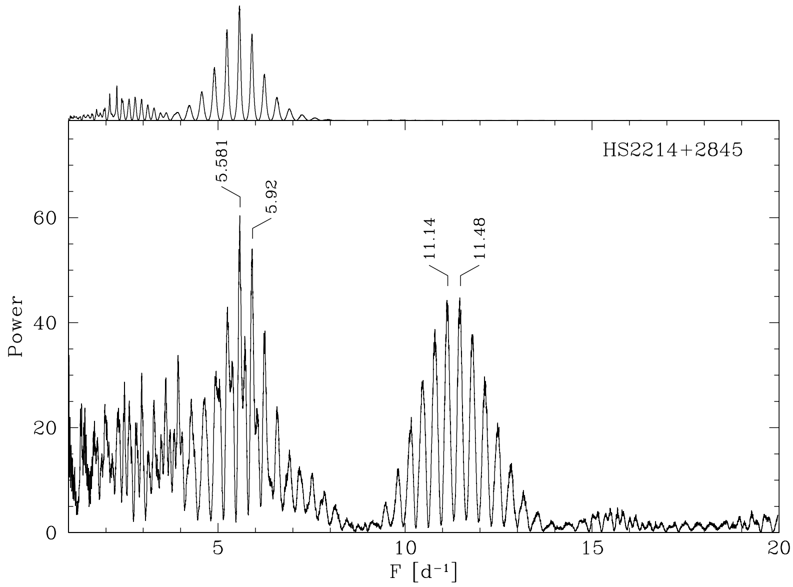

Figure 5.14: *Main panel*: the analysis-of-variance (AOV) periodogram of HS 2214+2845 calculated from the two longest light curves obtained at the Braeside Observatory, which show a double-humped pattern. *Top panel*: the AOV periodogram created from a sine wave with the orbital period of 258.02 min.

likely associated with the accretion disc/bright spot. In long-period dwarf novae, double-humped light curves are observed in the red part of the spectrum caused by ellipsoidal modulation of the secondary star, e.g. U Gem (Berriman et al. 1983) or IP Peg (Szkody & Mateo 1986; Martin et al. 1987). In both cases, a strong and sometimes dominant, signal at the harmonic of the orbital period is seen in the periodograms calculated from their light curves.

Figure 5.6 (bottom panel) shows the radial velocity data folded over the photometric orbital period (258.02 min), along with a sine-fit (Table 5.3). The radial velocities are shown again in Figure 5.15 together with the Braeside photometry, all folded using the photometric period but the spectroscopic zeropoint (Table 5.3). The photometric minima occur near orbital phase zero (inferior conjunction of the secondary) and 0.5, consistent with what is expected for ellipsoidal modulation. Very similar phasing is observed also for the double-humps in short-period systems, e.g.

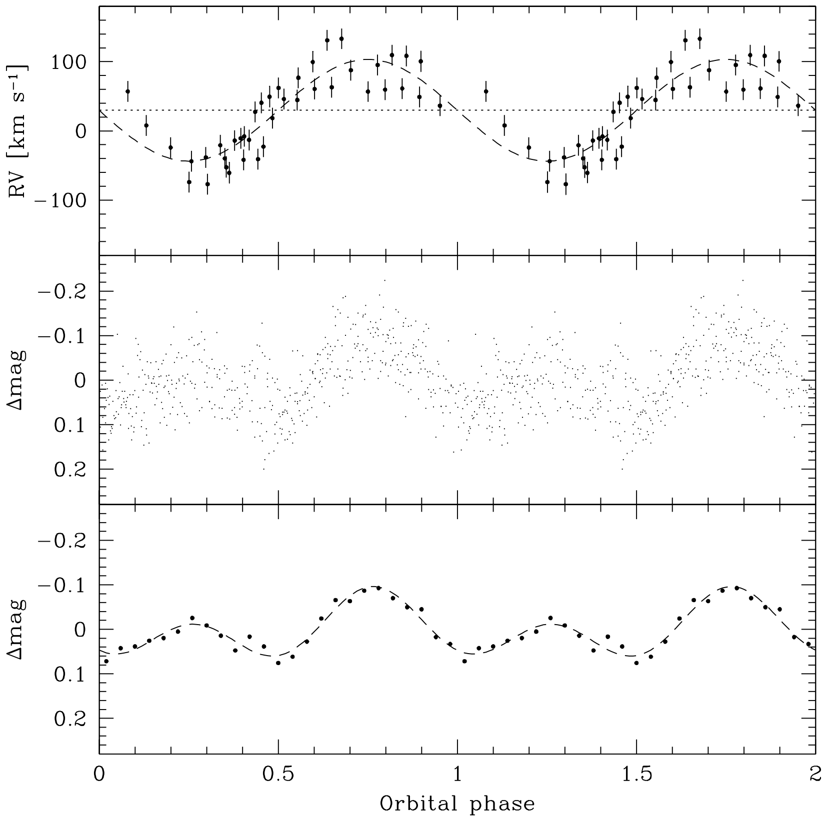

Figure 5.15: The spectroscopic and photometric data of HS 2214+2845 are folded on the photometric period of 258.02 min using the spectroscopic zero-point $T_0 =$ HJD 2451812.3309 defined by the red-to-blue crossing of the Hα and Hβ radial velocities. In that phase convention, the inferior conjunction of the secondary star is expected to be at orbital phase zero. *Top panel*: the radial velocity variation of the Hα and Hβ emission lines, as already shown in Figure 5.6. A whole cycle has been repeated for clarity. *Middle panel*: the photometric data obtained from the Braeside Observatory. *Bottom panel*: the photometric data binned into 25 phase slots, along with a two-frequency sine fit (dashed line).

WZ Sge (Patterson 1980) showing maximum brightness close to phases 0.25 and 0.75. However, given the strong contribution of the secondary star to optical flux of HS 2214+2845 (Figure 5.13), and the fact that the filterless Braeside photometry is rather sensitive in the red, we believe that the origin of the double-hump pattern seen in HS 2214+2845 is indeed ellipsoidal modulation.

The binary parameters of HS 2214+2845 could be improved in a future study by a measurement of the radial velocity of the secondary star, e.g. using the sodium doublet in the I band, and a determination of the orbital inclination from modelling the ellipsoidal modulation.

5.7 The new dwarf novae as X-ray sources

All five dwarf novae identified on the basis of their emission line spectra in the HQS are also X-ray sources in the ROSAT All Sky Survey (RASS): HS 0417+7445, HS 1340+1524, and HS 2214+2845 are contained in the Bright Source Catalogue (Voges et al. 1999), HS 1016+3412 and HS 1857+7127 within the Faint Source Catalogue (Voges et al. 2000). The X-ray properties of the new systems are summarised in Table 5.1. All but HS 1340+1524 are hard X-ray sources in the hardness ratio HR1, typical of non- (or weakly-) magnetic CVs (van Teeseling et al. 1996).

5.8 Discussion, part II

5.8.1 The orbital period distribution of dwarf novae

Because of their outbursts, the vast majority of all currently known dwarf novae have been discovered by variability surveys, either through professional sky patrols, or through the concentrated efforts of a large number of amateur astronomers (Gänsicke 2005). Considering the irregular temporal sampling of such observations, the population of known dwarf novae is likely to be biased towards systems which have frequent and/or large amplitude outbursts.

The orbital period distribution of all known dwarf novae

Inspecting the Ritter & Kolb catalogue (2003, Edition 7.5 of July 1, 2005) within the orbital period range of ~ 1 h to ~ 1 d and removing AM CVn systems, it is found that nearly half of all known CVs (262 systems out of 572, or 46%) are dwarf novae of which 166 (63%) have $P_{\rm orb} < 2$ h, 26 (10%) are found in the $2-3$ h orbital period gap, and 70 (27%) have long periods, $P_{\rm orb} > 3$ h. The conventional definition of the period gap as being the range $2-3$ h is somewhat arbitrary, and these numbers vary slightly if a different definition is used, but without changing the overall picture. Figure 5.16 (top panel) shows the orbital period distribution of all known CVs and dwarf novae with periods between ~ 1 h and ~ 1 d. Whereas the total population of all CVs features the well-known period gap, i.e. the relatively small number of CVs with periods $2\,{\rm h} < P_{\rm orb} < 3$ h, the number of dwarf novae reaches a minimum in the range $3-4$ h. In fact, the number of dwarf novae with $3\,{\rm h} < P_{\rm orb} < 4$ h is a half (15, or 6% of all dwarf novae) of that in the "standard" $2-3$ h period gap (26, or 10%). The dearth of known dwarf novae in the $3-4$ h period range was pointed out by Shafter et al. (1986) and Shafter (1992), who compared the observed dwarf nova period distribution with those constructed from various magnetic braking models, and concluded that none of the standard magnetic braking models can satisfactorily explain the lack of observed dwarf novae in the $3-4$ h period range.

The bottom panel of Figure 5.16 displays all known dwarf novae according to their subtypes, which are 159 (61%) SU UMa, 37 (14%) U Gem, 18 (7%) Z Cam, and 48 (18%) unclassified subtype (XX). For completeness, we note that the SU UMa class includes 8 ER UMa stars (which have very short superoutburst cycles) and 19 WZ Sge stars (which have extremely long outburst cycles). All confirmed U Gem and Z Cam stars lie above the period gap; in fact all but one Z Cam star (BX Pup) have $P_{\rm orb} > 3.5$ h[2]. It is clearly seen that the majority (85%) of SU UMa lie below the period gap and only a small fraction (15%) inhabits the $2-3$ h period range[3].

[2]Ritter & Kolb (2003) list five U Gem-type dwarf novae with $P_{\rm orb} < 3$ h: CC Cnc is a SU UMa-type dwarf nova (Kato & Nogami 1997), and we included 587 Lyr, CF Gru, V544 Her, and FS Aur as dwarf novae with no subtype (XX) due to the lack of clear observational evidence for a specific subtype.

[3]A note of caution among the WZ Sge stars, which mostly have ultrashort-periods, concerns UZ Boo. Ritter & Kolb (2003) list a period of ~ 3 h based on quiescent photometry, which is almost certainly wrong. Intensive time-series of the 2003 outburst of UZ Boo revealed a superhump period

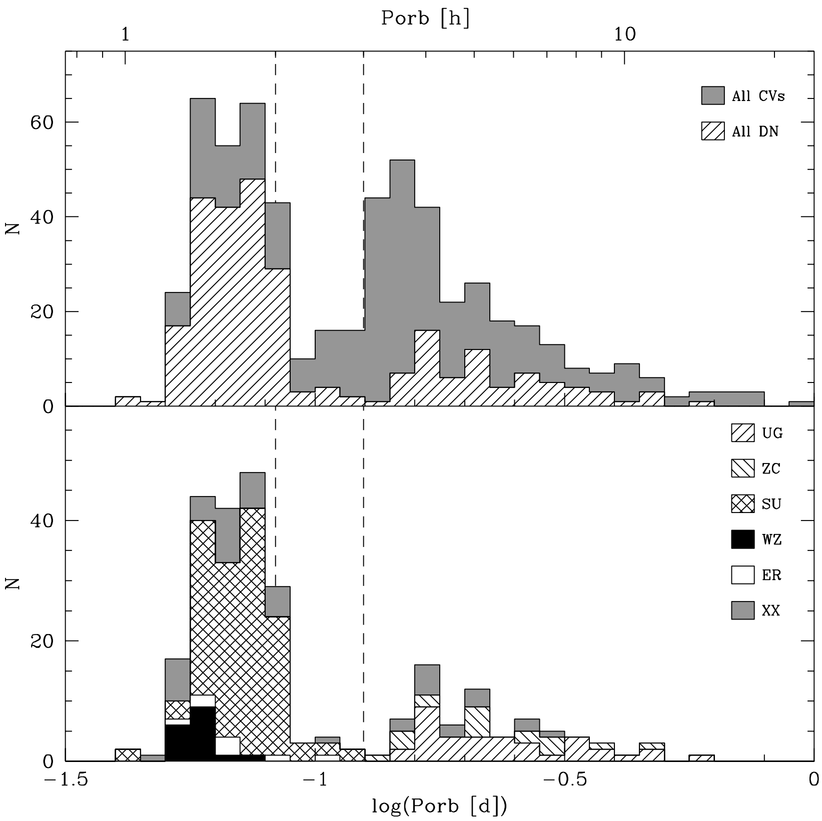

Figure 5.16: *Top panel*: the orbital period distribution of known CVs and dwarf novae from Ritter & Kolb (2003, 7th Edition, rev. 7.5, July 2005) are shown in gray and shaded, respectively. *Bottom panel*: the period distribution of known dwarf novae according to their subtypes, U Gem (UG), Z Cam (ZC), SU UMa (SU), WZ Sge (WZ), ER UMa (ER), and unclassified subtype (XX). The dashed lines represent the conventional 2–3 h period gap.

The orbital period distribution of short-period dwarf novae in Figure 5.16 (the majority of all CVs in this period range) differs markedly from the predictions made by the standard CV evolution theory (e.g. Kolb 1993; Kolb & Baraffe 1999; Howell et al. 2001): the minimum period is close to ~ 77 min, contrasting with the predicted minimum period of ~ 65 min (Paczyński & Sienkiewicz 1983), and the distribution of systems is nearly flat in $P_{\rm orb}$, whereas the theory predicts a substantial accumulation of systems at the minimum period. Several modifications of the CV

of 89.3 min (Kato, vsnet-campaign-dn 4064), and we use here this value as an estimate of the orbital period.

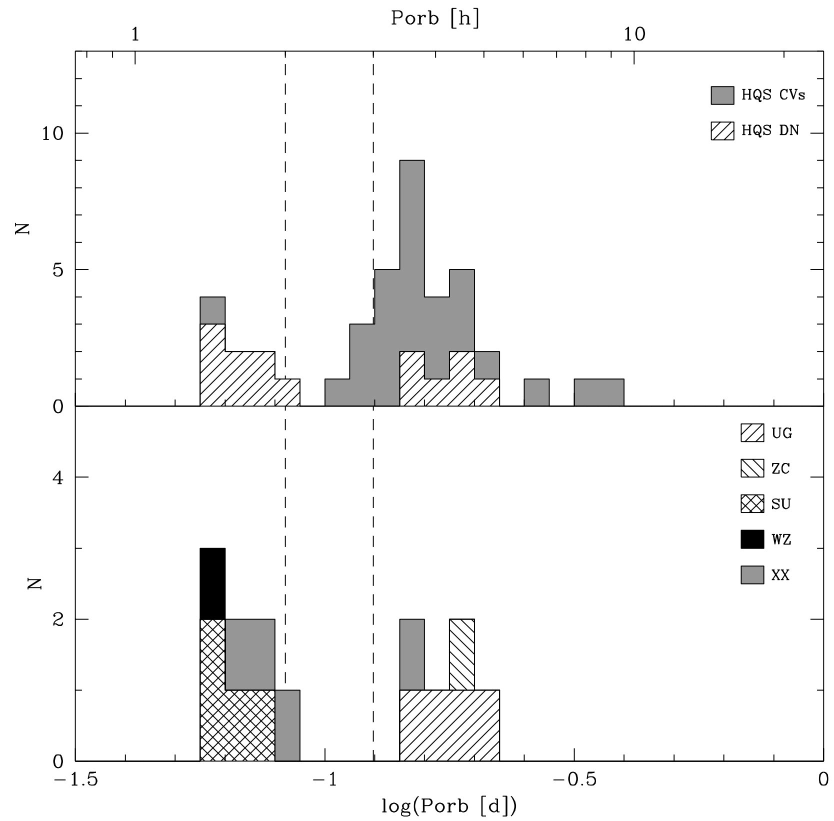

Figure 5.17: *Top panel*: the orbital period distribution of 41 new CVs and 14 dwarf novae identified in HQS are shown in gray and hatched, respectively. *Bottom panel*: the period distribution of HQS dwarf novae according to their subtypes, U Gem (UG), Z Cam (ZC), SU UMa (SU), WZ Sge (WZ), and unclassified subtype (XX). The dashed lines are the conventional 2–3 h period gap.

evolution theory have been suggested to resolve this discrepancy, however, none with indisputable success (King et al. 2002; Renvoizé et al. 2002; Barker & Kolb 2003).

The orbital period distribution of dwarf novae in the HQS

Another possible explanation for the lack of a spike in the orbital period distribution of CVs near the minimum period is that systems close to the minimum period, especially those evolving back to longer periods, have not yet been discovered due to observational selection effects. As most CVs below the period gap are dwarf novae, the most obvious bias suppressing the period spike is to assume that dwarf novae close to the minimum period have very rare outbursts. In fact, a number of dwarf novae near the minimum period have very long outburst intervals, e.g. WZ Sge ($P_{\rm orb} = 81.6$ min, Patterson et al. 2002) erupts every $20-30$ years; GW Lib ($P_{\rm orb} = 76.8$ min, Thorstensen et al. 2002) has been seen in outburst only once, in 1983, although a second outburst was detected at the time of writing in April 2007. It cannot be excluded that these systems represent "the tip of the iceberg" of a dwarf nova population with even longer outburst periods. Assuming that rarely outbursting dwarf novae do exist in a significant number, and that they spectroscopically resemble the known objects, such as WZ Sge or GW Lib, our search for CVs in the HQS should be able to identify them (Gänsicke et al. 2002b).

We have so far obtained orbital periods for 41 new CVs found in the HQS; their period distribution is shown in Figure 5.17 (top panel). The first thing to notice is that the majority of the new CVs identified in the HQS are found *above* the period gap, with a large number of systems in the period range $3-4$ h (see Chapter 4 for a discussion of the properties of CVs in this period range). As for the overall CV population, a dearth of systems is observed in the $2-3$ h period range (Figure 5.17, top panel), with the gap being wider for dwarf novae (Figure 5.17, bottom panel).

To date 14 (26%) out of 53 new CVs discovered in the HQS have been classified as dwarf novae, including the five systems, HS 0417+7445, HS 1016+3412, HS 1340+1524, HS 1857+7127, and HS 2214+2845, presented in this chapter (Table 5.5). The fraction of long-period ($P_{\rm orb} > 3$ h) systems is larger in the HQS sample (43%) than in the total population of known dwarf novae (27%, see Section 5.8.1). The total number of new HQS dwarf novae is relatively small, and subject to corresponding statistical uncertainties. However, the tilt towards long-period dwarf novae among the new HQS CVs is likely to be underestimated, as a significant number of long-period HQS CVs have still uncertain CV subtypes, and several of them could turn out to be additional a Z Cam-type dwarf nova (e.g.

HS 0139+0559, HS 0229+8016, HS 0642+5049, plus additional yet unpublished systems). Optical monitoring of the long-term variability of these systems will be necessary to unambiguously determine their CV type. Overall, the dwarf novae identified within the HQS fulfil the above expectations of being "low-activity" systems, i.e. dwarf novae that have either infrequent outbursts (e.g. KV Dra, HS 0941+0411, HS 2219+1824) or low-amplitude outbursts (e.g. EX Dra). We found only one system that resembles the WZ Sge stars with their very long outburst intervals found near the minimum period that is HS 2331+3905 (Araujo-Betancor et al. 2005a) which has a period of 81.1 min, and no outburst has been detected so far.

Thus, our search for CVs in the HQS has been unsuccessful in identifying the predicted large number of short-period CVs, despite having a very high efficiency in picking up systems that resemble the typical known short-period dwarf novae.

5.8.2 Constraints on the space density of CVs

CV population models result in space densities in the range $2 \times 10^{-5}\,\mathrm{pc}^{-3}$ to $2 \times 10^{-4}\,\mathrm{pc}^{-3}$ (de Kool 1992; Politano 1996), whereas the space density determined from observations is $(0.5-1) \times 10^{-5}\,\mathrm{pc}^{-3}$ (Patterson 1984; Ringwald 1996; Patterson 1998). It appears therefore that we currently know about an order of magnitude fewer CVs than predicted by the models. Also the observed ratio of short to long orbital period systems is in strong disagreement with the predictions of the theory. Patterson (1984, 1998) estimated that the fraction of short-period CVs per volume is $75-80\%$, which has to be compared to 99% in the population studies (Kolb 1993; Howell et al. 1997).

Because of the large differences in mass-transfer rates, and hence absolute magnitudes of long ($P_{\mathrm{orb}} > 3\,\mathrm{h}$) and short ($P_{\mathrm{orb}} < 3\,\mathrm{h}$) period CVs, a proper discussion of CV space densities seems dishearteningly difficult. However, taking the

Table 5.5: Dwarf novae discovered in the HQS with their subtypes, U Gem (UG), SU UMa (SU), Z Cam (ZC), and unclassified (XX). Uncertain classifications are marked by a colon.

HQS ID	Other name	$P_{\rm orb}$ (min)	Type	References
HS 2331+3905		81.1	WZ:	1
HS 1449+6415	KV Dra	84.9	SU	2,3
HS 2219+1824		86.2	SU	4
HS 1340+1524		92.7	XX	this work
HS 1017+5319	KS UMa	97.9	SU	2,5
HS 0417+7445		105.1/109.9	SU	this work
HS 1016+3412		114.3	XX	this work
HS 0913+0913	GZ Cnc	127.1	XX	2,7,8
HS 0941+0411	RX J0944.5+0357	215.0	XX	2,9
HS 0552+6753	LU Cam	216.6	UG	2,6
HS 0907+1902	GY Cnc	252.6	UG	2,10,11
HS 2214+2845		258.0	UG	this work
HS 1857+7127		272.3	ZC:	this work
HS 1804+6753	EX Dra	302.3	UG	12,13,14

References: (1) Araujo-Betancor et al. (2005a); (2) Jiang et al. (2000); (3) Nogami et al. (2000); (4) Rodríguez-Gil et al. (2005a); (5) Patterson et al. (2003); (6) Thorstensen priv. com. & vsnet-campaign-dn 2681; (7) Kato et al. (2002a); (8) Tappert & Bianchini (2003); (9) Mennickent et al. (2002); (10) Gänsicke et al. (2000); (11) Kato et al. (2002b); (12) Fiedler et al. (1997); (13) Billington et al. (1996); (14) Shafter & Holland (2003)

theoretical models at face value, the space density of long-period CVs is entirely negligible compared to that of short-period CVs (Kolb 1993; Howell et al. 1997), and hence a discussion of the total CV space density can be carried out on the basis of short-period systems alone. In the following, we assess the expected numbers of systems in the HQS separately for short-period CVs that are still evolving towards the minimum period (pre-bounce), and those that already reached the minimum period and are evolving back to longer periods (post-bounce). For both cases, we assumed (1) a space density of $5\times10^{-5}\,{\rm pc}^{-3}$ as an intermediate value between the predictions of de Kool (1992) and Politano (1996), (2) that 70% of all CVs are post-bounce systems, and 30% are pre-bounce systems (Kolb 1993; Howell et al. 1997) (ignoring, as stated above, the small number of long-period CVs), (3) a galactic disc scale height of 150 pc (e.g. Patterson 1984), and (4) that the luminosity of short-period CVs is dominated by the accretion-heated white dwarf.

Pre-bounce CVs expected in the HQS

CV evolution models predict a typical accretion rate of $\dot{M} \simeq 5 \times 10^{-11} M_{\odot}\,\mathrm{yr}^{-1}$ for pre-bounce systems, with a relatively small spread (Kolb 1993; Howell et al. 1997). For this accretion rate, Townsley & Bildsten's (2003) calculation of white dwarf accretion heating predicts an effective temperature of $T_{\mathrm{wd}} \simeq 12\,000$ K. If the luminosity is dominated by a white dwarf of this temperature, the HQS with an average magnitude limit of $B \simeq 18$ would detect pre-bounce CVs out to a distance of 175 pc (using the absolute magnitudes of white dwarfs by Bergeron et al. 1995), i.e. over a bit more than one scale height. Within a sphere of radius 175 pc around the Earth, one would expect $\simeq 144$ CVs (taking into account the exponential drop-off of systems perpendicular to the plane), of which $\simeq 36$ would be within the sky area sampled by the HQS. This is a conservative lower limit, as any additional luminosity from the accretion disc and/or bright spot as well as a hotter white dwarf temperature would increase the volume sampled by the HQS, and therefore increase the number of pre-bounce CVs within the survey.

Post-bounce CVs expected in the HQS

Once past the minimum period, the accretion rate of CVs substantially drops as a function of time, and we assume here a value of $\dot{M} = 10^{-11} M_{\odot}\,\mathrm{yr}^{-1}$, corresponding to an intermediate CV age of ~ 5 Gyr (Kolb & Baraffe 1999), and a white dwarf temperature of $T_{\mathrm{wd}} \simeq 7000$ K (Townsley & Bildsten 2003). This lower white dwarf temperature reduces the detection limit of the HQS to only $\simeq 65$ pc. The total number of post-bounce CVs within a sphere of radius 65 pc around the Earth is hence expected to be 40, of which 10 are within the HQS area.

Short-period CVs in the HQS: most likely pre-bounce only

The immediate question is *what type are the short-period HQS CVs: pre- or post-bounce?* As mentioned in Section 5.8.1, only 12 short-period ($P_{\rm orb} < 3$ h) systems have been found among the 41 new HQS CVs for which we have adequate follow-up data. The new short-period CVs comprise eight dwarf novae (Table 5.5), two polars (Reimers et al. 1999; Jiang et al. 2000; Schwarz et al. 2001; Tovmassian et al. 2001; Thorstensen & Fenton 2002; Gänsicke et al. 2004b), one intermediate polar (Rodríguez-Gil et al. 2004a; Patterson et al. 2004), and one system with uncertain classification (Gänsicke et al. 2004a). The white dwarfs have been detected in spectra of HS 2237+8154 (Gänsicke et al. 2004a), HS 2331+3905 (Araujo-Betancor et al. 2005a), HS 2219+1824 (Rodríguez-Gil et al. 2005a), and HS 1552+2730 (Gänsicke et al. 2004b), with temperatures of $\simeq 10\,500$ K, $\simeq 11\,500$ K, $\simeq 15\,000$ K, and $\simeq 20\,000$ K, respectively. These four systems are very likely to have the lowest mass transfer rates among the 12 new short-period CVs; the optical spectra of the other eight are characterised by strong Balmer and He emission lines and the associated continuum which outshines the white dwarf, typical of higher accretion rates. While there are still about a dozen HQS CVs with no accurate orbital period determination, the data already at hand makes it very unlikely that more than two or three of those systems will turn out to have periods < 3 h.

For a complete assessment of the short-period content of the HQS, one has obviously to include in the statistics the short-period CVs that are contained within the HQS data base, but were already known – subject to the same selection criteria that were applied to identify the twelve new systems. Gänsicke et al. (2002b) analysed the properties of the previously known CVs within the HQS data base, and came to the following conclusions. 18 previously known short-period ($P_{\rm orb} < 3$ h) systems with HQS spectra are correctly (re-)identified as CVs, including 12 dwarf novae, five polars, and one intermediate polar[4]. The authors also found that only two previously known short-period systems with HQS spectra failed to be identified as CVs; this "hit rate" of 90% underlines the extreme efficiency of the HQS of finding short-period CVs. Five out of those 18 systems have measured white dwarf temperatures, all of them in the range $\simeq 11\,000 - 16\,000$ K (MR Ser, ST LMi, AR UMa, SW UMa, T Leo: Gänsicke et al. 2001; Hamilton & Sion 2004; Araujo-Betancor et al. 2005b; Gänsicke et al. 2005b). For the remaining 13 systems, all have spectra dominated by strong Balmer and He emission, suggesting accretion rates too high to detect the white dwarf.

In summary, the HQS contains a total of 30 short-period CVs (12 new identifications plus 18 previously known systems); all of which are consistent with being pre-bounce systems. At face value, this number agrees rather nicely with the 36 expected systems derived above, but one has to bear in mind that this number is an absolute lower limit, as hotter white dwarfs and/or accretion luminosity from the disc and hot spot will increase the volume sampled by the HQS.

While there may still be some shortfall of pre-bounce systems, it is much more worrying that so far no systems with the clear signature of a post-bounce CV that evolved significantly back to longer periods has been found – neither in the HQS, nor elsewhere. The coldest CV white dwarfs have been found, to our knowledge, in the polar EF Eri ($T_{\rm wd} \simeq 9500$ K, Beuermann et al. 2000), and HS 2331+3905 ($T_{\rm wd} \simeq 10\,500$ K, Araujo-Betancor et al. 2005a), both systems with the orbital periods of $\simeq 81$ min – which may hence be either pre- or post-bounce systems.

A final note concerns the number of WZ Sge stars, i.e. short-period dwarf novae with extremely long outburst intervals. Given the strong Balmer lines in the known WZ Sge stars e.g. WZ Sge itself (Gilliland et al. 1986), BW Scl (Abbott et al. 1997), GD 552 (Hessman & Hopp 1990), and GW Lib (Szkody et al. 2000;

[4]Excluding the double-degenerate helium CVs, which follow a different evolution channel that is not taken into account in the population models of de Kool (1992) and Politano (1996).

Thorstensen et al. 2002), we believe that any WZ Sge star brighter than $B \simeq 18$ would have easily been identified in the HQS – yet, only a single new WZ Sge system has been discovered, HS 2331+3905 (Araujo-Betancor et al. 2005a).

Thus, we conclude that while our systematic effort in identifying new CVs leads to a space density of pre-bounce short-period CVs which agrees with the predictions within an order of magnitude, the bulk of all CVs, which are predicted to past the minimum orbital period, remain unidentified so far.

5.9 Summary

We have identified five new dwarf novae as a part of our search for new CVs in the HQS, bringing the total number of HQS-discovered dwarf novae to 14. The new systems span orbital periods from ~ 1.5 h to nearly 5 h, confirming the trend that dwarf novae spectroscopically selected in the HQS display a larger ratio of long-to-short orbital periods. Overall, dwarf novae represent only about one third of the HQS CVs which are studied sufficiently well, and it is by now clear that the properties of the sample of new HQS CVs do not agree with those of the predicted large population of short-period low mass-transfer systems. Within the limiting magnitude of $B \simeq 17.5 - 18.5$, the HQS *does* however contain a large number of previously known dwarf novae that were identified because of their variability, and almost all of these systems have been recovered as strong CV candidates on the basis of their HQS spectrum (Gänsicke et al. 2002b). Based on their spectroscopic and photometric properties it appears that most, if not all, short-period CVs in the HQS (newly identified and previously known) are still evolving towards the minimum period. If the large number of post-bounce CVs evolving back to longer periods predicted by population models exists, they must (a) have very long outburst recurrence times, and (b) have Hβ equivalent widths that are far lower than observed in the currently known typical short-period CVs.

Chapter 6

A new hot and young pre-cataclysmic variable

6.1 Introduction

Post-common envelope binaries (PCEBs), i.e. detached white dwarf-main sequence binaries, originate from wide binaries comprising unequal main sequence components. Once the more massive star evolves through the giant phase and fills its Roche lobe, unstable mass transfer onto the unevolved star starts. The high accretion rate subsequently brings the system into a common envelope (CE) phase. Friction between the stellar components and the envelope shrinks the binary orbital separation and eventually ejects the envelope from the system, resulting in the majority of PCEBs having orbital periods of a few days (Willems & Kolb 2004). The binary separations of PCEBs are believed to be further reduced through angular momentum loss via magnetic braking and/or gravitational radiation. The main-sequence star will ultimately fill its Roche lobe and start mass transfer onto the white dwarf, which turns the binary into a CV. While this general scenario is widely accepted, the details of the evolution through the common envelope phase, as well as the subsequent orbital angular momentum loss are poorly understood. Consequently, predictions made by binary population models are rather uncertain.

As PCEBs are simple objects in terms of their stellar components, they offer a large potential in constraining and calibrating the physics of both CE evolution and orbital angular momentum loss. This has implications for a wide range of astronomical objects such as SN Ia progenitors, X-ray binaries, or neutron star binaries as likely progenitors of short gamma-ray bursts. However, until recently PCEBs received little observational attention, largely due to the lack of a dedicated search for such systems. Schreiber & Gänsicke (2003) analysed the properties of 30 well-studied PCEBs and showed that the known population of these systems is extremely biased towards young systems consisting of hot white dwarfs and late type companions, as the majority of the known PCEBs were initially selected as blue objects. A substantial improvement in the statistics of PCEB properties will be possible through the exploitation of large extragalactic surveys such as the Hamburg Quasar Survey (HQS, Hagen et al. 1995) or the Sloan Digital Sky Survey (SDSS, York et al. 2000).

In this chapter, I present a detailed follow-up study of the new PCEB HS 1857+5144, which has been discovered in our ongoing effort to identify CVs and pre-CVs in the HQS. The information on observations is available in Chapter 2. In Section 6.2, I describe the spectroscopic and photometric characteristics of the system. The orbital ephemeris of HS 1857+5144 as well as radial velocity and equivalent width are determined in Sections 6.3–6.4. In addition, phase relations between photometric and spectroscopic data are derived in Section 6.5. In Sections 6.6–6.7, I analyse the nature of the stellar components and discuss the future evolution of the system.

6.2 Spectroscopic and photometric characteristics

6.2.1 Spectroscopic characteristics

An identification spectrum of HS 1857+5144 was obtained in August 1992 at the Calar Alto 2.2 m telescope. The spectrum is characterised by a blue continuum superimposed by strong Balmer emission lines. Subsequent time-series, intermediate resolution spectroscopy of HS 1857+5144 was performed in July 2004 at the 2.7 m McDonald telescope covering ~ 10 h (35 spectra) in total. Four additional high resolution spectra were obtained at the WHT in July 2006, covering the orbital minimum, maximum, and the quadrature phases.

Figures 6.1 and 6.2 illustrate the orbital phase-dependent variation of the emission line profiles of HS 1857+5144 from the McDonald and WHT spectra, respectively. The emission lines greatly vary in strength over the orbital cycle, with maximum line fluxes occurring at $\varphi \simeq 0.5$ and disappearing around $\varphi \simeq 0.0$. The dominant lines detected in the McDonald spectra belong to the Balmer series, but the high quality of the WHT spectra reveals a multitude of narrow emission lines, e.g. the C III/N III λ4650 Bowen blend, Mg II, N II, O II/C III blend, and N III/Fe III blend. This emission-line spectrum is a characteristic of known PCEBs containing a cool secondary star irradiated by a very hot primary component, such as BE UMa (Ferguson et al. 1981; Ferguson & James 1994), EC 11575-1845 (Chen et al. 1995), and HS 1136+6644 (Sing et al. 2004). The strengths of the Balmer emission lines vary in phase with those of He I, C III/N III, indicating that all emission lines come from the same source. The WHT spectra also reveal that the Balmer emission lines have double-peaked profiles, with peak separations of $\sim 170\,\mathrm{km\,s^{-1}}$ for Hβ (Figure 6.2, small window) and $\sim 150\,\mathrm{km\,s^{-1}}$ for Hγ which are most likely caused by non-LTE effects in the strongly irradiated atmosphere of the companion star (Barman et al. 2004).

During the orbital faint phase, $\varphi \simeq 0.0$, weak absorption Balmer lines are

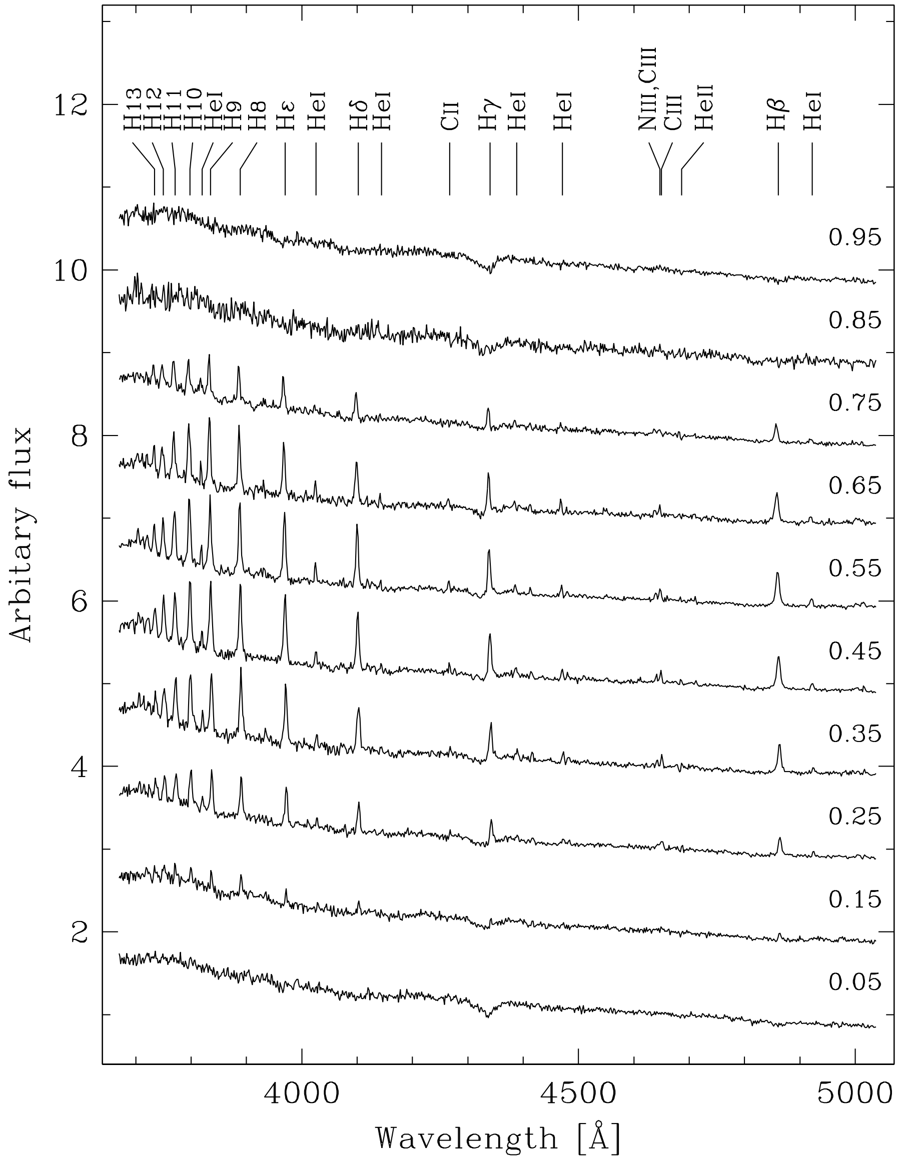

Figure 6.1: Phase-binned spectra of HS 1857+5144 obtained at McDonald Observatory. These spectra show a clear modulation of the emission line strengths with orbital phase.

observed in both sets of spectra, with the He II λ4686 absorption also detected in the WHT spectra. The detection of He II λ4686 classifies the primary star in HS 1857+5144 as a DAO white dwarf.

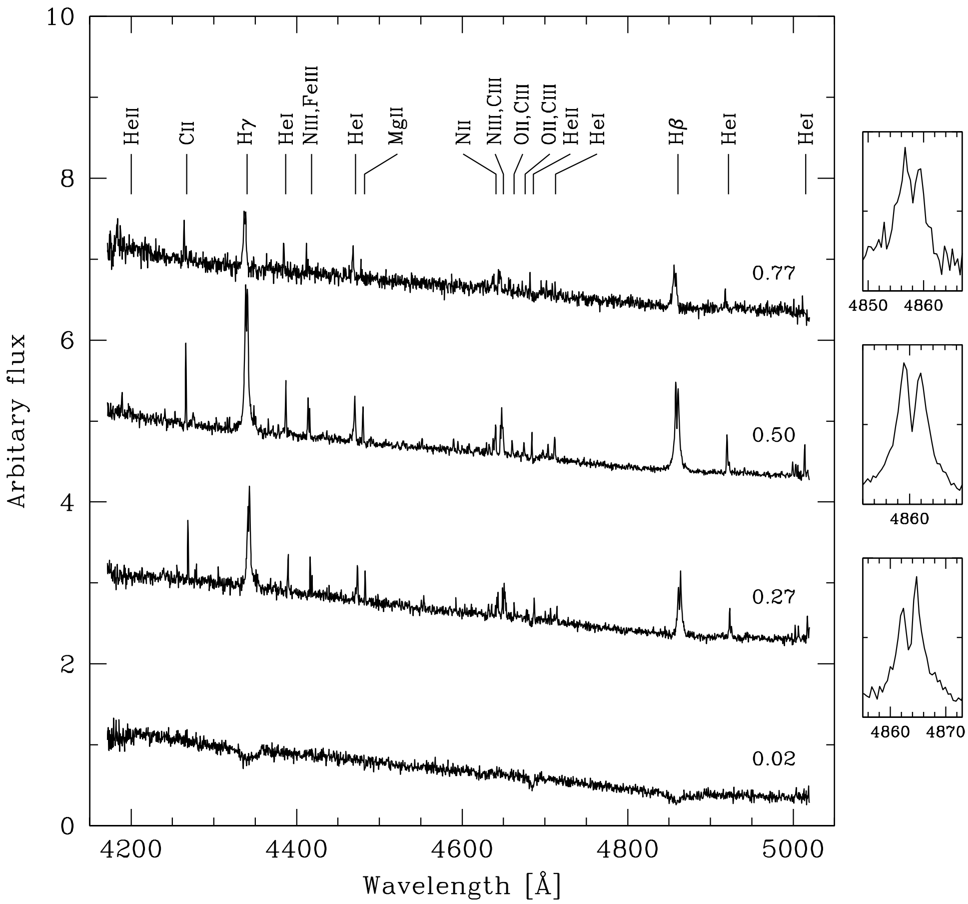

Figure 6.2: *Main panel*: high resolution spectra of HS 1857+5144 at different orbital phases from 0.02 – 0.77 obtained at the WHT. *Small windows*: close up of the evolution of the Hβ emission line profile in the orbital phase range 0.27 – 0.77 (from *bottom* to *top*).

6.2.2 Light curve morphology

We obtained a total of ~ 60 h of time-series CCD photometry of HS 1857+5144 during the period July 2003 to June 2006, using the IAC80, OGS, and Kryoneri telescopes. The light curves of HS 1857+5144 (Figure 6.3) display a smooth quasi-sinusoidal modulation with a period of $\simeq 6.4$ h and peak-to-peak amplitudes of 0.7 mag in the *B*-band, 1.1 mag in the *R*-band, and 0.9 mag in white light. The minimum in the *B*-band light curve is nearly flat for $\simeq 0.15$ orbital cycles, whereas the

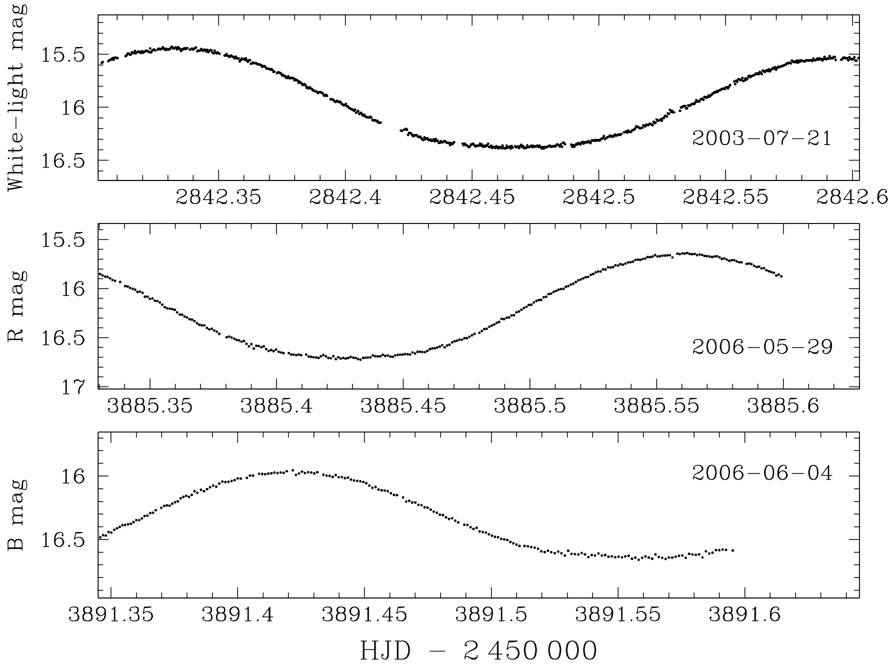

Figure 6.3: Filterless, R, and B (from *top* to *bottom*) sample light curves of HS 1857+5144 obtained with the 1.2 m telescope at Kryoneri Observatory.

shape of the minimum in the R-band is rounder. No sign of the typical short-period flickering of accreting systems is detected, which classifies HS 1857+5144 as a detached binary. The low-amplitude scatter seen in the light curves in Figure 6.3 is caused by residual flat-field structures and poor tracking of the Kryoneri telescope. The observed periodic brightness variation is characteristic of a large reflection effect on the heated face of the secondary star, irradiated by a hot primary star (e.g. TW Crv, Chen et al. 1995; KV Vel, Hilditch et al. 1996; and HS 2333+3927, Heber et al. 2004). Finally, HS 1857+5144 was found at a constant mean magnitude of $\simeq 16.2$ throughout our observing runs, consistent with USNO-A2.0 measurements of HS 1857+5144 ($R = 16.3$ and $B = 15.7$).

6.3 Orbital period and ephemeris

A qualitative inspection of the light curves presented in Section 6.2.2 provided an estimate of the orbital period of $\simeq 6.4$ h. In order to obtain a precise value, we shifted the magnitudes of each observing run so that their minima match that of the 2003 July 21 Kryoneri data, which covered an entire orbital cycle. We then subjected the combined 2003–2006 data to a time-series analysis within the `MIDAS/TSA` context using Schwarzenberg-Czerny's (1996) `ORT` method, a variation of the analysis-of-variance technique which fits orthogonal polynomials to the data folded over a set of trial periods. The `ORT` periodogram (Figure 6.4) contains an unambiguous peak at $3.755\,\mathrm{d}^{-1}$. A sine fit to the combined photometric data defined the following ephemeris:

$$T_0 = \mathrm{HJD}\,2452831.5475(17) + 0.26633357(8) \times E \ , \qquad (6.1)$$

where T_0 is defined as the time of inferior conjunction of the secondary star (= orbital minimum in the light curves). We conclude that the orbital period of HS 1857+5144 is $P_{\mathrm{orb}} = 383.5203 \pm 0.0001$ min. Figure 6.5 (bottom two panels) shows the Kryoneri B-band and R-band light curves folded according to the above ephemeris.

6.4 Radial velocities and equivalent widths

In order to spectroscopically confirm the orbital period of HS 1857+5144, we first measured radial velocity variations of the Hβ, Hγ, Hδ, Hε, and H10 emission lines separately by cross-correlating the observed line profiles with a single Gaussian with a FWHM of $250\,\mathrm{km\,s^{-1}}$ for Hβ and Hε, and of $300\,\mathrm{km\,s^{-1}}$ for Hγ, Hδ, and H10 within `MOLLY`. The `ORT` periodograms calculated from the radial velocities of the individual lines consistently favoured an orbital frequency of $\sim 3.75\,\mathrm{d}^{-1}$, in good agreement with the photometric result. The radial velocity amplitudes determined from the different Balmer lines varied in the range $\sim 175 - 215\,\mathrm{km\,s^{-1}}$.

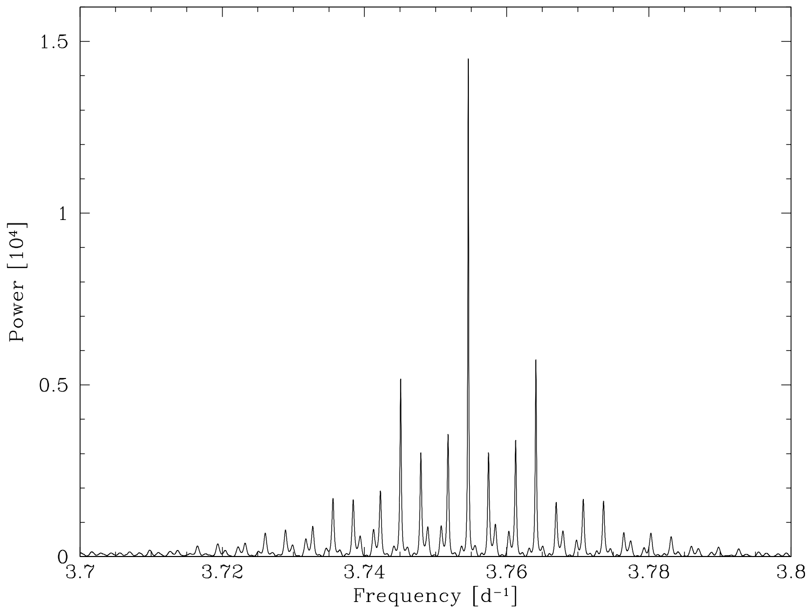

Figure 6.4: ORT periodogram of HS 1857+5144 computed from all photometric data.

In order to obtain a more robust measure of the radial velocity of the companion star in HS 1857+5144, we determined an average radial velocity of the Balmer lines by fitting simultaneously the Balmer series Hβ to H13 with a set of 10 Gaussians. The wavelengths of all Gaussians were fixed to their laboratory wavelengths relative to that of Hδ, and only the wavelength of Hδ, as well as the widths and amplitudes of all 10 Gaussians were used as free parameters. The average Balmer line radial velocities are listed in Table 6.1 and are shown in Figure 6.5 (top panel) folded over the ephemeris given in Equation 6.1. A sine fit to the folded velocities and their errors results in an amplitude of $K_{\rm em} = 185.2 \pm 4.9\,{\rm km\,s^{-1}}$ and $\gamma = -24.0 \pm 6.5\,{\rm km\,s^{-1}}$. Note that this velocity amplitude does not represent the radial velocity amplitude of the centre of mass of the secondary star, but that of the illuminated hemisphere. Since the centre of light is located closer to the centre of mass of the system than the centre of mass of the secondary star, the 'true' radial velocity amplitude of the secondary star should therefore be larger than the observed velocity amplitude, $K_{\rm em} = 185.2 \pm 4.9\,{\rm km\,s^{-1}}$. We will determine a K-correction in

Section 6.6.3.

We also analysed the variation of the equivalent width of the Hβ line (Table 6.1). The Scargle periodogram calculated from these measurements contained two equally significant signals at $3.409\,\mathrm{d}^{-1}$ and $3.749\,\mathrm{d}^{-1}$; the latter of which agrees well with the orbital frequency derived from the photometry and from the radial velocity variations. The equivalent width measurements folded over Equation 6.1 are shown in Figure 6.5 (second panel from top). As expected for an irradiation effect, maximum equivalent width takes place at $\varphi \simeq 0.5$.

6.5 Photometric and spectroscopic phase relations

The assumption that the emission lines in HS 1857+5144 originate on the inner hemisphere of the secondary star as a result of strong irradiation from the hot primary star makes specific predictions on the relative phases of the photometric and spectroscopic variability. At superior conjunction of the secondary star when the irradiated side faces the observer, $\varphi = 0.5$, the system appears brightest; the radial velocity of the secondary star is zero and crossing from red-shifted to blue-shifted velocities; the emission-line strength is at the maximum, and vice versa for the inferior conjunction of the secondary star at phase zero. Hence, one would expect an agreement in phase between the light curve and the equivalent width variation, and a 0.25 phase shift between those two parameters and the radial velocity curve (e.g. Thorstensen et al. 1978, 1994, 1996; Vennes & Thorstensen 1996; Orosz et al. 1999; Hillwig et al. 2000; Kawka et al. 2002). Figure 6.5 shows the average radial velocities of the Balmer lines and the equivalent widths of Hβ as well as the *B*-band and *R*-band light curves folded over Equation 6.1. The phase offset between the *B*-band and *R*-band light curves with respect to the equivalent width variation, as determined from sine fits, is ~ 0.004 for the *R*-band and ~ 0.018 for the *B*-band. The larger phase offset of the *B*-band light curve is probably related to the fact that

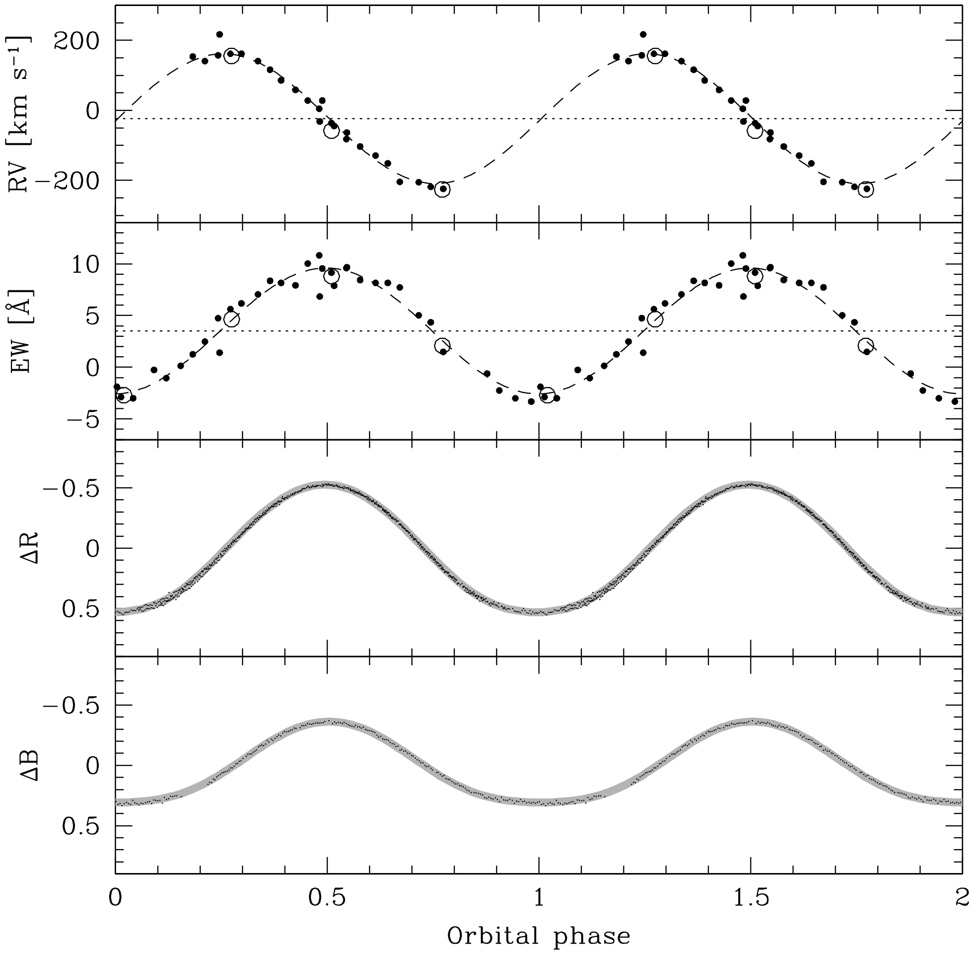

Figure 6.5: Spectroscopic and photometric data of HS 1857+5144 folded over the photometric orbital period of 383 min given in Equation 6.1. *Top two panels*: the average of the Balmer radial velocities and Hβ equivalent width variations along with the best sine fit (dashed line); the filled and open circles represent the Mcdonald and WHT data, respectively. The error bars in the radial velocity measurements are included in the plot, but of similar size as the points. The uncertainties in the values of the equivalent widths are dominated by systematic effects of the order ~ 1 Å. *Bottom two panels*: *R*-band and *B*-band light curves obtained during May/June 2006 along with the synthetic light curves (gray line) computed with the program PHOEBE for $M_{\rm wd} = 0.72\,M_{\odot}$, $M_{\rm sec} = 0.21\,M_{\odot}$, $i = 53°$, and $T_{\rm wd} = 100\,000$ K. Phase zero is defined as inferior conjunction of the secondary star. Note that phase of the radial velocity curve is offset with respected to equivalent width variation curve and light curves by $\simeq 0.25$, consistent with an origin of the emission lines on the heated inner hemisphere of the secondary star (see Section 6.5 for details).

Table 6.1: The average radial velocities of the Balmer emission lines and Hβ equivalent widths of HS 1857+5144 measured from the McDonald and WHT spectra.

HJD 245	V ($\mathrm{km\,s^{-1}}$)	EW (Å)	HJD 245	V ($\mathrm{km\,s^{-1}}$)	EW (Å)
3202.6780	4.5 ± 3.9	10.8	3202.8808	157.4 ± 6.7	4.8
3202.6857	-36.2 ± 3.4	9.1	3202.8884	161.1 ± 6.2	5.6
3202.6954	-64.0 ± 3.6	9.7	3202.8954	161.8 ± 6.4	6.2
3202.7037	-103.4 ± 3.5	8.4	3202.9058	140.2 ± 5.5	7.0
3202.7134	-128.7 ± 4.1	8.2	3202.9134	115.5 ± 5.3	8.3
3202.7211	-150.9 ± 5.1	8.2	3202.9204	85.9 ± 4.8	8.1
3202.7287	-204.6 ± 6.8	7.7	3202.9294	58.8 ± 4.6	7.9
3202.7405	-205.2 ± 6.1	5.0	3202.9371	28.6 ± 4.5	10.0
3202.7482	-218.7 ± 6.1	4.4	3202.9447	-31.9 ± 6.4	6.8
3202.7836	-	-0.6	3202.9537	-44.8 ± 4.7	7.9
3202.7912	-	-2.3	3202.9614	-82.5 ± 5.0	9.6
3202.8013	-	-3.0	3205.6857	-224.3 ± 8.1	1.5
3202.8114	-	-3.3	3205.7468	-	-1.9
3202.8197	-	-2.9	3205.8114	217.3 ± 10.4	1.4
3202.8273	-	-3.0	3205.8760	28.6 ± 4.7	9.5
3202.8405	-	-0.2	3919.3887	-57.8 ± 2.8	8.7
3202.8482	-	-1.0	3920.3912	155.6 ± 3.5	4.6
3202.8572	-	0.1	3921.3888	-	-2.7
3202.8648	153.1 ± 10.3	1.2	3922.3880	-226.1 ± 4.7	2.1
3202.8725	140.8 ± 8.7	2.5			

Notes: The statistical error of the Hβ equivalent widths is $\sim 0.01 - 0.05$ Å, which is negligible. The systematic error, however, is of the order ~ 1 Å, depending on the details of how the continuum flux is determined.

it does not cover the entire orbital cycle, and hence the sine fit results in larger uncertainties. The phase of the folded equivalent width variation lags that of the radial velocity curve by 0.25 ± 0.01 orbital cycle.

The phase-dependent behaviour of the emission lines, and the relative phases of the photometric, radial velocity, and equivalent width variations found in our data corroborate the hypothesis of the emission lines in HS 1857+5144 originating on the inner face of the secondary star illuminated by the hot white dwarf.

6.6 Stellar components

6.6.1 Light curve solution

In order to determine additional constraints on the system parameters from the observed reflection effect, we modelled the light curves of HS 1857+5144 with the 'PHysics Of Eclipsing BinariEs' program PHOEBE[1] (Prša & Zwitter 2005), which is built on top of the widely used WD code (Wilson & Devinney 1971; Wilson 1979, 1990). We simultaneously fitted the R-band and B-band data obtained at Kryoneri Observatory under the following assumptions: (a) circular orbits and synchronous rotation of the secondary star; (b) stellar surface temperature and brightness were computed assuming blackbody emission; (c) a detailed calculation of the reflection effect was adopted; (d) linear limb darkening was chosen, where the limb darkening coefficient was interpolated from Claret (2000); (e) gravity darkening exponents of 1 (von Zeipel 1924) and 0.32 (Lucy 1967) were used for radiative and convective stars, respectively; (f) no contribution fluxes from a spot or third light were applied.

In our analysis, we tested a wide range of white dwarf masses, covering $M_{\rm wd} = 0.3 - 1.4\,M_\odot$. We then assumed an M-type companion star, testing the whole range of spectral types M9–M0 V, corresponding to masses, radii, and temperatures of $M_{\rm sec} \simeq 0.07 - 0.53\,M_\odot$, $R_{\rm sec} \simeq 0.11 - 0.56\,R_\odot$, and $T_{\rm sec} \simeq 2300 - 3800$ K, interpolated from Rebassa-Mansergas et al. (2007). Earlier spectral types than M0 V would imply extremely massive white dwarfs (Section 6.6.3) which are excluded by the spectral fit (Section 6.6.2)[2]. This approach allows us to search for possible solutions over a large range of possible mass ratios, $q = M_{\rm sec}/M_{\rm wd} \simeq 0.05 - 1.77$. For each input q, we fixed $P_{\rm orb} = 0.26633$ d and $T_{\rm sec}$ according to the selected spectral type of the companion star. The following parameters were free in the

[1] http://phoebe.fiz.uni-lj.si/

[2] A strict upper limit on the mass of the companion comes from the fact that it is not Roche-lobe filling. Using $\bar{\rho} \simeq 107 P_{\rm orb}^{-2}({\rm h})$ (Equation 1.4), with $\bar{\rho}$, the average density of the donor, and $P_{\rm orb}({\rm h})$, the orbital period in hours for a Roche-lobe filling star, the maximum mass of a main-sequence companion in HS 1857+5144 is $M_{\rm sec} < 0.72\,M_\odot$, corresponding to a spectral type K3 V or later.

fits: q, white dwarf temperature ($T_{\rm wd}$), orbital inclination (i), surface potentials for both components, and albedo of the secondary star ($ALB2$). The fits for early type companions, M2–M0 V, do not reproduce well the observed B and R light curves, which supports the exclusion of early-type donors outlined above. We found that, independently from the details of a given fit, the system must contain a hot white dwarf with $T_{\rm wd} > 60\,000$ K and a cool component with an albedo higher than that of a normal M star ($ALB2 > 0.5$) to reproduce the large amplitude observed in the light curves. Such high $T_{\rm wd}$ is also confirmed by the spectral fit to the WHT faint-phase spectrum in the following section. Fitting the B-band and R-band light curves alone provides a fairly large range of possible system parameters, $M_{\rm wd} \simeq 0.3 - 1.4\,M_{\odot}$, $M_{\rm sec} \simeq 0.066 - 0.367\,M_{\odot}$, (spectral type M9–M3 V), $i \sim 40^{\circ} - 60^{\circ}$, and $T_{\rm wd} \sim 60\,000 - 100\,000$ K. For a given $M_{\rm sec}$, a more massive white dwarf requires a larger inclination and a higher $T_{\rm wd}$.

Figure 6.5 (bottom two panels) presents the corresponding R-band and B-band synthetic light curves from the program PHOEBE for $M_{\rm wd} = 0.72\,M_{\odot}$, $M_{\rm sec} = 0.21\,M_{\odot}$, $i = 53^{\circ}$, and $T_{\rm wd} = 100\,000$ K, along with the observed light curves folded over the ephemeris in Equation 6.1. The choice of this particular set of parameters is detailed below in Section 6.6.4, but other fits in the parameter range given above fit the data equally well.

6.6.2 Spectral fit

We performed a spectral fit to the faint-phase WHT spectrum of HS 1857+5144 to obtain an independent estimate of $M_{\rm wd}$ and $T_{\rm wd}$, using both a grid of LTE pure-hydrogen models (Koester et al. 2005), and a grid of NLTE models with a variety of He abundances[3]. We fitted the Hβ and Hγ absorption lines after normalising the continua of the observed data and the model spectra in the same way using a third-order polynomial. The fits suggest $80\,000\,{\rm K} \lesssim T_{\rm wd} \lesssim 100\,000$ K and $7.5 \lesssim$

[3] http://astro.uni-tuebingen.de/~rauch

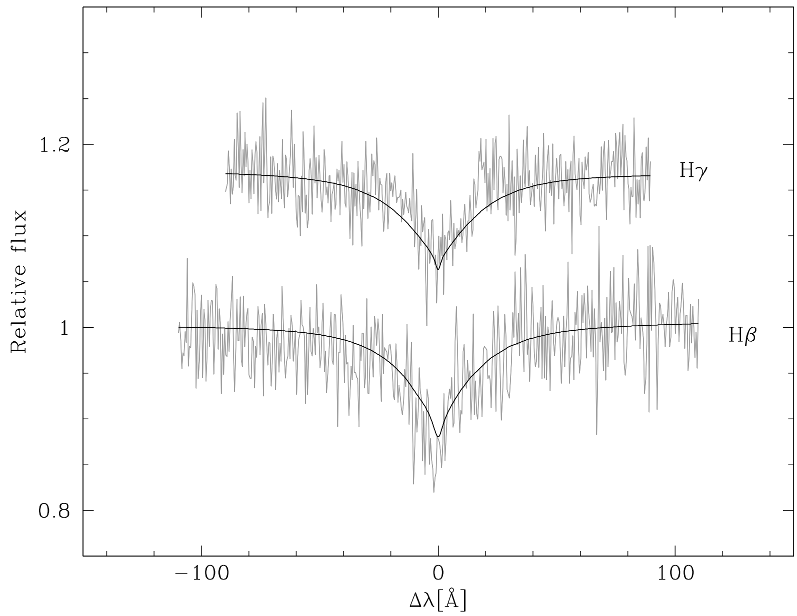

Figure 6.6: Hβ and Hγ from the WHT faint-phase spectrum ($\varphi = 0.02$) fitted with an LTE model for $T_{\rm wd} = 100\,000$ K and $\log g = 8.0$.

$\log g \lesssim 8.5$ (corresponding to $0.6\,M_{\odot} \lesssim M_{\rm wd} \lesssim 1.0\,M_{\odot}$) for the LTE models, and $70\,000\,{\rm K} \lesssim T_{\rm wd} \lesssim 100\,000\,{\rm K}$ and $8.0 \lesssim \log g \lesssim 8.5$ (corresponding to $0.7\,M_{\odot} \lesssim M_{\rm wd} \lesssim 1.0\,M_{\odot}$) for the NLTE models. Figure 6.6 shows the best LTE fit to Hβ and Hγ for $T_{\rm wd} = 100\,000$ K and $\log g = 8.0$. These numbers should be considered as rough estimates only, as the optical spectrum of HS 1857+5144 is contaminated by flux from the companion star, which is very difficult to quantify. A more reliable temperature and mass estimate would require far-ultraviolet data, where the white dwarf dominates the emission of the system (Good et al. 2004). We conclude from this qualitative spectral analysis that the white dwarf in HS 1857+5144 is indeed very hot, and given the high surface gravity preferred by the fits, is more likely to be a white dwarf than a subdwarf. The detection of He II λ4686 then qualifies the primary as a DAO white dwarf.

6.6.3 K-correction and mass ratio-inclination constraints

As mentioned already in Section 6.4, the emission lines in HS 1857+5144 trace the orbit of the centre of light of the illuminated hemisphere of the secondary star, and not its centre of mass. Hence, for a dynamic assessment of the binary parameters, the measured velocity K_{em} (Section 6.4) has to be corrected accordingly. The radial velocity amplitude of the secondary star's centre of mass, $K_{\mathrm{sec,cor}}$ can be expressed according to Wade & Horne (1988) as

$$K_{\mathrm{sec,cor}} = \frac{K_{\mathrm{em}}}{1-(1+q)(\Delta R/a)} \quad ,$$

where ΔR is the displacement of the centre of light from the centre of mass of the secondary star, with $0 \lesssim \Delta R \lesssim R_{\mathrm{sec}}$ ($\Delta R = 0$ implies that the centre of light coincides with the centre of mass of the secondary star, whereas $\Delta R = R_{\mathrm{sec}}$ is the maximum possible displacement, where all the light comes from a small region on the secondary star closest to the primary star). Assuming that the emission due to irradiation is distributed uniformly over the inner hemisphere of the secondary star, and zero on its unirradiated face, $\Delta R = (4/3\pi)R_{\mathrm{sec}}$ (Wade & Horne 1988; Wood et al. 1995; Orosz et al. 1999; Vennes et al. 1999).

The expected radial velocity of the secondary star ($K_{\mathrm{sec,cal}}$) is

$$K_{\mathrm{sec,cal}} = \frac{2\pi a \sin i}{P_{\mathrm{orb}}(1+q)} \quad ,$$

where a is the binary separation. Equating $K_{\mathrm{sec,cor}} = K_{\mathrm{sec,cal}}$ then gives a unique q for a given choice of i, Hence, a fixed value of i projects onto a one-dimensional curve within the $(M_{\mathrm{wd}}, M_{\mathrm{sec}})$ plane, and for the possible range of parameters considered here, those curves are nearly straight lines.

6.6.4 Combined constraints

In Sections 6.6.1–6.6.3 above, we have outlined what type of constraints on the system parameters of HS 1857+5144 can be derived from the observed light curves, radial velocity variations, and the spectrum of the primary star. Here, we will combine all those independent constraints.

In a first step, we imposed a range of $i = 40^\circ - 60^\circ$, as suggested by the set of PHOEBE fits to the B-band and R-band light curves, on the combinations of $(M_{\rm wd}, M_{\rm sec})$ which are consistent with the corrected radial velocity $K_{\rm sec,cor}$ of the secondary star. The resulting parameter range is indicated by the gray shaded area in Figure 6.7. In a second step, we inspected the individual light curve fits from the grid of PHOEBE runs, and required the inclination of a model for a given $(M_{\rm wd}, M_{\rm sec})$ to fall within $\pm 5^\circ$ of the corresponding inclination constraint from the radial velocity of the secondary star. We introduced this "fuzziness" in inclination as a measure to account for systematic uncertainties within the K-correction and the light curve fits. Possible combinations of $(M_{\rm wd}, M_{\rm sec})$ are indicated by filled circles in Figure 6.7, and trace a somewhat narrower band than the initial $i = 40^\circ - 60^\circ$ constraint. A final constraint comes from the spectral fit of the WHT faint phase spectrum (Section 6.6.2), which implied $0.6\,M_\odot \lesssim M_{\rm wd} \lesssim 1.0\,M_\odot$, shown as vertical dashed lines in Figure 6.7.

The combination of all constraints suggests $0.15\,M_\odot \lesssim M_{\rm sec} \lesssim 0.30\,M_\odot$ (spectral type M6–M4 V), $0.6\,M_\odot \lesssim M_{\rm wd} \lesssim 1.0\,M_\odot$, $70\,000\,{\rm K} \lesssim T_{\rm wd} \lesssim 100\,000\,{\rm K}$, and $45^\circ \lesssim i \lesssim 55^\circ$. A substantial improvement on this set of parameters will require measuring the radial velocity amplitude of the white dwarf, $K_{\rm wd}$, and determining an accurate temperature for the primary. Both types of measurements could be easily obtained from time-resolved ultraviolet spectroscopy.

6.6.5 2MASS magnitudes

HS 1857+5144 is detected in the 2MASS (Skrutskie et al. 2006) at $J = 15.09 \pm 0.04$, $H = 15.05 \pm 0.08$, $K_{\rm s} = 14.76 \pm 0.14$. Our ephemeris is good enough to establish the orbital phase of the 2MASS data, which is very close to orbital maximum, $\varphi \simeq 0.5$. In order to test to what extent the optical-infrared spectral energy dis-

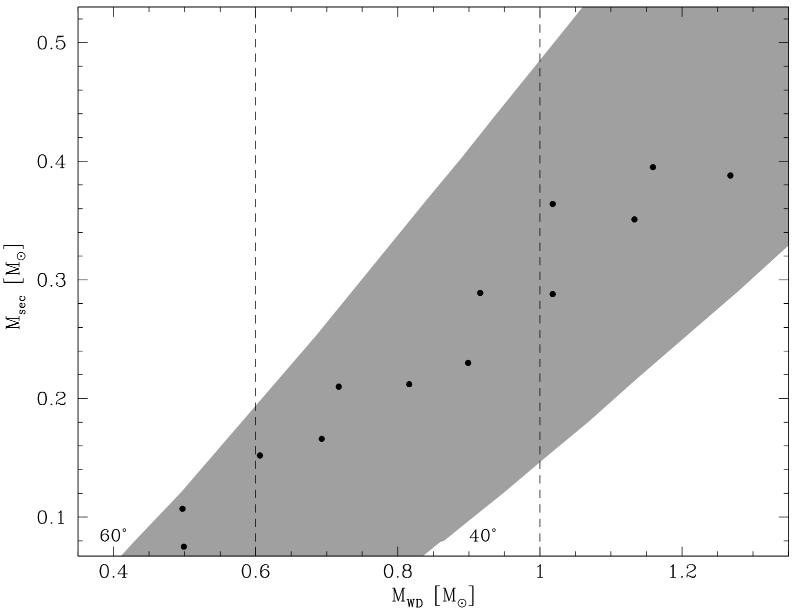

Figure 6.7: Photometric and spectroscopic constraints on ($M_{\rm wd}$, $M_{\rm sec}$). The gray shaded area represents possible dynamical solutions from the "K-corrected" radial velocity of the secondary star for $K_{\rm em} = 185\,{\rm km\,s^{-1}}$ and for $i = 40° - 60°$. Filled circles represent possible solutions from the light curve analysis for given ($M_{\rm wd}$, $M_{\rm sec}$) in which i agrees with spectroscopic constraint within $\pm 5°$. Dashed lines are upper and lower limits on $M_{\rm wd}$ derived from the spectral fit (see Section 6.6.4 for details).

tribution (SED) of HS 1857+5144 is compatible with the stellar photometry and spectroscopy, we modelled the $BRJHK_{\rm s}$ parameter range obtained from the analysis of the time-resolved magnitudes with the sum of a white dwarf spectrum from Koester et al. (2005) and a blackbody representing the contribution of a (heated) low-mass companion. The data leave some freedom in the exact parameters, however, as an example, a fairly good fit is achieved for $T_{\rm wd} = 70\,000\,{\rm K}$, $T_{\rm sec} = 6000\,{\rm K}$, $R_{\rm wd} = 1.3 \times 10^9\,{\rm cm}$, corresponding to $M_{\rm wd} \simeq 0.6\,M_\odot$, and $R_{\rm sec} = 1.3 \times 10^{10}\,{\rm cm}$, corresponding to a spectral type of M6, at a distance of 460 pc (Figure 6.8). This solution coincides well with the photometric and spectroscopic constraints in Figure 6.7. Overall our simple model confirms the stellar parameters established in the previous sections, with a slight preference for a white dwarf mass in the range

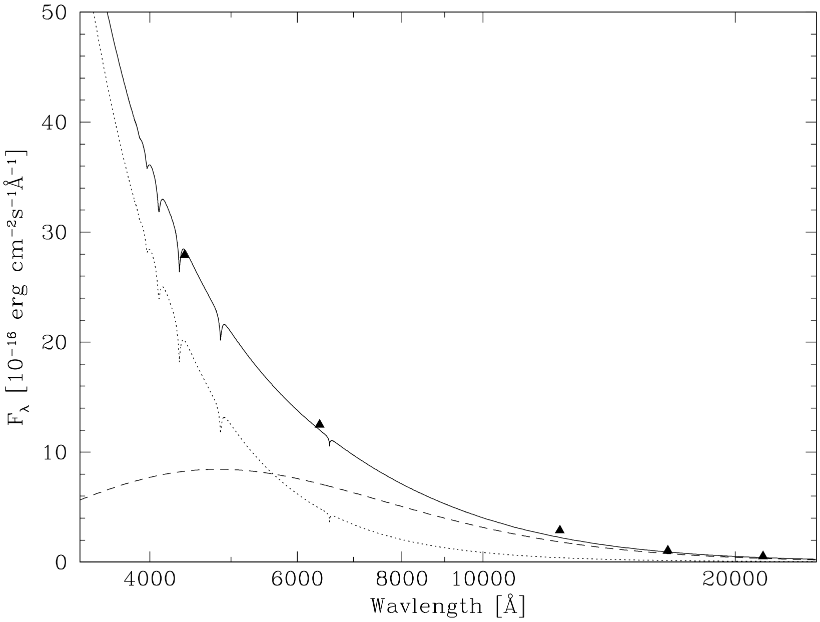

Figure 6.8: The $BRJHK_s$ fluxes of HS 1857+5144 (filled triangles) at orbital maximum ($\varphi \simeq 0.5$) along with an example of a plausible fit (solid line) with the sum of a white dwarf spectrum (dots) and a blackbody (dashed line) representing the heated side of the low-mass companion, assuming $T_{wd} = 70\,000$ K, $T_{sec} = 6000$ K, $R_{wd} = 1.3 \times 10^9$ cm, and $R_{sec} = 1.3 \times 10^{10}$ cm, at a distance of 460 pc (see Section 6.6.5 for details).

$M_{wd} = 0.6 - 0.8\,M_\odot$, and a companion star with a radius near the lower end of the determined range, i.e. corresponding to a spectral type M6–M5, and a distance to the system of 290–460 pc.

Table 6.2: PCEBs with a large reflection effect.

Object	P_{orb} [d]	SP1	SPsec	T_1 [K]	M_1 [$M_\odot$]	M_{sec} [$M_\odot$]	Reflection effect [mag] B	V	R	Ref.
NN Ser	0.130	DAO	M4.75 V	$57\,000 \pm 3000$	0.54 ± 0.05	0.150 ± 0.008	0.33	0.49	0.772	1, 2
HS 1857+5144	0.266	DAO	~M6-M4 V	$\sim 70\,000 - 100\,000$	$\sim 0.6 - 1.0$	$\sim 0.15 - 0.30$	0.7		1.1	this work
TW Crv	0.328	sdO	M V	$105\,000 \pm 20\,000$	$\sim 0.55 - 0.61$	< 0.3	0.74	0.85	0.93	3, 4
KV Vel	0.357	sdO,PN	M V	$77\,000 \pm 3000$	0.63 ± 0.03	0.23 ± 0.01	0.49	0.55	0.61	5
V477 Lyr	0.472	sdOB,PN		$60\,000 \pm 10\,000$	0.51 ± 0.07	0.15 ± 0.02	0.5	0.6		6, 7
V664 Cas	0.582	sdO,PN	K5-F5 V	$83\,000 \pm 6000$				1.15		4, 8
VW Pyx	0.676	sdO,PN		$85\,000 \pm 6000$				1.36		9, 10
Abell 65	1	sd?,PN		$\sim 80\,000$				> 0.5		11, 12
BE UMa	2.291	sdO/DAO,PN	K4-3 V	$105\,000 \pm 5000$	0.70 ± 0.07	0.36 ± 0.07		~ 1.3		13, 14, 15

References: (1) Haefner (1989); (2) Haefner et al. (2004); (3) Chen et al. (1995); (4) Exter et al. (2005); (5) Hilditch et al. (1996); (6) Bond & Grauer (1987); (7) Pollacco & Bell (1994); (8) Shimanskii et al. (2004); (9) Kohoutek & Schnur (1982); (10) Exter et al. (2003); (11) Bond & Livio (1990); (12) Walsh & Walton (1996); (13) Ferguson et al. (1987); (14) Wood et al. (1995); (15) Ferguson et al. (1999)

6.7 Discussion, part III

The analysis presented in Section 6.6.2 suggests that HS 1857+5144 contains a hot white dwarf with $T_{\rm wd} \simeq 70\,000 - 100\,000$ K. The implied cooling age of the white dwarf is $1.2 - 6 \times 10^5$ yr (Bergeron et al. 1995, and Bergeron 2002, private communication), making HS 1857+5144 one of the youngest PCEBs known to date. Following the prescription of Schreiber & Gänsicke (2003), and assuming the range of system parameters established in Section 6.6 as well as "classical" magnetic braking for the angular momentum loss mechanism, we estimate the period at which HS 1857+5144 left the common envelope phase to be $P_{\rm CE} \simeq 0.266334 - 0.266345$ d, very close to its present orbital period. HS 1857+5144 will evolve within the next $\sim 0.4 - 1.3 \times 10^{10}$ yr into a semi-detached CV configuration, and start mass transfer at an orbital period of $\simeq 0.08 - 0.13$ d, i.e. within or below the period gap. The large uncertainties on the future evolution are a consequence of the limited constraints on the system parameters. Additional systematic uncertainties in the actual strength of angular momentum loss from the orbit have not been taken into account.

Among ~ 40 previously known PCEBs listed in Schreiber & Gänsicke (2003), and Shimansky et al. (2006), only 8 systems display a reflection effect comparable to that of HS 1857+5144 (Table 6.2). All these systems contain extremely hot white dwarfs or subdwarfs, and all are very young PCEBs that may serve as observational probes into our understanding of common envelope evolution.

A large reflection effect is expected for those PCEBs containing a hot subdwarf, because of the larger luminosity compared to a white dwarf of the same temperature, and indeed the majority of known PCEBs with a large reflection effect have sdO primary stars. So far, only one PCEB, HS 1136+6646 (Sing et al. 2004), containing a hot white dwarf similar to HS 1857+5144 is known. The secondary star in HS 1136+6646 has been suggested to be a K7–4 V star on the basis of its spectral type, which appears too early for the estimated mass of $0.34\,M_{\odot}$. However, Sing et al. (2004) discuss the possibility that the secondary is overluminous as it is still out of thermal equilibrium after accreting at a high rate during the common envelope phase. The amplitude of the reflection effect in HS 1136+6646 is much lower than in HS 1857+5144, which is consistent with its longer orbital period of 0.84 d. The other system most similar to HS 1857+5411 is BE UMa, which has been classified as a borderline object between an sdO subdwarf and a DAO white dwarf (Liebert et al. 1995; Ferguson et al. 1999), and is associated with a planetary nebula. It is interesting to note that six out of the nine systems listed in Table 6.2 are still embedded in planetary nebulae. Our long-slit spectroscopy of HS 1857+5144 does not reveal any noticeable trace of extended emission around Hα, though a deep Hα image testing for remnant nebular emission would be useful. Similarly, no sign of extended Hα emission around HS 1136+6646 has been observed. While the majority of very young PCEBs are still embedded in their planetary nebulae/common envelopes, the discovery of HS 1857+5144 and HS 1136+6646 suggests that the envelope can be dispersed rather quickly.

6.8 Summary

We have identified a pre-CV, HS 1857+5144, containing a hot DAO white dwarf and a low mass M V star with an orbital period of $P_{\rm orb} = 383.52$ min. The light curves of HS 1857+5144 display a very large reflection effect with peak-to-peak amplitudes of 0.7 and 1.1 mag in the *B*- and *R*-band, respectively. Combining the results of our spectroscopic and photometric analyses, we constrain the system parameters to $0.15\,M_{\odot} \lesssim M_{\rm sec} \lesssim 0.30\,M_{\odot}$ (spectral type M6–M4 V), $0.6\,M_{\odot} \lesssim M_{\rm wd} \lesssim 1.0\,M_{\odot}$, $70\,000\,{\rm K} \lesssim T_{\rm wd} \lesssim 100\,000\,{\rm K}$, and $45^{\circ} \lesssim i \lesssim 55^{\circ}$. Taking these parameters at face value, HS 1857+5144 is one of the youngest PCEBs known to date and has just emerged from the post common envelope phase. The system will eventually evolve into a CV, and start mass transfer within or below the $2-3$ h orbital period gap.

Chapter 7

Discussion: a big picture of the survey

In Chapter 1, I pointed out the serious discrepancies between the CV population predicted by the standard scenario of CV evolution theory and the observed one, which may be caused either by uncertainties in the theory or by observational selection effects among the known CVs. A rather likely selection effect is that CVs with low-amplitude variability and CVs that are intrinsically faint and/or not particularly blue, as well as faint X-ray systems, are most certainly underrepresented in the known sample of CVs. The main path towards an understanding of the evolution of CVs is to create a model that can reproduce all features found in the observed period distribution. On the observational side, it is necessary to characterise a large and unbiased CV sample as a major tool to test and calibrate the theoretical population models. The work presented in this thesis is part of a large effort of our team in Warwick to establish the properties of the intrinsic CV population of our Galaxy using a homogeneous selection scheme, with the specific aim to derive the orbital period distribution of the HQS CV sample. Our selection criterion, the spectroscopic fingerprint of CVs, has never been systematically exploited before and we have shown that our selection method is very sensitive to short-period CVs (see

Section 1.8.3 for details). We should, therefore, be able to identify a large number of CVs below the period gap, if they exist in the predicted space density.

7.1 An overview of the new CVs and pre-CVs in the HQS

We have discovered 53 new CVs/pre-CVs in the HQS (Table 7.2). The follow-up observations of these candidates have led to the discovery of a number of interesting and rare systems, including nine new CVs, HS 0139+0559, HS 0229+8016, HS 0417+7445, HS 0506+7725, HS 0642+5049, HS 1016+3412, HS 1340+1524, HS 1857+7127, and HS 2214+2845, as well as one new pre-CV, HS 1857+5144 presented in this thesis (Chapters 4–6). The list below gives several examples of such objects found in the survey.

7.1.1 The new HQS CVs with orbital period measurements

- **Short-period dwarf novae**
  - The HQS identified eight short-period dwarf novae, of which HS 0417+7445, HS 1017+5319, HS 1449+6415, and HS 2219+1824, are SU UMa type. HS 1449+6415 is found near the minimum period and has a relatively small outburst amplitude ($\sim$ 3.5 mag) among the SU UMa stars with orbital periods less than 90 min, other than ER UMa stars (Nogami et al. 2000 and see also Nogami et al. 1997). HS 2219+1824 is characterised by a long recurrence time between outbursts; no normal outburst has been detected (Rodríguez-Gil et al. 2005a). The optical spectra of the system clearly reveal the photospheric emission of the white dwarf similar to that of low mass-transfer short-period dwarf novae such as WZ Sge (Greenstein 1957; Gilliland et al. 1986), GW Lib (Duerbeck &

Seitter 1987), BC UMa (Mukai et al. 1990), and BW Scl (Abbott et al. 1997).

– HS 0913+0913 has an orbital period just at the lower edge of the period gap (Tappert & Bianchini 2003). The system was proposed as an IP candidate due to its long-term outbursting behaviour, the unusual strength of the He II emission, and the appearance of an absorption component during rise to outburst (Kato et al. 2002a; Tappert & Bianchini 2003).

– HS 2331+3905 is an enigmatic short-period likely dwarf nova that resembles WZ Sge (Araujo-Betancor et al. 2005a). The system contains a cold white dwarf and most likely a brown dwarf donor, and it is eclipsing with an orbital period of $\simeq 81.1$ min. Another photometric period was detected at $\simeq 83.4$ min which might relate to the presence of permanent superhumps. Most puzzling, however, is the detection of a large amplitude radial velocity variation in the emission line wings with a period ~ 3.5 h which is in no way related to the orbital period. HS 2331+3805 exhibits the photometric behaviour of a pulsating white dwarf; it is the brightest CV among this class of extremely rare objects, making it the prime target for detailed follow-up studies. The system is characterised by extremely low mass-transfer and has never been observed in outburst, turning the system into a dwarf nova candidate.

– Another two short-period dwarf novae that have rare outbursts are HS 1016+3412 and HS 1340+1524 (Chapter 5).

- **Long-period dwarf novae**

  Among the long-period dwarf novae, the HQS identified two rare bright systems exhibiting deep eclipses, which are HS 0907+1920 and HS 1804+6753. HS 0907+1920 (Gänsicke et al. 2000; for system parameters see Thorstensen 2000; Shafter et al. 2000) shows no strong orbital hump in the quiescent light curves, suggesting that the system may contain a faint bright-spot, resulting from a mass-transfer rate lower than in normal dwarf novae above the period gap (Kato et al. 2002b; Feline et al. 2005). HS 1804+6753 is characterised by low-amplitude outbursts and eclipses of the white dwarf and the hot spot (Billington et al. 1996; see system parameters in Fiedler et al. 1997; Baptista et al. 2000; Shafter & Holland 2003; and structure of accretion disc of the system in Joergens et al. 2000; Baptista & Catalán 2001).

- **Novalike variables**

  Nine novalike variables have been classified in the HQS and all inhabit in the 3–4 h orbital period range. The most abundant species of the class belong to the exotic SW Sex stars: HS 0357+0614 (Thorstensen & Taylor 2001), HS 0728+6738 (Rodríguez-Gil et al. 2004b), HS 0129+2933, HS 0220+0603, HS 0455+8315, HS 0805+3822, and HS 1813+6122 (Rodríguez-Gil et al. 2007b). While they have relatively strong emission lines, they are weak X-ray emitters, and display only moderate variability.

- **IPs**

  A handful of the HQS CVs have been added to the class of IPs, which do not show large-amplitude variability.

  - Specifically, HS 0618+7336 is an IP with a soft X-ray excess, adding the system to a small group of soft IPs (Araujo-Betancor et al. 2003a; Staude et al. 2003).
  - HS 0752+6314 (Tovmassian et al. 1998; Kemp et al. 2002) and HS 0756+1624 (Rodríguez-Gil et al. 2004a; Patterson et al. 2004) are short-period IPs having orbital periods near the observed period minimum of hydrogen-rich CVs. Although they have orbital periods in common, their observed properties are dramatically different. HS 0752+6314 is a low mass-transfer system (de Martino et al. 2005; Evans & Hellier 2005)

which occasionally displays short outbursts similar to a short-period IP, EX Hya (Kemp et al. 2002; Ishioka et al. 2002). In contrast, HS 0756-+1624 never been observed to undergo an outburst, but it occasionally exhibits low states, resembling the behaviour of the high mass-transfer VY Scl stars (Rodríguez-Gil et al. 2004a).

- HS 0943+1404 shows signatures of being a transitional object between IPs and polars i.e. having an unusually large $P_{\mathrm{spin}}/P_{\mathrm{orb}}$ ratio, a long orbital period, and the magnetic moment of the white dwarf found in the range of polars, and it undergoes deep low states which are characteristic of polars (Rodríguez-Gil et al. 2005b).

- **Polars/pre-polars**

  The HQS has turned out to be efficient in identifying extremely rare magnetic systems such as high-field polars and pre-polars.

  - HS 1552+2730 is a polar found in the period gap (Tovmassian et al. 2001; Thorstensen & Fenton 2002). The system has an extremely high magnetic field strength of ~ 160 MG, which is the second highest field observed in polars (Gänsicke et al. 2004b; Schwope et al. 2006). HS 1552-+2730 shows signs of an unusually low mass-transfer rate and frequently switches between high and low states (Tovmassian et al. 2001).
  - HS 1023+3900 (Reimers et al. 1999; Vogel et al. 2007) and HS 0922+1333 (Reimers & Hagen 2000) are probably pre-polars containing a very cold white dwarf and a late-type stellar companion which is not filling its Roche lobe. These systems were identified as low accretion rate polars due to their extremely low accretion rate from a stellar wind.

- **Pre-CVs**

  Among new 53 systems, HS 1857+5144, is classified as one of the youngest pre-CVs containing a very hot white dwarf (see Chapter 6). In addition, a confirmed pre-CV, HS 1316+6747, has been discovered in this survey. HS 1316+6747 was first identified as a CV candidate by Green et al. (1986). However, the lack of significant variability in the light curve (Misselt & Shafter 1995), and the absence of emission lines in its spectrum (Tappert et al. 2000) were thought to make this system unlikely to be a CV; based on our unpublished spectroscopic and photometric data this system is a definite pre-CV, showing occasionally Balmer emission lines which are likely to be caused by a phase-dependent reflection effect with an orbital period of the order of a few days.

- **Uncertain classification**
  - Interestingly, the detached white dwarf/red dwarf binary HS 2237+8154, containing a very cold white dwarf, is found just at the upper edge of the period gap, with an orbital period of 178 min. Gänsicke et al. (2004a) classified the system as either one of the oldest pre-CVs close to the onset of mass transfer, a CV that terminated mass transfer and entered the period gap, or a hibernating nova.
  - HS 0139+0559 and HS 0229+8016 have been identified in this work as either UX UMa-type novalike variables or as Z Cam-type dwarf novae. These systems exhibit clean quasi-sinusoidal radial velocity variations of their emission lines but no or very little orbital photometric variability.

7.1.2 The new HQS CVs with no orbital period measurements

The orbital periods of most CVs in the HQS have already been measured and only a few systems await spectroscopic and photometric observations to determine their orbital periods (see Table 7.2). Among them, HS 0019+3947, HS 0038+4308, and

HS 0058+4307 are spectroscopically very similar to HS 0139+0559, HS 0229+8016, and HS 0642+5049 which are characterised by thick-disc absorption line spectra that resembles those of high mass-transfer novalike variables or dwarf novae in outburst. In particular, photometric data of HS 0058+4307 does not show significant variability; the system has been proposed as a Z Cam-type dwarf nova by Kato et al. (2003). The identification spectrum of HS 0002+0901 suggests that the system is a CV dominated by a K-type donor. The three systems, HS 0124+3752, HS 0128+3547, and HS 1434+2355 are probably short-period dwarf novae. Based on our spectroscopic and photometric data, HS 1634+4658 is likely to be a long-period novalike variable. Finally, HS 0819+2003 is a CV candidate which shows transient Balmer and He II emission.

In summary, many of the CVs identified in the HQS fulfil the criterion of "hard-to-find" objects, with infrequent/no, or low-amplitude outbursts, weak X-ray emission , and small-amplitude variability that might be inconspicuous in variability and X-ray surveys.

7.2 The period distribution of the HQS CVs

So far, the orbital periods of 44 HQS CVs/pre-CVs (Table 7.2) have been measured through the combined effort of our team, investing large amounts of observing time. Figure 7.1 (left panel) presents the orbital period distribution of the 42 new HQS CVs (excluding two pre-CVs, HS 1857+5144 and HS 1316+6764, and assuming that HS 2237+8154 is a CV that turned off mass transfer and entered the period gap). Although the orbital period distribution of the new HQS CVs is still not complete, with $\sim$ 20% of them lacking orbital period measurements, the similarities between the distribution in Figure 7.1 (left panel) and that of the known CV population in Figure 1.2 (Ritter & Kolb 2003) are evident: the existence of the $2-3$ h period gap, the small number of systems at $P_{\rm orb} \gtrsim 6$ h, and the minimum period cut-off at $\sim$

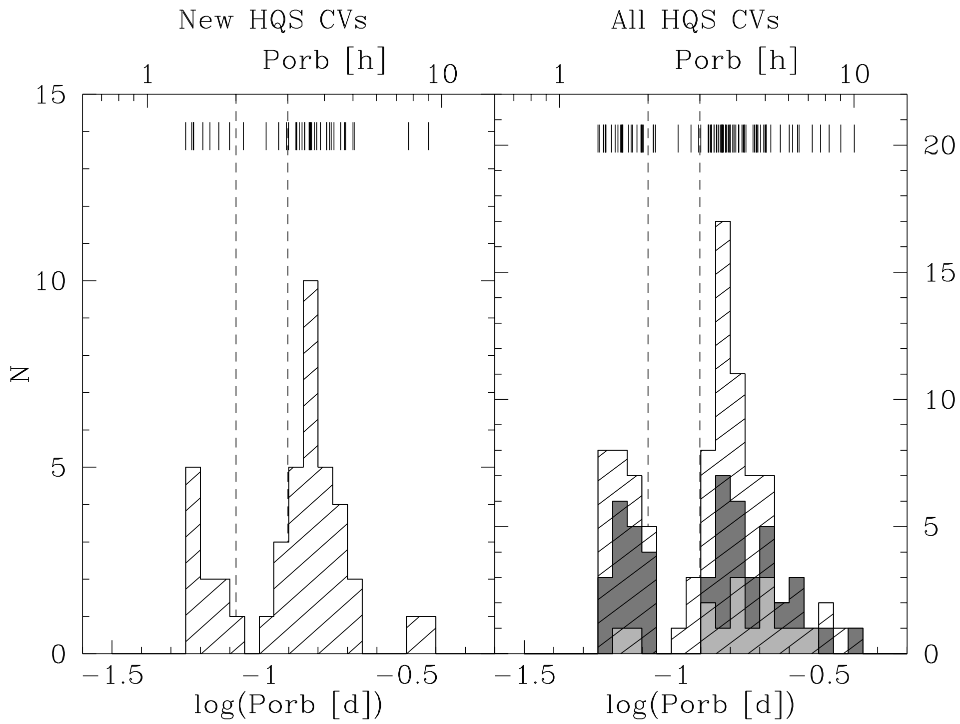

Figure 7.1: *Left panel:* Orbital period distribution of 42 new HQS CVs. *Right panel:* Orbital period distribution of all HQS CVs consisting of 42 new HQS CVs (white shade) and 49 previously known CVs that are contained in the HQS spectral data base; the systems that were recovered by the spectroscopic selection criterion are represented in dark gray shade; those which were not recognised are shown in light gray shade (see Section 7.2 for details). The tick-marks indicate the individual periods. The conventional 2–3 h period gap is represented by dashed lines. The data of the previously known HQS CVs are provided by B. Gänsicke.

80 min. The characteristics of the HQS CV period distribution can be summarised as follows.

7.2.1 The lack of short-period systems

In contrast with the predictions made by the standard model, only a small number of new HQS CVs have been discovered below the period gap, with just $\sim 33\%$ (14 out of 42) short-period systems ($P_{\rm orb} \lesssim 3$ h) found in our sample. Figure 7.1 (right panel) presents *all* CVs discovered in the HQS, i.e. the previously known CVs (gray shade) plus the new HQS discoveries (white shade); see below for the details. Table 7.1 reveals an extremely interesting ratio of short-period ($P_{\rm orb} \lesssim 3$ h) to long-period ($P_{\rm orb} > 3$ h) new HQS CVs which is *only a half of the value* of that of the known CVs in the Ritter & Kolb catalogue[1], i.e. the relative fraction of short-period CVs among the new HQS CVs is even lower than in the generic Ritter & Kolb catalogue. In what follows, I present an updated discussion of the CV discovery efficiency of the HQS and of the overall properties of the HQS CV sample (see Gänsicke et al. (2002b) for an earlier summary). In order to compare the ratio of short- to long-period systems of the new HQS CVs with the previously known CVs contained in the HQS, we separate them into two groups, i.e. the systems that were recovered and those that were not recovered by our spectroscopic selection criterion. A large fraction of short-period systems was recovered by this criterion (Figure 7.1, right panel, dark gray shade); there are only two systems (TY Psc and TY Uma) that were not recognised (Figure 7.1, right panel, light gray shade). In particular, the equal number of short-period and long-period systems (see Table 7.1) implies that we should easily find the same fraction for the new HQS CVs within the same magnitude limit. Despite our method being most efficient in detecting low mass-transfer systems, the number of new short-period systems is *only half that of* the new long-period systems, suggesting that a large fraction of short-period CVs (i.e. with strong emission lines) have already been found before our survey, because of their variability and/or X-ray emission.

A full discussion of the implications that our search for CVs in the HQS has for our understanding of the galactic CV population must await the characterisation of the complete HQS CV sample. However, an important preliminary statement that will not substantially change is: *there is no large population of nearby short-period CVs that resemble the known template systems*. Phrased differently, if the large population of short-period CVs predicted by theory exists, the majority of

[1]Ritter & Kolb (2003), Edition 7.5 of July 1, 2005, within the orbital period range of ~ 1 h to ~ 1 d and removing AM CVn systems

Table 7.1: CVs population in the HQS, the PG, and the Ritter & Kolb (2003).

Surveys/catalouge	Short $P_{\rm orb}$	Long $P_{\rm orb}$	Total	short-/long- $P_{\rm orb}$
HQS old-rec.	17	17	34	1
HQS old-nrec.	2	13	15	0.2
HQS new	14	28	42	0.5
HQS all	33	58	91	0.6
PG old	5	5	10	1
PG new	10	15	25	0.7
PG all	15	20	35	0.8
Ritter&Kolb	295	277	572	1.1

Note. HQS old-rec. and old-nrec. are the previously CVs with recovered and not recovered by our spectroscopic selection criterion, respectively.

these systems must look very different from the well-known short-period systems, i.e. have weak emission lines and/or substantially redder continua.

7.2.2 An accumulation of the new systems at the 3–4 h orbital period range

An unexpectedly large number of systems with orbital periods in the range 3–4 h were identified; nearly half (7 out of 16) of which are new SW Sex stars (see Section 4.6.1 for a full detailed discussion on CV population in this period range). Recently Rodríguez-Gil et al. (2007b) pointed out an increase in a large number of SW Sex stars in the the narrow 3–4.5 h period range as well as a large fraction of these systems in the 2–3 h period gap among the novalike variable/classical nova population. Whereas SW Sex stars initially appeared to be the “freaks” among the CVs, they now turn out to be an important subclass. Studying their relation to the global population of CVs may have important implications to our current understand of CV evolution as a whole.

The accumulation of systems just above the period gap represents an intriguing challenge to our current understanding of CV evolution. While most of the CV population models do not show any particular accumulation above the period gap (e.g. Kolb 1993; Howell et al. 2001), the theoretical study by de Kool (1992) found that the orbital period distribution of CVs contains a peak above the period gap ($\sim 3-4$ h), if the initial mass ratio distribution is assumed to be peaked towards equal masses in the zero-age main-sequence binaries. However, the stellar masses in the well-studied eclipsing SW Sex star DW UMa ($P_{\rm orb} = 3.28$ h) are $M_{\rm wd} = 0.77 \pm 0.07\,M_\odot$ and $M_{\rm sec} = 0.30 \pm 0.10\,M_\odot$ (Araujo-Betancor et al. 2003b), suggesting a very unequal mass ratio for the initial main-sequence progenitor binary. The lack of evidence of equal masses to produce a spike above the period gap in the population model seriously challenges our current understanding of CV evolution.

7.3 Comparison with Palomar-Green survey

The HQS represents currently the largest-area CV survey based on optical data[2]. We compare its population to the previously largest survey, the Palomar-Green (PG) survey. The PG survey was a high-galactic latitude UV excess survey. The photographic U and B observations were carried out using the Palomar 46 cm Schmidt telescope, covering 10714 deg^2, or about a quarter of the sky at galactic latitudes $|b| > 30^\circ$ and declinations $\delta > -10^\circ$ with a limiting magnitude $15.5 \lesssim B \lesssim 16.7$, and a colour selection criterion of $U - B < -0.46$ (Green et al. 1986). The survey discovered a sample of 35 CVs (Ringwald 1993, 1996, and references therein), of which ten are previously known CVs. Figure 7.2 illustrates the orbital period distributions of the new PG CVs (left panel) and that of all PG CVs (right panel where the gray shaded systems are the previously known CVs). Overall, the period dis-

[2]While SDSS has discovered already more CVs than the HQS, it (a) still covers a smaller area, (b) is not complete due to the limited number of fibres, and (c) saturates at $V \sim 15$, hence it is incomplete for nearby intrinsically bright CVs.

tribution of PG CVs is similar to that of all observed CV population in Figure 1.2. We now compare the orbital period distribution of new PG CVs to that of new HQS CVs. The most distinct feature found in these two surveys is the accumulation of systems at the 3–4 h period range which is occupied by a large fraction of SW Sex stars. This is most extremely the case in the PG survey where six SW Sex stars (SW Sex, Penning et al. 1984; DW UMa, Shafter et al. 1988; PX And, Thorstensen et al. 1991b; BH Lyn, Thorstensen et al. 1991a; WX Ari, Beuermann et al. 1992; and BP Lyn Ringwald 1993) are found among eight systems (75%) in this period range. In contrast with the HQS, the PG survey shows a preference towards the discovery of short-period systems just below the period gap, while the HQS provides more systems near period minimum. Finally, the lack of long-period systems at $P_{\rm orb} \gtrsim 6$ h is similar in both surveys.

Interestingly, the ratio of short-period to long-period systems among the previously known CVs in the PG survey is unity (Table 7.1), similar to that of the previously known HQS CVs that are recovered by spectroscopic selection. The ratio of short- to long-period systems among the new PG CVs is smaller than that of the known CVs in Ritter & Kolb (2003), again similar to the results we found from our survey. Recently, Pretorius et al. (2007) pointed out that the distribution of the predicted intrinsic population is inconsistent with the PG CV sample. In particular, the discrepancy found in the ratio of long-period to short-period systems is much higher than the predicted one. The authors pointed out as well the lack of period bouncers in the PG sample. This confirms the deep-rooted problems in the standard model of CV evolution.

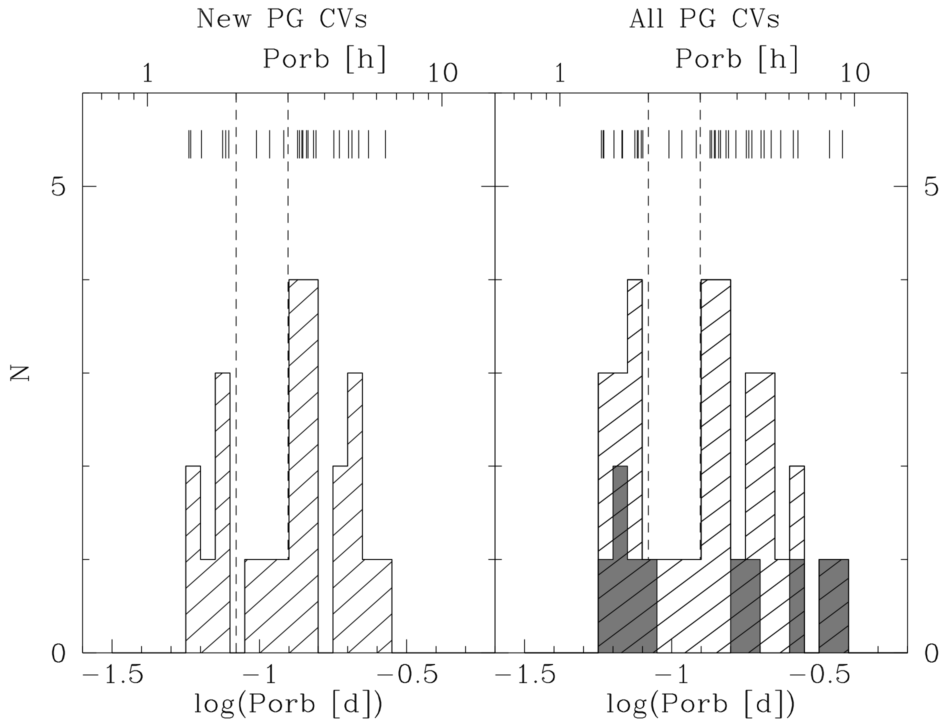

Figure 7.2: *Left panel:* Orbital period distribution of 25 new PG CVs. *Right panel:* Orbital period distribution of all PG CVs consisting of 25 new CVs (white shade) and 10 previously known CVs (gray shade) The tick-marks indicate the individual periods. The conventional 2–3 h period gap is represented by dashed lines. Data are provided by B. Gänsicke.

Table 7.2: The 53 new CVs/pre-CVs discovered in the HQS.

HQS ID	Other name	P_{orb} (min)	Type[a]	References[b]
CVs with orbital period measurements				
HS 2331+3905		81.1	DN:/WZ:	1
HS 1449+6415	KV Dra	84.9	DN/SU	2,3
HS 0752+6314	HT Cam	86.0	IP	2,4,5,6,7
HS 0756+1624	DW Cnc	86.1	IP, VY	8,9,10
HS 2219+1824		86.2	DN/SU	11
HS 1340+1524		92.7	DN/XX	this work
HS 1017+5319	KS UMa	97.9	DN/SU	2,12
HS 0417+7445		105.1/109.9	DN/SU	this work
HS 1016+3412		114.3	DN/XX	this work
HS 0913+0913	GZ Cnc	127.1	DN/XX, IP:	2,13,14
HS 1552+2730	RX J1554.2+2721	151.8	AM	2,15,16,17,18
HS 1023+3900	WX LMi	167.6	AM, PP:	19,20,21
HS 2237+8154		178.1	CV:,PC:	22
HS 2141+1231		181	NL:	23
HS 1607+0400	RX J161008.0+035222	192	AM	2,24,25
HS 0728+6738		192.6	NL/SW	26
HS 0805+3822	SDSS J080908.39+381406.2	193	NL/SW	27,28
HS 2133+0513		197	NL:,ZC:	23
HS 0129+2933	TT Tri	201.1	NL/SW	28
HS 0551+7241	LS Cam	~ 240	IP:, VY:	29
HS 0357+0614	KUV 03580+0614	205.5	NL/SW	30,31
HS 0506+7725		212.7	NL/VY	this work
HS 1813+6122		213.0	NL/SW	28

Continued on next page

HQS ID	Other name	P_{orb} (min)	Type[a]	References[b]
HS 0455+8315		214.2	NL/SW	28
HS 0220+0603		214.9	NL/SW	28
HS 0941+0411	RX J0944.5+0357	215.0	DN/XX	2,32
HS 0552+6753	LU Cam	216.6	DN/UG	2,25
HS 0758+4019	SDSS J080215.39+401047.2	221.6	NL	33
HS 0642+5049		225.9	NL/UX:, DN/ZC:	this work
HS 0229+8016		232.6	NL/UX:, DN/ZC:	this work
HS 0922+1333		244.0	AM, PP:	34, 35
HS 0139+0559		243.7	NL/UX:, DN/ZC:	this work
HS 0943+1404		250	IP	36
HS 0907+1902	GY Cnc	252.6	DN/UG	2,37,38
HS 2214+2845		258.0	DN/UG	this work
HS 1857+7127		272.3	DN/ZC:	this work
HS 2325+8205		280	DN:/ZC:	39
HS 0618+7336	1RXS J062518.2+733433	283.0	IP	40,41,42
HS 2205+0201		300	CV	23
HS 1804+6753	EX Dra	302.3	DN/UG	43,44,45
HS 1857+5144		383.5	PC	this work
HS 0218+3229		462.5	CV/DN:	46
HS 1055+0939		541	DN	46
HS 1316+6747	PG 1316+678	~ 3.4 d:	PC	47,48,49
CVs with no orbital period measurements				
HS 0002+0901			CV	
HS 0019+3947			NL:, DN/ZC:	
HS 0038+4308	HV And		NL:, DN/ZC:	50
HS 0058+4307	IW And		NL:, DN/ZC:	51

Continued on next page

HQS ID	Other name	P_{orb} (min)	Type[a]	References[b]
HS 0124+3752			DN	
HS 0128+3547	RX J0131.4+3602		DN:	2
HS 0819+2033			CV:	
HS 1434+2355	RX J1437.0+2342		DN	2,24
HS 1634+4658	SDSSJ 163605.00+465204.5		CV	52

[a]AM: polar, DN: dwarf nova, IP: intermediate polar, NL: novalike variable, PC: pre-CV, PP: pre-polar candidate, SU: SU UMa-type dwarf nova, SW: SW Sex star, UG: U Gem-type dwarf nova, UX: UX UMa-type novalike variable VY: VY Scl star, WZ: WZ Sge star, ZC: Z Cam-type dwarf nova, XX: unclassified subclass. Uncertain classifications are marked by a colon.

[b](1) Araujo-Betancor et al. (2005a); (2) Jiang et al. (2000); (3) Nogami et al. (2000); (4) Tovmassian et al. (1998); (5) Kemp et al. (2002); (6) Ishioka et al. (2002); (7) de Martino et al. (2005); (8) Uemura et al. (2002); (9) Rodríguez-Gil et al. (2004a); (10) Patterson et al. (2004); (11) Rodríguez-Gil et al. (2005a); (12) Patterson et al. (2003); (13) Kato et al. (2002a); (14) Tappert & Bianchini (2003); (15) Tovmassian et al. (2001); (16) Thorstensen & Fenton (2002); (17) Gänsicke et al. (2004b); (18) Schwope et al. (2006); (19) Reimers et al. (1999); (20) Schwarz et al. (2001); (21) Vogel et al. (2007); (22) Gänsicke et al. (2004a); (23) Gänsicke et al. in prep.; (24) Schwope et al. (2002); (25) Thorstensen priv. com.; (26) Rodríguez-Gil et al. (2004b); (27) Szkody et al. (2003) (28) Rodríguez-Gil et al. (2007b); (29) Dobrzycka et al. (1998); (30) Szkody et al. (2001); (31) Thorstensen & Taylor (2001); (32) Mennickent et al. (2002); (33) Rodriguez-gil priv. com.; (34) Reimers & Hagen (2000); (35) Tovmassian & Zharikov (2007); (36) Rodríguez-Gil et al. (2005b); (37) Gänsicke et al. (2000); (38) Kato et al. (2002b); (39) Pyrzas et al. in prep.; (40) Wei et al. (1999); (41) Araujo-Betancor et al. (2003a); (42) Staude et al. (2003); (43) Fiedler et al. (1997); (44) Billington et al. (1996); (45) Shafter & Holland (2003); (46) Rodriguez-gil et al. in prep.; (47) Tappert et al. (2000); (48) Misselt & Shafter (1995); (49) Gänsicke priv. com.; (50) Schwope & Reinsch (1992); (51) Kato et al. (2003); (52) Szkody et al. (2003).

Chapter 8

Conclusion

The work presented in this thesis is an attempt to establish a large homogeneously selected sample of CVs from the HQS that overcomes observational biases found in the previously known CV population. The ultimate goal of the project is to compile a statistically complete sample of CVs which could then be compared with the predictions of the current models of CV evolution as well as the previously known CV population. The large amount of observing time and man-power required to achieve this goal are far beyond the scope of this thesis. Based on the data at hand, however, this work underlines the deep-rooted problems in our understanding of CV evolution. The HQS CV sample provides a first glance at a CV sample that is closer to the intrinsic CV population than any previous study, and represents an important tool to improve our understanding in CV evolution. In this final chapter, I summarise the major results from the HQS presented in this thesis, and outline future work.

We are undertaking a large scale search for new CVs in the HQS at high galactic latitudes, $\delta > 0^\circ$ and $|b| > 20^\circ$, covering $\approx 13\,600\,\mathrm{deg}^2$, with a dynamic range of $13 \lesssim B \lesssim 18.5$. Our candidate selection was done systematically via the spectroscopic appearance of most CVs, i.e. the presence of Balmer emission lines, resulting in the discovery of 50 new CVs and 3 new pre-CVs. So far 44 CVs/pre-

CVs have had their orbital period determined. Overall the period distribution of the HQS CVs presents similar features found in that of the previously known CV population, i.e. a prominent period gap, a sharp cut-off at $P_{\rm orb} \simeq 80$ min, and a dwindling amount of long-period systems. The main surprises are: (a) the small number of new short-period ($P_{\rm orb} \lesssim 3$ h) systems. In fact, the ratio of short- to long-period CVs in our sample is only half that of the previously known CVs, even though our selection method is specifically sensitive to short-period low mass-transfer systems. This aggravates the problem of the missing short-period CV population. We conclude that if numerous short-period systems do exist they must look different from the well known low mass-transfer systems such as e.g. WZ Sge, SU UMa, T Leo, and ST LMi. (b) the accumulation of long-period systems in the narrow period range of 3–4 h, just above the period gap, and a large fraction of SW Sex stars (7 out of 16) among these systems. None of these objects is a strong X-ray source or displays large-amplitude outbursts.

This thesis provides follow-up time-resolved optical spectroscopy and photometry of ten new systems among the 53 new CVs/pre-CVs. Their orbital periods were determined from radial velocity and photometric variability studies. In particular, four relatively bright ($V \sim 14.0 - 15.5$) long-period CVs, HS 0139+0559, HS 0229+8016, HS 0506+7725, and HS 0642+5049 increase the population in the 3–4 h period range with orbital periods of 243.69 ± 0.49 min, 232.550 ± 0.049 min, 212.7 ± 0.2 min, and 225.90 ± 0.23 min, respectively. Although they inhabit the same orbital period range, they greatly differ in their observed properties. HS 0506+7725 is classified as a VY Scl star. The other three systems are identified either as UX UMa-type novalike variables or as Z Cam-type dwarf novae.

The orbital periods of new five dwarf novae span the range $\sim 1.5 - 5$ h i.e. $P_{\rm orb} \simeq 105.1$ min or $P_{\rm orb} \simeq 109.9$ min (HS 0417+7445), $P_{\rm orb} = 114.3 \pm 2.7$ min (HS 1016+3412), $P_{\rm orb} = 92.66 \pm 0.17$ min (HS 1340+1524), $P_{\rm orb} = 272.317 \pm 0.001$-min (HS 1857+7127), and $P_{\rm orb} = 258.02 \pm 0.56$ min (HS 2214+2845). These five new dwarf novae display a variety of observed properties. We recorded one superoutburst of HS 0417+7445, identifying the system as a SU UMa-type dwarf nova. HS 1016+3412 and HS 1340+1524 have rare outbursts, and their subtype is yet undetermined. HS 1857+7127 is found to be partially eclipsing, frequently varies in brightness and is likely to be a Z Cam-type dwarf nova. In HS 2214+2845, the M-type secondary star is clearly seen; we classified this system as a U Gem-type dwarf nova with a most likely cycle length of 71 d.

The ratio of short-period ($\lesssim 3$ h) to long-period (> 3 h) dwarf novae of the HQS sample is 1.3, much smaller compared to the ratio of 2.7 found for all known dwarf novae. The HQS dwarf novae display typically infrequent or low-amplitude outburst activity, underlining the strength of spectroscopic selection in identifying new CVs independently of their variability. The spectroscopic properties of short-period CVs in the HQS, newly identified and previously known, suggest that most or possibly all of them are still evolving towards the minimum period. Their total number agrees with the predictions of population models to within an order of magnitude. However, the bulk of all CVs is predicted to have evolved past the minimum period, and those systems remain unidentified. This suggests that those post-bounce systems have markedly weaker Hβ emission lines compared to the average known short-period CVs, and undergo no or extremely rare outbursts.

The orbital period of a new detached white dwarf/M dwarf binary, HS1857+5144, was determined to be $P_{\rm orb} = 383.5203 \pm 0.0001$ min. The system contains a hot white dwarf with temperature of $\sim 70\,000 - 100\,000$ K that illuminates the inner hemisphere of the M dwarf companion, resulting in a large reflection effect observed in the light curves. We estimated the masses of the stellar components to be $M_{\rm wd} \simeq 0.6 - 1.0\,M_{\odot}$ and $M_{\rm sec} \simeq 0.15 - 0.30\,M_{\odot}$ as well as an inclination of $i \simeq 45^{\circ} - 55^{\circ}$. The cooling age of the white dwarf suggests that the system has just emerged from a common envelope phase $\sim 10^5$ yr ago and will start mass transfer within or below the 2–3 h period gap.

Future work

In order to complete the new HQS CV sample, the orbital periods of nine CVs (Table 7.2, for CVs with no orbital period measurements) need to be obtained. In Chapter 5, the space density of short-period systems was estimated, but detailed follow-up information (e.g. distances, masses, temperatures, and subclasses) are required to derive the true space density of the HQS CVs to be compared with the predicted values.

Interestingly, the Sloan Digital Sky Survey (SDSS) is discovering a number of CVs with a steep Balmer decrement, in which the white dwarf dominates the optical emission, a clear sign of low mass-transfer rates (Szkody et al. 2005 and references therein). However, most of these systems are very faint, $g \simeq 19-20$, implying that they are distant ($d > 100\,\mathrm{pc}$) and not intrinsically numerous anywhere near the numbers predicted by theory. Recently, Szkody et al. (2007) have published the total number of CVs in the SDSS data base to be 213, of which 177 are new discoveries. Based on the published data $\sim 40\%$ of the SDSS CVs have accurate orbital period measurements. It appears that the SDSS is successful in finding systems below the period gap, with a large fraction of 70%, which differs dramatically from the statistics of the HQS CVs or that of the previously known CVs. Although SDSS seems to provide a large number of all systems below the period gap, the number of the short-period systems near the period minimum still does not match that of model estimates. However, before drawing any solid conclusion, the orbital periods of the whole sample must be derived.

Appendix A

Finding charts

$10' \times 10'$ finding charts for HS 0139+0559, HS 0229+8016, HS 0417+7445, HS 0506+7725, HS 0642+5049, HS 1016+3412, HS 1340+1524, HS 1857+5144, HS 1857+7127, HS 2214+2845, and comparison stars used for the differential CCD photometry in Chapter 2.

Table A.1: Comparison stars used for the differential CCD photometry in Chapter 2

ID	USNO-A2.0	*R*	*B*
C1	1650-00512682	12.6	13.5
C2	1575-02009718	13.3	13.3
C3	1575-02008711	13.6	14.9
C4	1650-00942250	13.1	14.2
C5	1350-06806656	12.4	13.3
C6	1200-06495553	14.3	15.0
C7	1050-06991669	13.4	14.5
C8	1050-06992410	14.4	16.4
C9	1050-06992029	15.3	17.3
C10	1350-10080469	13.2	14.7
C11	1350-10079362	16.4	17.8
C12	1575-04072972	12.2	13.5
C13	1575-04073098	13.8	14.8
C14	1575-04073991	13.8	14.9
C15	1125-19198939	13.7	14.8
C16	1125-19199670	15.0	15.6

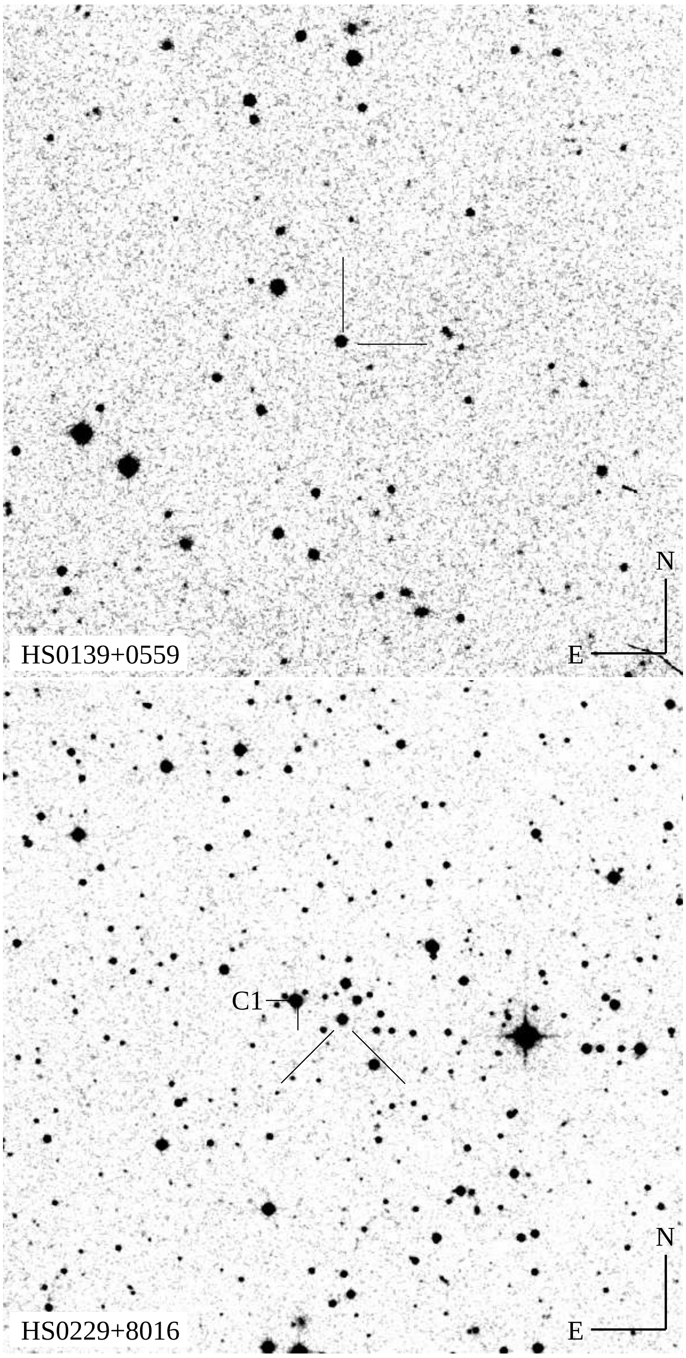
N
E
HS0139+0559
C1
N
E
HS0229+8016

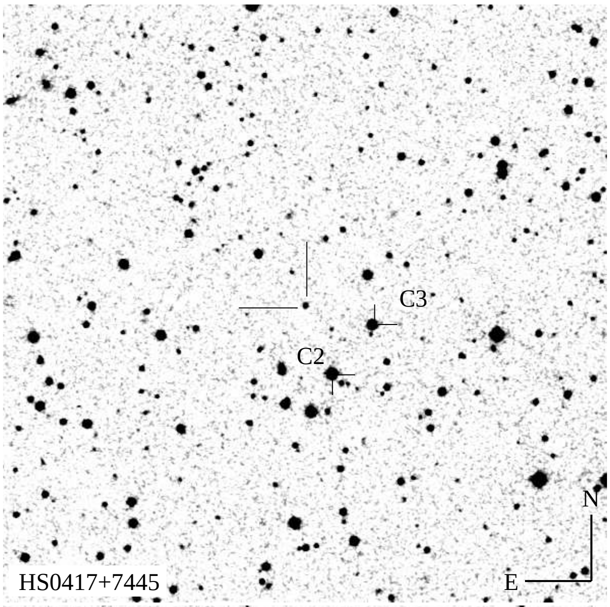
C3
C2
HS0417+7445
N
E

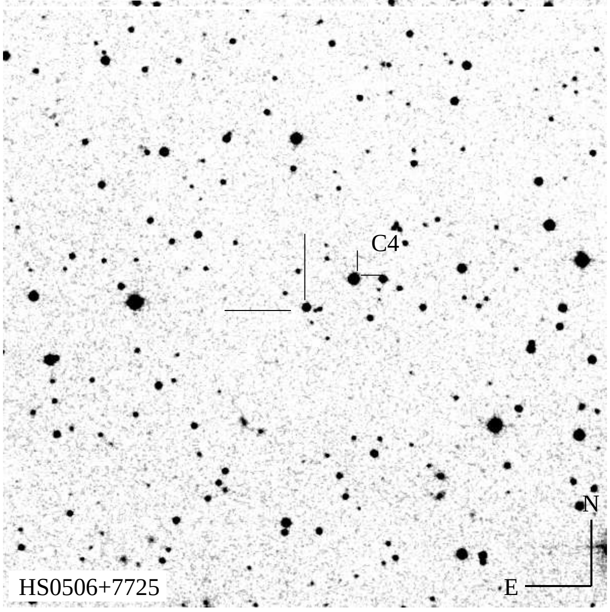
C4
HS0506+7725
N
E

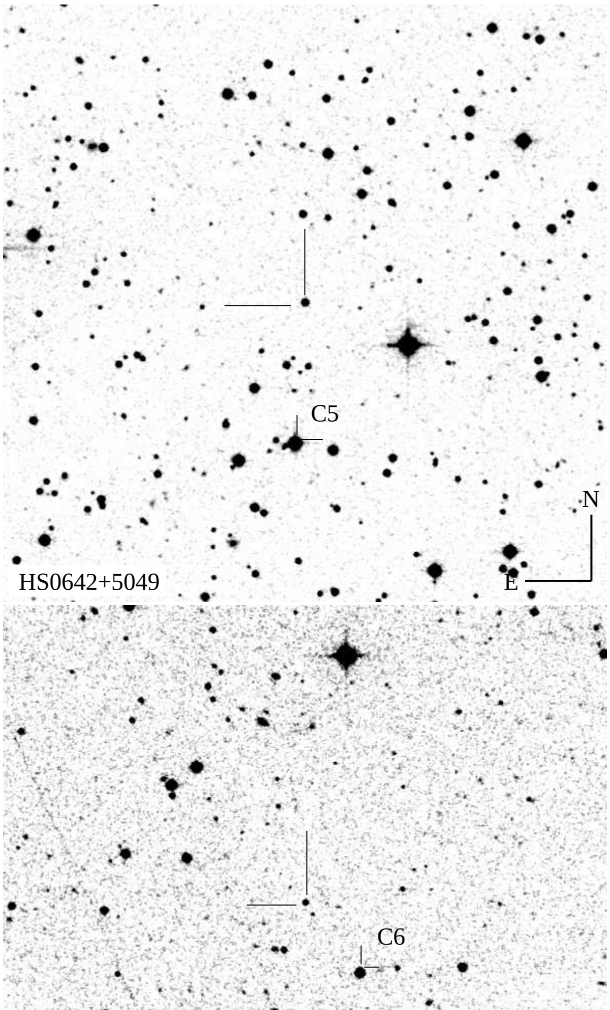
C5
N
HS0642+5049
E
C6
N
HS1016+3412
E

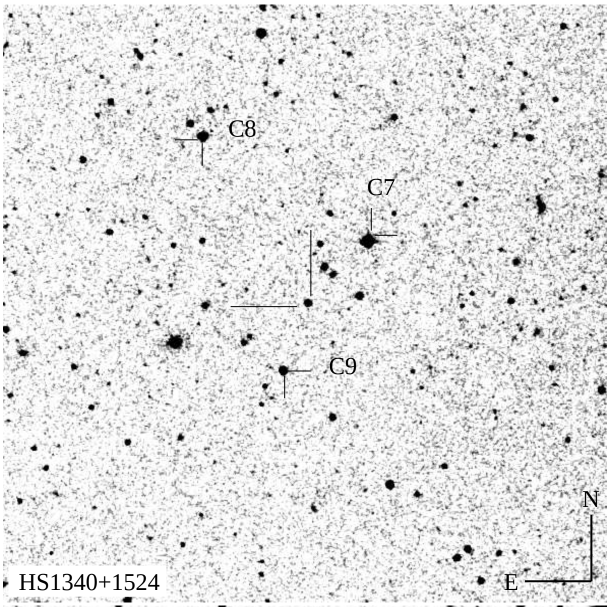
C8
C7
C9
N
E
HS1340+1524

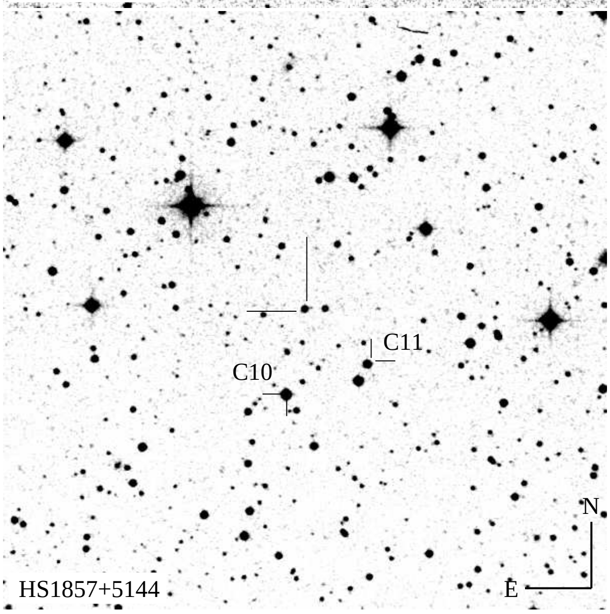
C11
C10
N
E
HS1857+5144

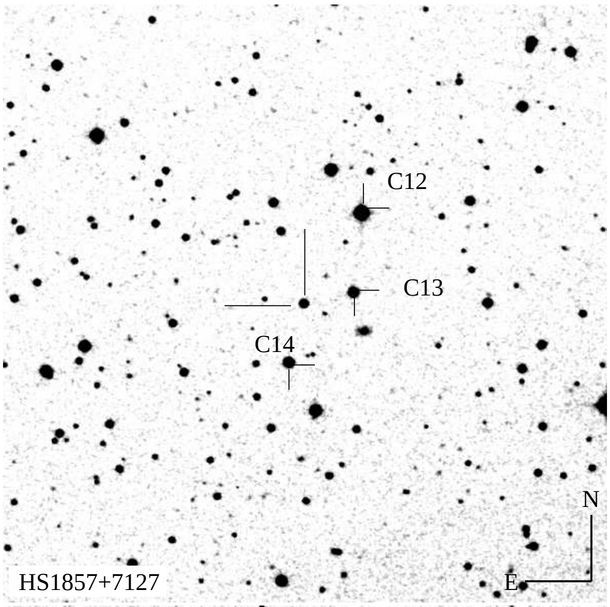
C12
C13
C14
N
E
HS1857+7127

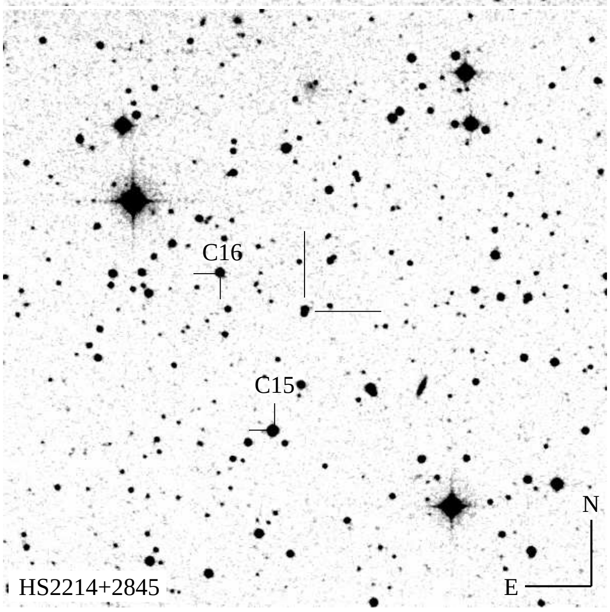
C16
C15
N
E
HS2214+2845

Bibliography

Abbott, T. M. C., Fleming, T. A., & Pasquini, L. 1997, A&A, 318, 134

Andronov, N., Pinsonneault, M., & Sills, A. 2003, ApJ, 582, 358

Araujo-Betancor, S., Gänsicke, B. T., Hagen, H.-J., et al. 2005a, A&A, 430, 629

Araujo-Betancor, S., Gänsicke, B. T., Hagen, H.-J., Rodríguez-Gil, P., & Engels, D. 2003a, A&A, 406, 213

Araujo-Betancor, S., Gänsicke, B. T., Long, K. S., et al. 2005b, ApJ, 622, 589

Araujo-Betancor, S., Knigge, C., Long, K. S., et al. 2003b, ApJ, 583, 437

Baptista, R. & Catalán, M. S. 2001, MNRAS, 324, 599

Baptista, R., Catalán, M. S., & Costa, L. 2000, MNRAS, 316, 529

Barker, J. & Kolb, U. 2003, MNRAS, 340, 623

Barman, T. S., Hauschildt, P. H., & Allard, F. 2004, ApJ, 614, 338

Bergeron, P., Wesemael, F., & Beauchamp, A. 1995, PASP, 107, 1047

Berriman, G., Beattie, D. H., Gatley, I., et al. 1983, MNRAS, 204, 1105

Bertin, E. & Arnouts, S. 1996, A&AS, 117, 393

Beuermann, K., Thomas, H.-C., Reinsch, K., et al. 1999, A&A, 347, 47

Beuermann, K., Thorstensen, J. R., Schwope, A. D., Ringwald, F. A., & Sahin, H. 1992, A&A, 256, 442

Beuermann, K. & Weichhold, M. 1999, in Annapolis Workshop on Magnetic Cataclysmic Variables, ed. C. Hellier & K. Mukai (ASP Conf. Ser. 157), 283–290

Beuermann, K., Wheatley, P., Ramsay, G., Euchner, F., & Gänsicke, B. T. 2000, A&A, 354, L49

Billington, I., Marsh, T. R., & Dhillon, V. S. 1996, MNRAS, 278, 673

Bond, H. E. & Grauer, A. D. 1987, in IAU Colloq. 95: Second Conference on Faint Blue Stars, ed. A. G. D. Philip, D. S. Hayes, & J. W. Liebert, 221–228

Bond, H. E. & Livio, M. 1990, ApJ, 355, 568

Cannizzo, J. K. 1993, in Accretion disks in compact stellar objects, ed. J. Wheeler, Advanced Series in Astrophysics and Cosmology No. 9 (Singapore: World Scientific), 6–40

Cannizzo, J. K., Wheeler, J. C., & Polidan, R. S. 1986, ApJ, 301, 634

Casares, J., Martinez-Pais, I. G., Marsh, T. R., Charles, P. A., & Lazaro, C. 1996, MNRAS, 278, 219

Cassisi, S., Iben, I., J., & Tornambe, A. 1998, ApJ, 496, 376

Chen, A., O'Donoghue, D., Stobie, R. S., et al. 1995, MNRAS, 275, 100

Chen, A., O'Donoghue, D., Stobie, R. S., Kilkenny, D., & Warner, B. 2001, MNRAS, 325, 89

Claret, A. 2000, A&A, 363, 1081

Clemens, J. C., Reid, I. N., Gizis, J. E., & O'Brien, M. S. 1998, ApJ, 496, 352

Cropper, M. 1990, Space Science Reviews, 54, 195

de Kool, M. 1992, A&A, 261, 188

de Martino, D., Matt, G., Mukai, K., et al. 2005, A&A, 437, 935

Diaz, M. P. & Bruch, A. 1997, A&A, 322, 807

Dickinson, R. J., Prinja, R. K., Rosen, S. R., et al. 1997, MNRAS, 286, 447

Dobrzycka, D., Dobrzycki, A., Engels, D., & Hagen, H.-J. 1998, AJ, 115, 1634

Downes, R. A. 1986, ApJ, 307, 170

Downes, R. A., Webbink, R. F., Shara, M. M., et al. 2001, PASP, 113, 764

Duerbeck, H. W. & Seitter, W. C. 1987, Ap&SS, 131, 467

Eggleton, P. P. 1983, ApJ, 268, 368

Evans, P. A. & Hellier, C. 2005, MNRAS, 359, 1531

Exter, K. M., Pollacco, D. L., & Bell, S. A. 2003, MNRAS, 341, 1349

Exter, K. M., Pollacco, D. L., Maxted, P. F. L., Napiwotzki, R., & Bell, S. A. 2005, MNRAS, 359, 315

Feline, W. J., Dhillon, V. S., Marsh, T. R., Watson, C. A., & Littlefair, S. P. 2005, MNRAS, 364, 1158

Ferguson, D. H. & James, T. A. 1994, ApJS, 94, 723

Ferguson, D. H., Liebert, J., Cutri, R., et al. 1987, ApJ, 316, 399

Ferguson, D. H., Liebert, J., Haas, S., Napiwotzki, R., & James, T. A. 1999, ApJ, 518, 866

Ferguson, D. H., McGraw, J. T., Spinrad, H., Liebert, J., & Green, R. F. 1981, ApJ, 251, 205

Fiedler, H., Barwig, H., & Mantel, K. H. 1997, A&A, 327, 173

Gänsicke, B. T. 2004, in Compact Binaries and Beyond, ed. G. Tovmassian & E. Sion, Conf. Ser. No. 20 (RMAA), 152–154

Gänsicke, B. T., Marsh, T. R., Edge, A., et al. 2005a, MNRAS, 361, 141

Gänsicke, B. T., Szkody, P., Howell, S. B., & Sion, E. M. 2005b, ApJ, 629, 451

Gänsicke, B. T. 2000, Reviews of Modern Astronomy, 13, 151

Gänsicke, B. T. 2005, in The Astrophysics of Cataclysmic Variables and Related Objects, ed. J.-M. Hameury & J.-P. Lasota (ASP Conf. Ser. 330), 3–16

Gänsicke, B. T., Araujo-Betancor, S., Hagen, H.-J., et al. 2004a, A&A, 418, 265

Gänsicke, B. T., Beuermann, K., & Reinsch, K., eds. 2002a, The Physics of Cataclysmic Variables and Related Objects (ASP Conf. Ser. 261)

Gänsicke, B. T., Fried, R. E., Hagen, H.-J., et al. 2000, A&A, 356, L79

Gänsicke, B. T., Hagen, H. J., & Engels, D. 2002b, in The Physics of Cataclysmic Variables and Related Objects, ed. B. T. Gänsicke, K. Beuermann, & K. Reinsch (ASP Conf. Ser. 261), 190–199

Gänsicke, B. T., Jordan, S., Beuermann, K., et al. 2004b, ApJ Lett., 613, L141

Gänsicke, B. T., Schmidt, G. D., Jordan, S., & Szkody, P. 2001, ApJ, 555, 380

Gilliland, R. L., Kemper, E., & Suntzeff, N. 1986, ApJ, 301, 252

Good, S. A., Barstow, M. A., Holberg, J. B., et al. 2004, MNRAS, 355, 1031

Grauer, A. D. & Bond, H. E. 1983, ApJ, 271, 259

Green, R. F., Ferguson, D. H., Liebert, J., & Schmidt, M. 1982, PASP, 94, 560

Green, R. F., Liebert, J., & Wesemael, F. 1984, ApJ, 280, 177

Green, R. F., Schmidt, M., & Liebert, J. 1986, ApJS, 61, 305

Greenstein, J. L. 1957, ApJ, 126, 23

Haefner, R. 1989, A&A, 213, L15

Haefner, R., Fiedler, A., Butler, K., & Barwig, H. 2004, A&A, 428, 181

Hagen, H.-J., Groote, D., Engels, D., & Reimers, D. 1995, A&AS, 111, 195

Hameury, J. M. & Lasota, J. P. 2002, A&A, 394, 231

Hameury, J.-M. & Lasota, J.-P., eds. 2005, The Astrophysics of Cataclysmic Variables and Related Objects (ASP Conf. Ser. 330)

Hamilton, R. T. & Sion, E. M. 2004, PASP, 116, 926

Heber, U., Drechsel, H., Østensen, R., et al. 2004, A&A, 420, 251

Heber, U., Jordan, S., & Weidemann, V. 1991, in NATO ASIC Proc. 336: White Dwarfs, 109

Hellier, C. 2001, Cataclysmic Variable Stars (Springer)

Hessman, F. V. & Hopp, U. 1990, A&A, 228, 387

Hessman, F. V., Robinson, E. L., Nather, R. E., & Zhang, E.-H. 1984, ApJ, 286, 747

Hilditch, R. W., Harries, T. J., & Hill, G. 1996, MNRAS, 279, 1380

Hillwig, T. C., Honeycutt, R. K., & Robertson, J. W. 2000, AJ, 120, 1113

Hirose, M. & Osaki, Y. 1990, PASJ, 42, 135

Hoard, D. W., Thorstensen, J. R., & Szkody, P. 2000, ApJ, 537, 936

Horne, K. 1986, PASP, 98, 609

Horne, K. & Marsh, T. R. 1986, MNRAS, 218, 761

Howell, S. B., Nelson, L. A., & Rappaport, S. 2001, ApJ, 550, 897

Howell, S. B., Rappaport, S., & Politano, M. 1997, MNRAS, 287, 929

Iben, I. J. 1991, ApJS, 76, 55

Iben, I., J. & Livio, M. 1993, pasp, 105, 1373

Iben, I., J. & Tutukov, A. V. 1993, ApJ, 418, 343

Ishioka, R., Kato, T., Uemura, M., et al. 2002, PASJ, 54, 581

Ivanova, N. & Taam, R. E. 2004, ApJ, 601, 1058

Jiang, X. J., Engels, D., Wei, J. Y., Tesch, F., & Hu, J. Y. 2000, A&A, 362, 263

Joergens, V., Spruit, H. C., & Rutten, R. G. M. 2000, A&A, 356, L33

Kato, T., Dubovsky, P. A., Stubbings, R., et al. 2002a, A&A, 396, 929

Kato, T., Ishioka, R., & Uemura, M. 2002b, PASJ, 54, 1023

Kato, T., Ishioka, R., & Uemura, M. 2003, IBVS, 5376, 1

Kato, T. & Nogami, D. 1997, PASJ, 49, 341

Kawka, A., Vennes, S., Koch, R., & Williams, A. 2002, AJ, 124, 2853

Kemp, J., Patterson, J., Thorstensen, J. R., et al. 2002, PASP, 114, 623

King, A. R. 1988, QJRAS, 29, 1

King, A. R. & Kolb, U. 1995, ApJ, 439, 330

King, A. R. & Schenker, K. 2002, in The Physics of Cataclysmic Variables and Related Objects, ed. B. T. Gänsicke, K. Beuermann, & K. Reinsch (ASP Conf. Ser. 261), 233–241

King, A. R., Schenker, K., & Hameury, J. M. 2002, MNRAS, 335, 513

Knigge, C. 2006, MNRAS, 373, 484

Knigge, C., Long, K. S., Blair, W. P., & Wade, R. A. 1997, ApJ, 476, 291

Koester, D., Napiwotzki, R., Voss, B., Homeier, D., & Reimers, D. 2005, A&A, 439, 317

Kohoutek, L. & Schnur, G. F. O. 1982, MNRAS, 201, 21

Kolb, U. 1993, A&A, 271, 149

Kolb, U. & Baraffe, I. 1999, MNRAS, 309, 1034

Kolb, U., King, A. R., & Baraffe, I. 2001, MNRAS, 321, 544

Kolb, U., King, A. R., & Ritter, H. 1998, MNRAS, 298, L29

Kolb, U. & Ritter, H. 1992, A&A, 254, 213

Kolb, U. & Stehle, R. 1996, MNRAS, 282, 1454

Kraft, R. P., Mathews, J., & Greenstein, J. L. 1962, ApJ, 136, 312

Liebert, J., Bergeron, P., & Holberg, J. B. 2003, AJ, 125, 348

Liebert, J., Tweedy, R. W., Napiwotzki, R., & Fulbright, M. S. 1995, ApJ, 441, 424

Livio, M. & Pringle, J. E. 1994, ApJ, 427, 956

Lubow, S. H. 1991, ApJ, 381, 268

Lucy, L. B. 1967, Z. Astrophys., 65, 89

Martin, J. S., Jones, D. H. P., & Smith, R. C. 1987, MNRAS, 224, 1031

Martínez-Pais, I. G., Rodríguez-Gil, P., & Casares, J. 1999, MNRAS, 305, 661

Matthews, O. M., Wheatley, P. J., Wynn, G. A., & Truss, M. R. 2006, MNRAS, 372, 1593

McCormick, P. & Frank, J. 1998, ApJ, 500, 923

Mennickent, R. E., Tovmassian, G., Zharikov, S. V., et al. 2002, A&A, 383, 933

Miller, J. S., Krzeminski, W., & Priedhorsky, W. 1976, IAU Circ., 2974

Misselt, K. A. & Shafter, A. W. 1995, AJ, 109, 1757

Monet, D. G., Levine, S. E., Canzian, B., et al. 2003, AJ, 125, 984

Morales-Rueda, L. & Marsh, T. R. 2002, MNRAS, 332, 814

Mukai, K., Mason, K. O., Howell, S. B., et al. 1990, MNRAS, 245, 385

Nogami, D., Engels, D., Gänsicke, B. T., et al. 2000, A&A, 364, 701

Nogami, D., Masuda, S., & Kato, T. 1997, PASP, 109, 1114

Norton, A. J., Wynn, G. A., & Somerscales, R. V. 2004, ApJ, 614, 349

Orosz, J. A., Wade, R. A., Harlow, J. J. B., et al. 1999, AJ, 117, 1598

Osaki, Y. 1996, PASP, 108, 39

Paczyński, B. 1971, ARA&A, 9, 183

Paczynski, B. 1976, in IAU Symp. 73: Structure and Evolution of Close Binary Systems, ed. P. Eggleton, S. Mitton, & J. Whelan (Dordrecht: D. Reidel), 75–80

Paczyński, B. & Sienkiewicz, R. 1983, ApJ, 268, 825

Patterson, J. 1980, ApJ, 241, 235

Patterson, J. 1984, ApJS, 54, 443

Patterson, J. 1994, PASP, 106, 209

Patterson, J. 1998, PASP, 110, 1132

Patterson, J., Kemp, J., Harvey, D. A., et al. 2005, PASP, 117, 1204

Patterson, J., Masi, G., Richmond, M. W., et al. 2002, PASP, 114, 721

Patterson, J., Thorstensen, J. R., Kemp, J., et al. 2003, PASP, 115, 1308

Patterson, J., Thorstensen, J. R., Vanmunster, T., et al. 2004, PASP, 116, 516

Penning, W. R., Ferguson, D. H., McGraw, J. T., Liebert, J., & Green, R. F. 1984, ApJ, 276, 233

Politano, M. 1996, ApJ, 465, 338

Pollacco, D. L. & Bell, S. A. 1993, MNRAS, 262, 377

Pollacco, D. L. & Bell, S. A. 1994, MNRAS, 267, 452

Pretorius, M. L., Knigge, C., & Kolb, U. 2007, MNRAS, 374, 1495

Pringle, J. E. & Wade, R. A. 1985, Astronomy Express, 1, 159

Prša, A. & Zwitter, T. 2005, ApJ, 628, 426

Rappaport, S., Joss, P. C., & Verbunt, F. 1983, ApJ, 275, 713

Rebassa-Mansergas, A., Gänsicke, B. T., Rodríguez-Gil, P., Schreiber, M. R., & Koester, D. 2007, MNRAS, *submitted*

Reimers, D. & Hagen, H. J. 2000, A&A, 358, L45

Reimers, D., Hagen, H. J., & Hopp, U. 1999, A&A, 343, 157

Renvoizé, V., Baraffe, I., Kolb, U., & Ritter, H. 2002, A&A, 389, 485

Ringwald, F. 1993, PASP, 105, 805

Ringwald, F. A. 1996, in Cataclysmic Variables and Related Objects, ed. A. Evans & J. H. Wood, IAU Coll. No. 158 (Dordrecht: Kluwer), 89–92

Ringwald, F. A., Thorstensen, J. R., & Hamwey, R. M. 1994, MNRAS, 271, 323

Ritter, H. & Burkert, A. 1986, A&A, 158, 161

Ritter, H. & Kolb, U. 1998, A&AS, 129, 83

Ritter, H. & Kolb, U. 2003, A&A, 404, 301

Rodríguez-Gil, P. 2005, in The Astrophysics of Cataclysmic Variables and Related Objects, ed. J.-M. Hameury & J.-P. Lasota (ASP Conf. Ser. 330), 335–336

Rodríguez-Gil, P., Casares, J., Martínez-Pais, I. G., Hakala, P., & Steeghs, D. 2001, ApJ Lett., 548, L49

Rodríguez-Gil, P., Gänsicke, B. T., Araujo-Betancor, S., & Casares, J. 2004a, MNRAS, 349, 367

Rodríguez-Gil, P., Gänsicke, B. T., Barwig, H., Hagen, H.-J., & Engels, D. 2004b, A&A, 424, 647

Rodríguez-Gil, P., Gänsicke, B. T., Hagen, H.-J., et al. 2007a, MNRAS, 377, 1747

Rodríguez-Gil, P., Gänsicke, B. T., Hagen, H.-J., et al. 2005a, A&A, 431, 269

Rodríguez-Gil, P., Gänsicke, B. T., Hagen, H.-J., et al. 2005b, A&A, 440, 701

Rodríguez-Gil, P., Schmidtobreick, L., & Gänsicke, B. T. 2007b, MNRAS, 374, 1359

Rogoziecki, P. & Schwarzenberg-Czerny, A. 2001, MNRAS, 323, 850

Roth, M. M. 1992, in CCDs in astronomy, ed. G. Jacoby (ASP Conf. Ser. 8), 380–386

Scargle, J. D. 1982, ApJ, 263, 835

Schenker, K. & King, A. R. 2002, in The Physics of Cataclysmic Variables and Related Objects, ed. B. T. Gänsicke, K. Beuermann, & K. Reinsch (ASP Conf. Ser. 261), 242–251

Schenker, K., Kolb, U., & Ritter, H. 1998, MNRAS, 297, 633

Schneider, D. P. & Young, P. 1980, ApJ, 238, 946

Schreiber, M. R. & Gänsicke, B. T. 2003, A&A, 406, 305

Schreiber, M. R., Gänsicke, B. T., & Mattei, J. A. 2002, A&A, 384, L6

Schwarz, R., Schwope, A. D., & Staude, A. 2001, A&A, 374, 189

Schwarzenberg-Czerny, A. 1989, MNRAS, 241, 153

Schwarzenberg-Czerny, A. 1996, ApJ Lett., 460, L107

Schwope, A. D., Brunner, H., Buckley, D., et al. 2002, A&A, 396, 895

Schwope, A. D. & Reinsch, K. 1992, IBVS, 3725, 1

Schwope, A. D., Schreiber, M. R., & Szkody, P. 2006, A&A, 452, 955

Shafter, A. W. 1992, ApJ, 394, 268

Shafter, A. W., Clark, L. L., Holland, J., & Williams, S. J. 2000, PASP, 112, 1467

Shafter, A. W., Hessman, F. V., & Zhang, E.-H. 1988, ApJ, 327, 248

Shafter, A. W. & Holland, J. N. 2003, PASP, 115, 1105

Shafter, A. W., Wheeler, J. C., & Cannizzo, J. K. 1986, ApJ, 305, 261

Shimanskii, V. V., Borisov, N. V., Sakhibullin, N. A., & Surkov, A. E. 2004, Astronomy Reports, 48, 563

Shimansky, V., Sakhibullin, N. A., Bikmaev, I., et al. 2006, A&A, 456, 1069

Sills, A., Pinsonneault, M. H., & Terndrup, D. M. 2000, ApJ, 534, 335

Sing, D. K., Holberg, J. B., Burleigh, M. R., et al. 2004, AJ, 127, 2936

Sion, E. M. 1999, PASP, 111, 532

Skrutskie, M. F., Cutri, R. M., Stiening, R., et al. 2006, AJ, 131, 1163

Smak, J. 1983, ApJ, 272, 234

Smak, J. 1993, Acta Astron., 43, 101

Smith, D. A. & Dhillon, V. S. 1998, MNRAS, 301, 767

Spruit, H. C. & Ritter, H. 1983, A&A, 124, 267

Spruit, H. C. & Taam, R. E. 2001, ApJ, 548, 900

Staude, A., Schwope, A. D., Krumpe, M., Hambaryan, V., & Schwarz, R. 2003, A&A, 406, 253

Stauffer, J., Spinrad, H., & Thorstensen, J. 1979, PASP, 91, 59

Stepanian, J. A., Chavushyan, V. H., Carrasco, L., Tovmassian, H. M., & Erastova, L. K. 1999, PASP, 111, 1099

Stobie, R. S., Kilkenny, D., O'Donoghue, D., et al. 1997, MNRAS, 287, 848

Szkody, P., Desai, V., & Hoard, D. W. 2000, AJ, 119, 365

Szkody, P., Fraser, O., Silvestri, N., et al. 2003, AJ, 126, 1499

Szkody, P., Gänsicke, B. T., Fried, R. E., Heber, U., & Erb, D. K. 2001, PASP, 113, 1215

Szkody, P., Henden, A., Fraser, O. J., et al. 2005, AJ, 129, 2386

Szkody, P., Henden, A., Mannikko, L., et al. 2007, ApJ, 134, 185

Szkody, P. & Mateo, M. 1986, AJ, 92, 483

Taam, R. E., Sandquist, E. L., & Dubus, G. 2003, ApJ, 592, 1124

Taam, R. E. & Spruit, H. C. 1989, ApJ, 345, 972

Taam, R. E. & Spruit, H. C. 2001, ApJ, 561, 329

Tappert, C. & Bianchini, A. 2003, A&A, 401, 1101

Tappert, C., Oestreicher, M. O., Schmidtobreick, L., & Bianchini, A. 2000, IBVS, 4884, 1

Taylor, C. J., Thorstensen, J. R., & Patterson, J. 1999, PASP, 111, 184

Thorstensen, J. R. 2000, PASP, 112, 1269

Thorstensen, J. R., Charles, P. A., Bowyer, S., & Margon, B. 1978, ApJ, 223, 260

Thorstensen, J. R., Davis, M. K., & Ringwald, F. A. 1991a, AJ, 102, 683

Thorstensen, J. R. & Fenton, W. H. 2002, PASP, 114, 74

Thorstensen, J. R., Patterson, J., Kemp, J., & Vennes, S. 2002, PASP, 114, 1108

Thorstensen, J. R., Ringwald, F. A., Wade, R. A., Schmidt, G. D., & Norsworthy, J. E. 1991b, AJ, 102, 272

Thorstensen, J. R. & Taylor, C. J. 2001, MNRAS, 326, 1235

Thorstensen, J. R., Vennes, S., & Bowyer, S. 1996, ApJ, 457, 390

Thorstensen, J. R., Vennes, S., & Shambrook, A. 1994, AJ, 108, 1924

Tovmassian, G. H., Greiner, J., Kroll, P., et al. 1998, aa, 335, 227

Tovmassian, G. H., Greiner, J., Zharikov, S. V., Echevarría, J., & Kniazev, A. 2001, A&A, 380, 504

Tovmassian, G. H. & Zharikov, S. V. 2007, A&A, 468, 643

Townsley, D. M. & Bildsten, L. 2003, ApJ Lett., 596, L227

Uemura, M., Kato, T., Ishioka, R., Novak, R., & Pietz, J. 2002, pasj, 54, 299

van Teeseling, A., Beuermann, K., & Verbunt, F. 1996, A&A, 315, 467

Vennes, S. & Thorstensen, J. R. 1996, AJ, 112, 284

Vennes, S., Thorstensen, J. R., & Polomski, E. F. 1999, ApJ, 523, 386

Verbunt, F. & Zwaan, C. 1981, A&A, 100, L7

Vogel, J., Schwope, A. D., & Gänsicke, B. T. 2007, A&A, 464, 647

Voges, W., Aschenbach, B., Boller, T., et al. 1999, A&A, 349, 389

Voges, W., Aschenbach, B., Boller, T., et al. 2000, IAU Circ., 7432

von Zeipel, H. 1924, MNRAS, 84, 665

Wade, R. A. 1979, AJ, 84, 562

Wade, R. A. & Horne, K. 1988, ApJ, 324, 411

Walsh, J. R. & Walton, N. A. 1996, A&A, 315, 253

Warner, B. 1987, MNRAS, 227, 23

Warner, B. 1995, Cataclysmic Variable Stars (Cambridge: Cambridge University Press)

Warner, B. 2002, in American Institute of Physics Conference Series, Vol. 637, Classical Nova Explosions, ed. M. Hernanz & J. José, 3–15

Webbink, R. F. 1979, in IAU Colloq. 53: White Dwarfs and Variable Degenerate Stars, 426–447

Wei, J. Y., Xu, D. W., Dong, X. Y., & Hu, J. Y. 1999, A&AS, 139, 575

Whitehurst, R. 1988, MNRAS, 232, 35

Willems, B. & Kolb, U. 2004, A&A, 419, 1057

Willems, B., Kolb, U., Sandquist, E. L., Taam, R. E., & Dubus, G. 2005, ApJ, 635, 1263

Wilson, R. E. 1979, ApJ, 234, 1054

Wilson, R. E. 1990, ApJ, 356, 613

Wilson, R. E. & Devinney, E. J. 1971, ApJ, 166, 605

Wood, J. H., Robinson, E. L., & Zhang, E.-H. 1995, MNRAS, 277, 87

Wu, X., Li, Z., Gao, W., & Leung, K. 2001, ApJ Lett., 549, L81

York, D. G., Adelman, J., Anderson, J. E., et al. 2000, AJ, 120, 1579

Zhang, E.-H. & Robinson, E. L. 1987, ApJ, 321, 813